

## In-flight calibration and performance of the Mars Exploration Rover Panoramic Camera (Pancam) instruments

J. F. Bell III, J. Joseph, J. N. Sohl-Dickstein, H. M. Arneson, and M. J. Johnson

Department of Astronomy, Cornell University, Ithaca, New York, USA

M. T. Lemmon

Department of Atmospheric Sciences, Texas A&M University, College Station, Texas, USA

D. Savransky

Department of Astronomy, Cornell University, Ithaca, New York, USA

Received 12 April 2005; revised 2 September 2005; accepted 16 September 2005; published 6 January 2006.

[1] The Mars Exploration Rover Panoramic Camera (MER/Pancam) instruments have acquired more than 60,000 high-resolution, multispectral, stereoscopic images of soil, rocks, and sky at the Gusev crater and Meridiani Planum landing sites since January 2004. These images, combined with other MER data sets, have enabled new discoveries about the composition, mineralogy, and geologic/geochemical evolution of both sites. One key to the success of Pancam in contributing to the overall success of MER has been the development of a calibration pipeline that can quickly remove instrumental artifacts and generate both absolute radiance and relative reflectance images with high accuracy and precision in order to influence tactical rover driving and in situ sampling decisions. This paper describes in detail the methods, assumptions, and models/algorithms in the calibration pipeline developed for Pancam images, based on new measurements and refinements performed primarily from flight data acquired on Mars. Major calibration steps include modeling and removal of detector bias signal, active and readout region dark current, electronic “shutter smear,” and pixel-to-pixel responsivity (flatfield) variations. Pancam images are calibrated to radiance ( $\text{W}/\text{m}^2/\text{nm}/\text{sr}$ ) using refined preflight-derived calibration coefficients, or radiance factor (I/F) using near-in-time measurements of the Pancam calibration target and a model of aeolian dust deposition on the target as a function of time. We are able to verify that the absolute radiance calibration of most Pancam images is accurate to within about 10% or less and that the filter-to-filter and pixel-to-pixel precision of the calibrated relative reflectance data (both based on measurements of the Pancam calibration target) are typically about 3% and 1% or less, respectively. Examples are also presented of scientific applications made possible by the high fidelity of the calibrated Pancam data. These include 11-color visible to near-IR spectral analysis, calculation of “true color” and chromaticity values, and generation of “super resolution” image data products. This work represents a follow-on and enhancement to the Pancam preflight calibration process described by Bell et al. (2003).

**Citation:** Bell, J. F., III, J. Joseph, J. N. Sohl-Dickstein, H. M. Arneson, M. J. Johnson, M. T. Lemmon, and D. Savransky (2006), In-flight calibration and performance of the Mars Exploration Rover Panoramic Camera (Pancam) instruments, *J. Geophys. Res.*, **111**, E02S03, doi:10.1029/2005JE002444.

### 1. Introduction

[2] The two Panoramic Camera (Pancam) instruments on the Mars Exploration Rover (MER) missions conducted by the rovers Spirit and Opportunity have acquired many tens of thousands of high-resolution, stereo, multispectral images of rocks, soil, and sky from both landing sites. The primary scientific goals of the Pancam contribution to the

Athena Science Team investigation on MER [Squyres et al., 2003] are to characterize the geology, geologic context, and atmospheric, photometric, and multispectral properties of each landing site and to help to provide constraints on the composition, mineralogy, and physical properties of the sites based on these and other MER data sets [Bell et al., 2003]. Pancam objectives also involve a number of important mission support activities, such as Sun-finding, atmospheric opacity monitoring, and characterization of potential rover drive targets. Successfully achieving these goals requires a high degree of

accuracy and precision in the calibration of Pancam images. A calibration was derived for Pancam images based on extensive preflight laboratory measurements made using the Pancam instruments both before and after they were integrated with the rest of the rover systems [Bell *et al.*, 2003]. During flight operations on Mars, we acquired additional “in flight” calibration data that have allowed us to augment, extend, and enhance the quality of calibrated Pancam images. This paper describes the methods and results related to these in-flight Pancam calibration activities, and along with the work by Bell *et al.* [2003] provides the instrumental and data set information needed by researchers interested in performing quantitative multispectral, radiometric, or photometric studies using the raw or calibrated Pancam imaging data that are archived and distributed through the NASA Planetary Data System (PDS).

[3] There is a left and a right Pancam on each rover, and the cameras return images up to  $1024 \times 1024$  pixels in size using a frame transfer Charge-Coupled Device (CCD) detector. Each camera uses a small 8-position filter wheel to obtain multispectral images. Thirteen narrow band “geology” filters can be used to acquire images in 11 distinct effective wavelengths ( $\lambda_{\text{eff}}$ ) ranging from 432 to 1009 nm with bandpasses from 16 to 38 nm. One empty filter position on the left Pancams can be used to provide broadband (L1 filter,  $\lambda_{\text{eff}} = 739 \pm 338$  nm) “bolometric” information from the scene, and each camera also has a narrowband plus neutral density filter that can be used to acquire blue or red wavelength images of the Sun (calibration of data from the Pancam solar filters is discussed in detail by M. T. Lemmon *et al.* (MER optical depth calibration and history, manuscript in preparation, 2005)) or to block the input light for dark current calibration imaging. Each rover also carries a small Pancam calibration target, consisting of a number of well-characterized color and gray scale regions that can be imaged by the Pancams to derive an accurate relative reflectance calibration for scenes of interest. Many more details on the design, assembly, testing, and preflight calibration of the Pancam instruments are presented by Bell *et al.* [2003].

[4] This paper provides a detailed description of the data sets and methods used for the in-flight instrumental and radiometric calibration of the Pancams, and provides some examples of data products and analyses which are enabled by the combined preflight and in-flight calibration campaigns and algorithms which we have implemented. Section 2 provides a detailed description of the in-flight Pancam calibration pipeline, which includes 8-bit to 12-bit resampling, modeling and removal of detector bias signal, active and readout region dark current, electronic “shutter smear,” and pixel-to-pixel responsivity (flatfield) variations, and characterization and correction of bad pixels not corrected by the previous steps. This section also provides details on the absolute radiance calibration (which is based primarily on preflight measurements described by Bell *et al.* [2003] but which has been enhanced and validated by in-flight measurements), on the relative reflectance calibration using near-in-time measurements of the Pancam calibration target (including a detailed model for dust deposition with time on the target surfaces), and on the derivation of estimated

bolometric albedo from the Pancam broadband L1 filter measurements. Where possible, estimates of the magnitude of the uncertainties introduced in the calibration for each of these steps are also addressed. Section 3 provides examples of some scientific applications that have been enabled by the high fidelity of the calibration that we have been able to achieve in the Pancam data set, including 11-wavelength multispectral analyses, derivation of “true color” and chromaticity information, and generation of “super resolution” images of a small number of geologically compelling targets. Section 4 provides a summary of the current state of Pancam image calibration and provides some details on possible future refinements. A number of extensive tables provide details about the calibration files and measurements performed in-flight on Mars. These, combined with several appendices containing additional details on data reduction, calibration, and PDS archived file formats, as well as the preflight geometric and radiometric calibration details provided by Bell *et al.* [2003], should provide the information needed for researchers to understand the methods and limitations inherent in calibration of the Pancam images, as well as the data and algorithms required to reproduce or enhance the calibrations themselves.

## 2. Calibration Procedures

[5] Raw Pancam images are downlinked from Mars in packetized telemetry and converted to Experiment Data Records (EDRs) by engineers at the Jet Propulsion Laboratory in Pasadena, California, and archived on the World Wide Web by the NASA PDS ([http://pdsimg.jpl.nasa.gov/cgi-bin/MER/search?INSTRUMENT\\_HOST\\_NAME=MARS\\_EXPLORATION\\_ROVER](http://pdsimg.jpl.nasa.gov/cgi-bin/MER/search?INSTRUMENT_HOST_NAME=MARS_EXPLORATION_ROVER)). The raw Data Number (DN) values stored in the PDS archived images are directly proportional to the number of photons incident on each CCD pixel during the commanded integration time and at each filter’s effective wavelength, modulated by a variety of correctable instrumental effects. The goal of calibration is to reconstruct the true observed scene radiance using a combination of preflight and in-flight test and calibration data to remove the instrument effects. This section describes how that process is performed, which results in the generation of Pancam “Science Reduced Data Records” (Science RDRs) that are archived and released to the community through the NASA PDS.

[6] Figure 1 provides a schematic illustration of the Pancam in-flight calibration pipeline. This process converts EDRs with raw DN values into calibrated RDRs in radiance units ( $\text{W}/\text{m}^2/\text{nm}/\text{sr}$ ) or relative reflectance units (using the Pancam calibration target as a standard). Each step of the pipeline is described in greater detail below. Where noted, some of the calibration steps are sometimes performed on board the rover by taking advantage of the significant data processing capabilities built into the MER flight software [Maki *et al.*, 2003; Bell *et al.*, 2003].

### 2.1. 8-Bit to 12-Bit Resampling

[7] Raw Pancam data are originally sampled by the CCD electronics with 12 bits per pixel (0–4095 DNs). However, it is usually desirable to scale the data down to a smaller number of bits per pixel so that Poisson noise is

# Pancam Calibration Pipeline

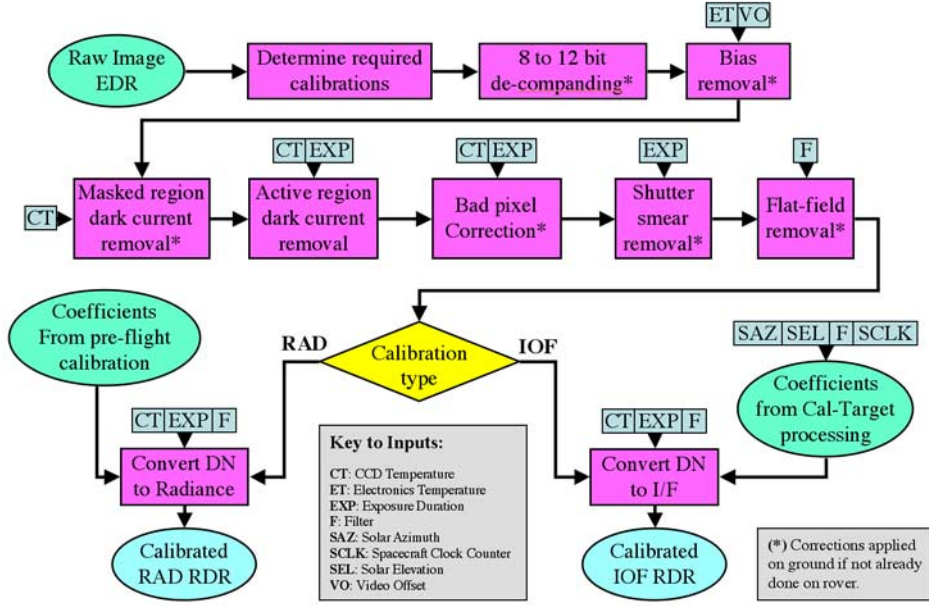


Figure 1. Schematic illustration of the Pancam in-flight calibration pipeline.

not encoded or downlinked in the telemetry. Approximately 73% of the raw Pancam images (corresponding to nearly 90% of the downlinked pixels) are scaled to 8 bits per pixel prior to downlink using one of several lookup tables (LUT) stored on board the rover. The shape of the LUTs used by Pancam is approximately a square-root function, with a 1-to-1 mapping for low DN values and a many-to-1 mapping for high DN values. Because Poisson noise in detectors like CCDs goes as the square root of the number of electrons detected, the square-root nature of the LUTs provides a way to decrease the number of bits downlinked without incurring a statistically significant loss of information (i.e., the noise is not quantized). In this first calibration step, if a 12 to 8 bit LUT was used to scale the data prior to downlink, we simply apply an inverse 8 to 12 bit LUT to restore the Pancam data to its original 12 bit (linearly proportional to radiance) format. Appendix A lists the inverse LUTs used for the Pancam instrument.

## 2.2. Bias Subtraction

[8] The horizontal serial register on the Pancam CCD contains an additional 32 pixels (16 “prefix” pixels to the left of the main CCD columns, and 16 “suffix” pixels to the right). These reference pixels are read out with each image row, and can be optionally saved to a file for downlink, if desired. When a reference pixel image containing these data is downlinked, it may be used to determine the row-dependent bias level for its associated image, so that the bias may be removed directly.

[9] For the initial in-flight calibration reported here, if the reference pixel file is not returned for a specific image, but reference pixel files were returned for the same camera for a different image in the same sequence, then the reference pixel data that is closest in time and in the same sequence as

the image being calibrated is used to remove the bias. This is our usual operating procedure for the Pancams on Mars, and is justified by examination of the sometimes-large temperature fluctuations that can occur in the CCDs and electronics during typical daily operations (Figure 2). If a usable reference pixel image is not available for the entire sequence, a new temperature-dependent model similar to the preflight calibration bias model described by *Bell et al.* [2003] but modified using available in-flight reference pixel data is used to remove the bias.

[10] The new bias model is based on in-flight reference pixel images (known as ERPs, for Experiment data record Reference Pixel images) downlinked from both rovers as of 10 September 2004. ERP data exhibiting anomalies (from missing telemetry packets, cosmic ray hits, or decompression error artifacts) were excluded from the analysis. As in the preflight calibration bias model, only columns 4 through 16 of the ERP files are used in the modeling, as these have been observed to exhibit the most stable and reliable bias estimates. The bias for a given row in an image is calculated as the mean value of the reference pixels in columns 4 through 16 in the corresponding row of the ERP. Because the electronics video offset level will affect the bias level, all data are first normalized to a video-offset value of 4095 [*Bell et al.*, 2003, equation (2)] before fitting a model. The new model has the same functional form as the preflight calibration bias model. That is,

$$\text{mean}(\text{Bias}_{4095}) = b_0 + b_1 \exp(b_2 T) \quad (1)$$

where  $\text{Bias}_{4095}$  is the ERP data normalized to a video offset value of 4095, and  $T$  is the temperature of the left Pancam electronics box as recorded in each ERP file. The data and model fits from each camera are shown in Figure 3 and the

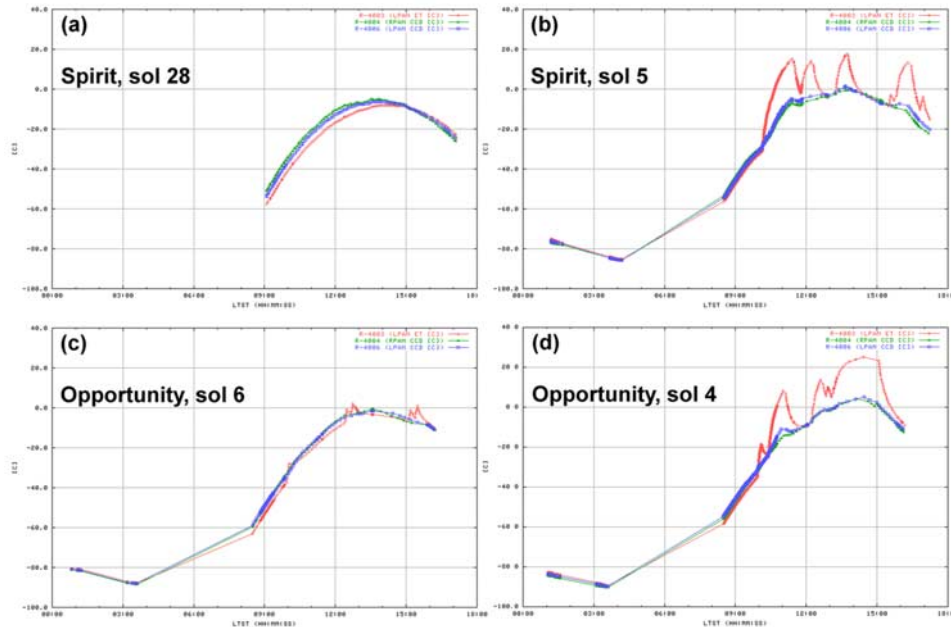


**Figure 2.** Plots of temperature telemetry data from the left Pancam electronics box (red lines) and left (blue) and right (green) Pancam CCDs on several representative sols from Spirit and Opportunity. The abscissa is local true solar time (LTST), beginning at midnight on each sol, and the ordinate is the temperature in °C. (a) A typical “light imaging” sol from Spirit, sol 28 (31 January 2004). (b) A typical “heavy imaging” sol from Spirit, sol 5 (7 January 2004). (c) A typical “light imaging” sol from Opportunity, sol 6 (29 January 2004). (d) A typical “heavy imaging” sol from Opportunity, sol 4 (27 January 2004). The large variations in electronics temperature during operations (red lines) translate directly into large variations in bias level. There are no temperature sensors for the right Pancam electronics boxes.

model values derived from the flight data are summarized in Table 1.

[11] The bias level varies slightly as a function of row on each CCD because of temperature variations during the readout process [Bell *et al.*, 2003]. During surface operations, we observed that the row-to-row offset of the bias value from the mean bias value over the image was not as smooth as during preflight calibration (Figure 4). The shape of this offset was similar to the curves we fit in our original model, but there is systematic and repeatable high-frequency structure in the data that cannot be modeled using a simple function. Therefore, instead of using an analytic function, we modeled the bias offset for each row by averaging the data from the flight ERP files to generate the empirical bias offset curves shown in Figure 4. While the bias offset is very consistent over a wide range of temperatures, there is a slight change in the shape of the offset versus row curve that trends with temperature (Figure 5). However, the magnitude of the variation is only about 0.1 DN over the operating range of the Pancam electronics, and so this effect has not been included in the current bias model.

[12] The bias level subtracted from each flight image, then, is the sum of the mean level defined by equation (1) and the row-by-row empirical offset values shown in Figure 4. From Figure 3, the  $3\sigma$  level of uncertainty associated with the bias model is  $<3$  DN, or less than about 0.1 to 0.2% of the signal level at half full well. There is some additional uncertainty in this process for the right eye

Pancams because all of the electronics temperature measurements come from the left Pancams only (limited space for running wires up and down the mast prevented us from activating the sensors on the right cameras’ electronics). However, both cameras are in a similar thermomechanical environment and both are usually used together during Pancam imaging observations, and so we assume that their electronics temperatures are highly correlated and approximately equal. The assumption appears to be justified because we usually only observe a few percent or less difference between calibrated left and right camera data for images of the same scenes through the two filters that overlap (at 430 nm and 750 nm).

### 2.3. Dark Current Modeling and Removal

[13] Thermal noise induces electron liberation in most semiconductor detectors, producing a temperature-dependent “dark current” in the devices even in the absence of illumination. This dark current accumulates in both the active (imaging) and masked (frame transfer) regions of the Pancam CCDs, though the rate of accumulation is different in the two regions [Bell *et al.*, 2003]. The temperature dependent models of the dark current in these two regions calculated during preflight characterization of the CCDs were modified for flight operations using dedicated dark current imaging measurements performed on Mars at a variety of temperatures (Tables 2 and 3).

[14] The preflight models for dark current accumulation in the 4 flight Pancams [Bell *et al.*, 2003] were developed



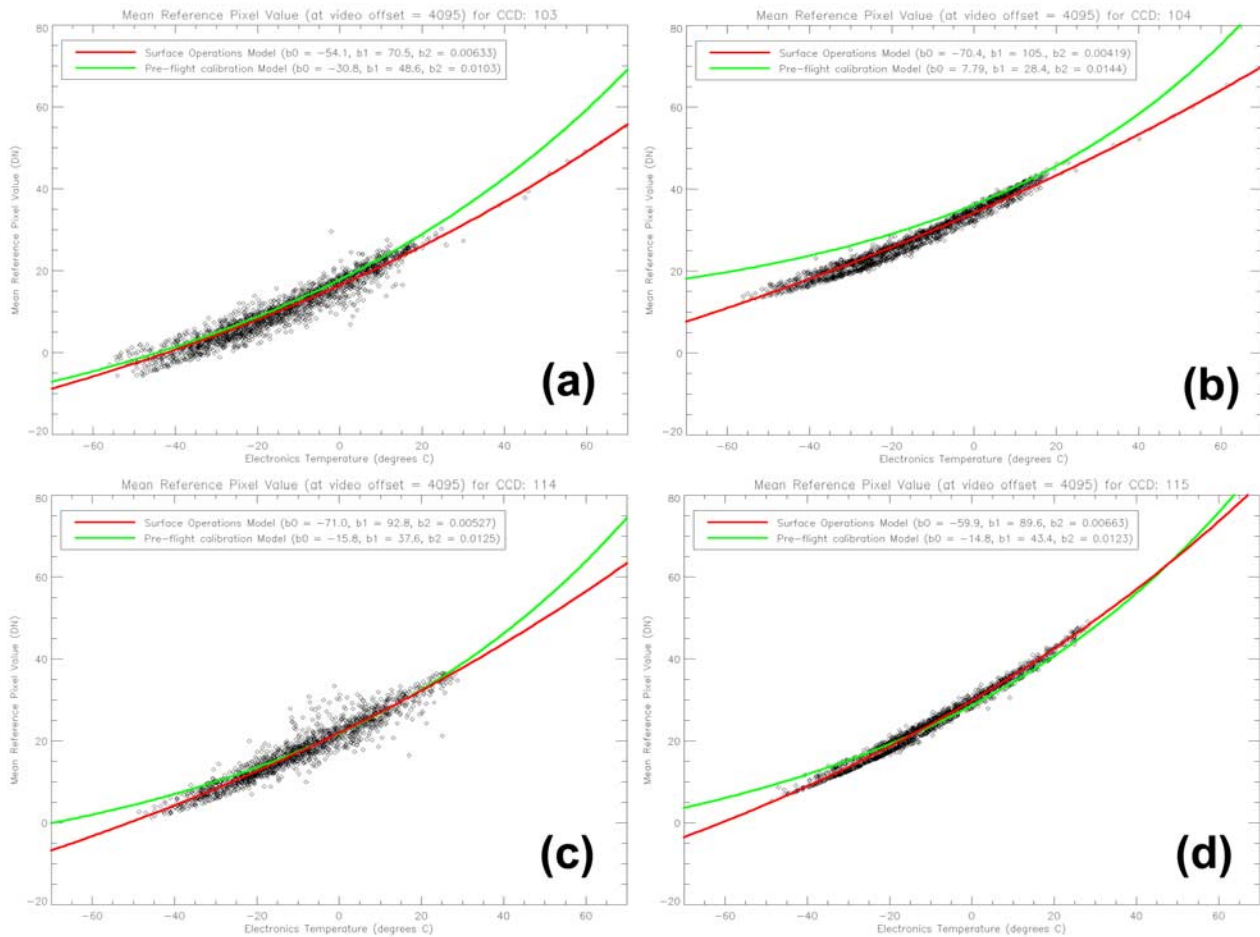


**Figure 3.** Plots of averaged video-offset corrected reference pixel (ERP) value versus left Pancam electronics box temperature for (a) the Spirit right Pancam S/N 103; (b) the Spirit left Pancam S/N 104; (c) the Opportunity right Pancam S/N 114; and (d) the Opportunity left Pancam S/N 115. The data are from in-flight measurements obtained on Mars between January and September 2004. The green curve is the preflight bias model developed by Bell *et al.* [2003]. The red curve is the new in-flight bias model described by equation (1) and Table 1.

by fitting exponential curves for each individual pixel, using data from dark frames taken at multiple temperatures during instrument and rover calibration tests. Because the preflight dark current models fit an exponential curve to each pixel individually based on a relatively small set of measurements, they were susceptible to the effects of noise and other artifacts in the data. For example, data values from pixels near the first read-out row of the masked region, which collect very little dark current, were so noisy that it was impossible to fit any meaningful exponential curve for them. As a result, the models for the masked-region dark current for a majority of pixels in the first ~50 rows adjacent to the read-out row had to be extrapolated.

[15] During preflight calibration, we noticed that the CCD temperature increased during the exposure. However, because we were not able to record temperature telemetry data automatically for each calibration image, our estimate of the actual CCD temperature had to be interpolated from more sparsely sampled temperature data recorded in our calibration log books. Thus we had to model the CCD warming effect by adjusting the estimated temperature on an image-

per-image basis. During cruise and on Mars, accurate CCD temperatures are automatically recorded in telemetry for each image acquired.

[16] Dedicated bias and dark current imaging sequences acquired in flight (acquired by imaging the surface through the neutral density solar filters) allow us to derive new models for both masked-region and active region dark current. As described below, these models are based on determining the average dark current with respect to temperature in the central region of each CCD (a central region is chosen to avoid edge effects) and then calculating the deviation of each individual pixel from the average as a ratio (a sort of “dark-current flat field” image). The new

**Table 1.** Pancam In-Flight Bias Model Parameters (Equation (1))

| Camera                    | S/N | # ERPs | $b_0$ | $b_1$ | $b_2$   |
|---------------------------|-----|--------|-------|-------|---------|
| MER-A (Spirit) right      | 103 | 2031   | -54.1 | 70.5  | 0.00633 |
| MER-A (Spirit) left       | 104 | 2058   | -70.4 | 105.  | 0.00419 |
| MER-B (Opportunity) right | 114 | 1670   | -71.0 | 92.8  | 0.00527 |
| MER-B (Opportunity) left  | 115 | 1784   | -59.9 | 89.6  | 0.00663 |

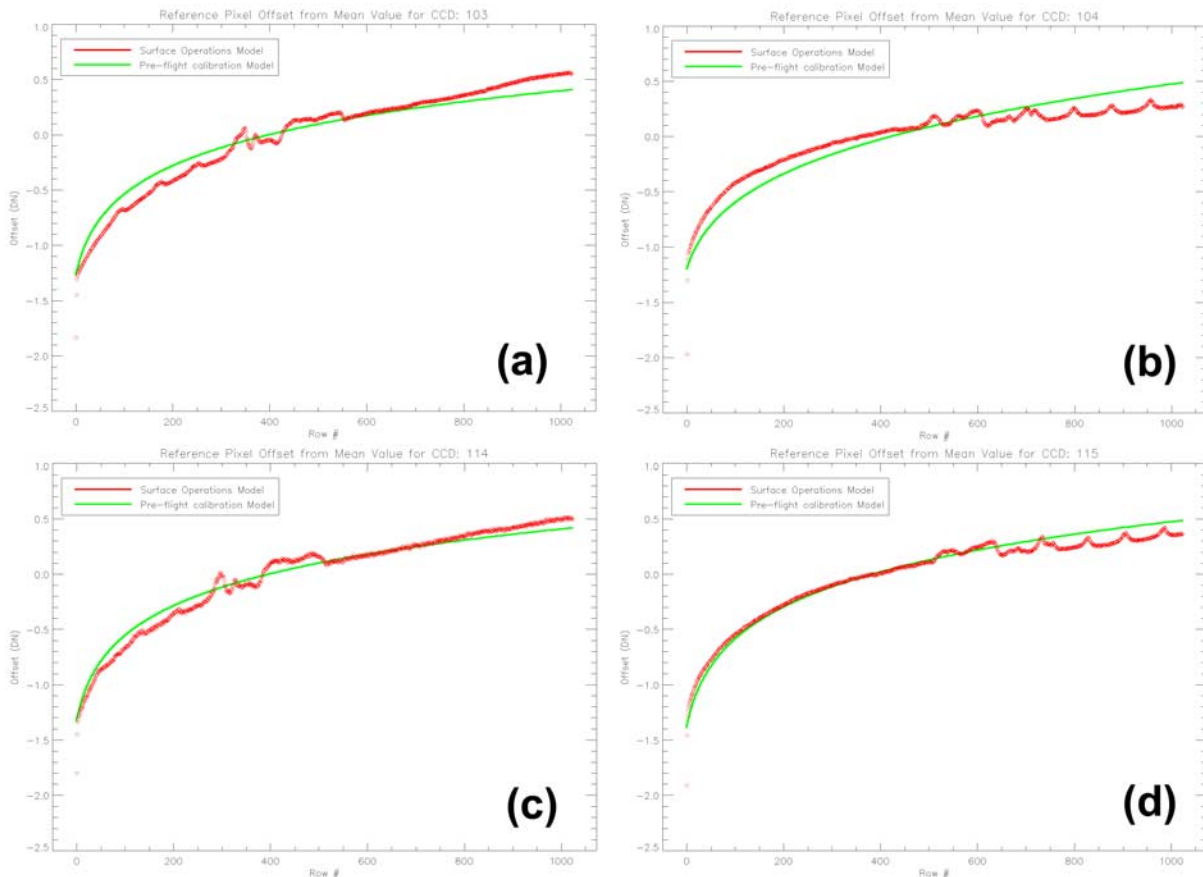


**Figure 4.** Plots of bias level offset from the mean value as a function of CCD row number for (a) the Spirit right Pancam S/N 103; (b) the Spirit left Pancam S/N 104; (c) the Opportunity right Pancam S/N 114; and (d) the Opportunity left Pancam S/N 115. The green curve is the preflight bias offset model developed by *Bell et al.* [2003]. The red curve is the new in-flight bias offset model.

flight dark current model produces similar results in general to the preflight model, but is more robust in terms of modeling pixels near the read-out row as well as extrapolating dark current performance outside the bounds of the in-flight dark current data set and dealing with pixels whose behavior has evolved in flight since the preflight calibration.

### 2.3.1. Masked Area Dark Current Subtraction

[17] To derive our in-flight dark current model for the masked region of the CCD, we use a combination of warm-temperature zero-exposure duration images from preflight calibration and moderate to cold-temperature zero-exposure duration images from flight operations on Mars. Flight dark-current images used to model masked-region and active region dark current are listed in Tables 2 and 3. Warm-temperature dark current images from preflight calibration used in the new model are listed in Tables 4 and 5.

[18] To model the dark current data, we first subtract the bias using the reference pixel images acquired with each sequence, leaving only the signal due to dark current accumulation in the masked region (actually, plus dark current signal accumulated in the active area during the 5 msec frame transfer period, but this component of the dark current signal is insignificant compared to the masked area dark current signal accumulated during the

~5 sec image readout). We then calculate the mean dark current in a central  $256 \times 1024$  pixel box for each image. Testing of various options for the size of this central box revealed the best performance when including all 1024

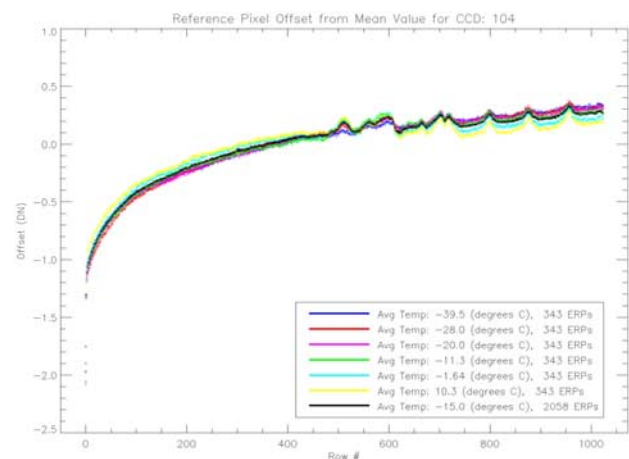


**Figure 5.** Plots of bias level offset from the mean value versus CCD row as a function of electronics box temperature for the Spirit left Pancam S/N 104.

**Table 2.** Spirit/Pancam Flight Dark Current Images Used in the Pancam In-Flight Dark Current Model

| Filename                        | CCD Serial No. | Sol | LTST  | CCD T, °C | Electronics T, °C | Exposure, ms |
|---------------------------------|----------------|-----|-------|-----------|-------------------|--------------|
| 2P126823111EFF0200P2105L8M1.IMG | 104            | 5   | 15:46 | −9.39429  | −6.83737          | 29998.08     |
| 2P126823111EFF0200P2105R8M1.IMG | 103            | 5   | 15:46 | −9.53075  | −6.83737          | 29998.08     |
| 2P126891134EFF0200P2105L8M1.IMG | 104            | 6   | 10:09 | −29.5975  | −34.0211          | 29998.08     |
| 2P126891134EFF0200P2105R8M1.IMG | 103            | 6   | 10:09 | −29.1139  | −34.0211          | 29998.08     |
| 2P127080191EFF0211P2132L8M1.IMG | 104            | 8   | 13:16 | −3.00022  | −5.36129          | 29998.08     |
| 2P127080191EFF0211P2132R8M1.IMG | 103            | 8   | 13:16 | −2.77244  | −5.36129          | 29998.08     |
| 2P127080235EFF0211P2132L8M1.IMG | 104            | 8   | 13:16 | −1.55193  | −4.4525           | 0            |
| 2P127080235EFF0211P2132R8M1.IMG | 103            | 8   | 13:16 | −1.36876  | −4.4525           | 0            |
| 2P127246856EFF0211P2132L8M1.IMG | 104            | 10  | 10:19 | −28.5677  | −28.1762          | 29998.08     |
| 2P127246856EFF0211P2132R8M1.IMG | 103            | 10  | 10:19 | −28.7331  | −28.1762          | 29998.08     |
| 2P127246899EFF0211P2132L8M1.IMG | 104            | 10  | 10:20 | −27.1791  | −26.7353          | 0            |
| 2P127246899EFF0211P2132R8M1.IMG | 103            | 10  | 10:20 | −27.12    | −26.7353          | 0            |
| 2P127256198EFF0214P2132L8M1.IMG | 104            | 10  | 12:51 | −3.00022  | 11.9394           | 29998.08     |
| 2P127256198EFF0214P2132R8M1.IMG | 103            | 10  | 12:51 | −3.90386  | 11.9394           | 29998.08     |
| 2P127256256EFF0214P2132L8M1.IMG | 104            | 10  | 12:52 | −2.09514  | 12.4426           | 0            |
| 2P127256256EFF0214P2132R8M1.IMG | 103            | 10  | 12:52 | −2.9535   | 12.4426           | 0            |
| 2P127264243EFF0224P2132L8M1.IMG | 104            | 10  | 15:01 | −3.40739  | −0.5637           | 29998.08     |
| 2P127264243EFF0224P2132R8M1.IMG | 103            | 10  | 15:02 | −6.21038  | −0.5637           | 29998.08     |
| 2P127264314EFF0224P2132L8M1.IMG | 104            | 10  | 15:03 | −3.18119  | 1.18937           | 0            |
| 2P127264314EFF0224P2132R8M1.IMG | 103            | 10  | 15:03 | −5.57743  | 1.18937           | 0            |
| 2P133288824EFF2232P2105L8M1.IMG | 104            | 78  | 12:01 | −21.0106  | −22.4302          | 29998.08     |
| 2P133288824EFF2232P2105R8M1.IMG | 103            | 78  | 12:01 | −20.724   | −22.4302          | 29998.08     |
| 2P133288867EFF2232P2105L8M1.IMG | 104            | 78  | 12:01 | −19.5278  | −21.4825          | 0            |
| 2P133288867EFF2232P2105R8M1.IMG | 103            | 78  | 12:01 | −19.308   | −21.4825          | 0            |
| 2P133456546EFF2232P2874L8M1.IMG | 104            | 80  | 9:22  | −49.7241  | −20.715           | 120002.6     |
| 2P133456546EFF2232P2874R8M1.IMG | 103            | 80  | 9:22  | −48.2532  | −20.715           | 120002.6     |
| 2P133456701EFF2232P2105L8M1.IMG | 104            | 80  | 9:25  | −47.3479  | −9.58283          | 0            |
| 2P133456701EFF2232P2874R8M1.IMG | 103            | 80  | 9:25  | −45.8968  | −9.58283          | 0            |
| 2P133469365EFF2232P2105L8M1.IMG | 104            | 80  | 12:50 | −12.7993  | 3.49071           | 29998.08     |
| 2P133469365EFF2232P2105R8M1.IMG | 103            | 80  | 12:50 | −13.5229  | 3.49071           | 29998.08     |
| 2P133469409EFF2232P2105L8M1.IMG | 104            | 80  | 12:51 | −11.3567  | 3.44512           | 0            |
| 2P133469409EFF2232P2105R8M1.IMG | 103            | 80  | 12:51 | −12.3733  | 3.44512           | 0            |
| 2P139324380EFF58BQP2105L8M1.IMG | 104            | 146 | 12:06 | −27.56    | −30.2235          | 29998.08     |
| 2P139324380EFF58BQP2105R8M1.IMG | 103            | 146 | 12:06 | −26.8958  | −30.2235          | 29998.08     |
| 2P139324423EFF58BQP2105L8M1.IMG | 104            | 146 | 12:07 | −26.1036  | −29.1663          | 0            |
| 2P139324423EFF58BQP2105R8M1.IMG | 103            | 146 | 12:07 | −25.4833  | −29.1663          | 0            |
| 2P139421376EFF5906P2105L8M1.IMG | 104            | 147 | 14:20 | −23.7266  | −26.0146          | 29998.08     |
| 2P139421376EFF5906P2105R8M1.IMG | 103            | 147 | 14:20 | −22.4312  | −26.0146          | 29998.08     |
| 2P139421420EFF5906P2105L8M1.IMG | 104            | 147 | 14:20 | −22.3577  | −24.5273          | 0            |
| 2P139421420EFF5906P2105R8M1.IMG | 103            | 147 | 14:20 | −21.1285  | −24.5273          | 0            |
| 2P139495357EFF6002P2105L8M1.IMG | 104            | 148 | 10:20 | −46.748   | −49.398           | 29998.08     |
| 2P139495357EFF6002P2105R8M1.IMG | 103            | 148 | 10:20 | −49.6081  | −49.398           | 29998.08     |
| 2P139495401EFF6002P2105L8M1.IMG | 104            | 148 | 10:21 | −45.214   | −48.1259          | 0            |
| 2P139495401EFF6002P2105R8M1.IMG | 103            | 148 | 10:21 | −48.0532  | −48.1259          | 0            |
| 2P139602383EFF6104P2105L8M1.IMG | 104            | 149 | 15:16 | −20.4715  | −0.5637           | 29998.08     |
| 2P139602383EFF6104P2105R8M1.IMG | 103            | 149 | 15:16 | −21.8024  | −0.5637           | 29998.08     |
| 2P139602427EFF6104P2105L8M1.IMG | 104            | 149 | 15:17 | −19.1682  | −0.72301          | 0            |
| 2P139602427EFF6104P2105R8M1.IMG | 103            | 149 | 15:17 | −20.7465  | −0.72301          | 0            |

pixels along the readout axis of the CCD, which is perhaps not unexpected since the dark current can vary significantly along this dimension during the  $\sim 5$  sec readout time for the CCD masked region. We fit an exponential function to the mean dark-current values (weighting each value by an estimate of its uncertainty) in the following form:

$$dark\_current_{box\_mean} = a_0 \exp(a_1 T) \quad (2)$$

as shown in Figure 6, where  $dark\_current_{box\_mean}$  is the total dark current DN accumulated over the  $\sim 5$  sec readout time of the masked region. The best-fit model coefficients are listed in Table 6. As expected, images taken at higher temperatures yield much more dark current, and as a consequence, these images produced results with higher signal-to-noise ratio (SNR). The deviation between the data and the model at very low temperatures (which is small in an absolute sense) is a result of noise in the measurement of the bias and the quantum nature of the analog-to-digital encoding of the detector voltage. We

found (as expected) that the  $a_0$  and  $a_1$  coefficients were very close to the mean of the coefficient images that we had generated in the preflight model [Bell et al., 2003].

[19] Because of the limitations in the pixel-by-pixel preflight dark current modeling noted above, we modified our modeling approach using a combination of preflight and in-flight dark measurements. First, a relative dark current value or “dark-flat” was derived for each column. These column dark-flats were derived exclusively from images taken at very warm temperatures during preflight calibration (Tables 4 and 5). Each column’s dark-flat was found by dividing the dark current values in each column by the mean dark current value of that column. The shapes of these dark-flats were found to be consistent across temperature for all columns, as shown in Figure 7. Therefore, by using only the warm temperature images, we were able to reduce any (possibly cumulative) effects due to low SNR or low DN value sampling. In the description below, the mean dark current value for column  $i$  will be referred to

**Table 3.** Opportunity/Pancam Flight Dark Current Images Used in the Pancam In-Flight Dark Current Model

| Filename                        | CCD Serial No. | Sol | LTST  | CCD T, °C | Electronics T, °C | Exposure, ms |
|---------------------------------|----------------|-----|-------|-----------|-------------------|--------------|
| 1P128534493EFF0203P2850L8M1.IMG | 115            | 4   | 10:24 | −23.7444  | −22.6169          | 29998.08     |
| 1P128534493EFF0203P2850R8M1.IMG | 114            | 4   | 10:24 | −23.6001  | −22.6169          | 29998.08     |
| 1P128534537EFF0203P2850L8M1.IMG | 115            | 4   | 10:25 | −22.3131  | −21.1785          | 0            |
| 1P128534537EFF0203P2850R8M1.IMG | 114            | 4   | 10:25 | −22.0751  | −21.1785          | 0            |
| 1P128549912EFF0205P2850L8M1.IMG | 115            | 4   | 14:34 | 4.31592   | 24.7684           | 29998.08     |
| 1P128549912EFF0205P2850R8M1.IMG | 114            | 4   | 14:34 | 3.49545   | 24.7684           | 29998.08     |
| 1P128549955EFF0205P2850L8M1.IMG | 115            | 4   | 14:35 | 5.5372    | 24.4021           | 0            |
| 1P128549955EFF0205P2850R8M1.IMG | 114            | 4   | 14:35 | 4.47022   | 24.4021           | 0            |
| 1P129081110EFF0224P2850L8M1.IMG | 115            | 10  | 14:11 | 2.46252   | 8.03972           | 29998.08     |
| 1P129081110EFF0224P2850R8M1.IMG | 114            | 10  | 14:11 | 0.980919  | 8.03972           | 29998.08     |
| 1P129081154EFF0224P2850L8M1.IMG | 115            | 10  | 14:12 | 3.77332   | 8.4947            | 0            |
| 1P129081154EFF0224P2850R8M1.IMG | 114            | 10  | 14:12 | 2.33981   | 8.4947            | 0            |
| 1P129598881EFF0312P2855L8M1.IMG | 115            | 16  | 10:11 | −34.0742  | −36.9553          | 29998.08     |
| 1P129598881EFF0312P2855R8M1.IMG | 114            | 16  | 10:11 | −34.204   | −36.9553          | 29998.08     |
| 1P129598924EFF0312P2855L8M1.IMG | 115            | 16  | 10:12 | −32.4707  | −35.7934          | 0            |
| 1P129598924EFF0312P2855R8M1.IMG | 114            | 16  | 10:12 | −32.5292  | −35.7934          | 0            |
| 1P129618112EFF0322P2855L8M1.IMG | 115            | 16  | 15:23 | −4.95997  | 15.3521           | 29998.08     |
| 1P129618112EFF0322P2855R8M1.IMG | 114            | 16  | 15:23 | −4.17617  | 15.3521           | 29998.08     |
| 1P129618210EFF0322P2855L8M1.IMG | 115            | 16  | 15:25 | −4.71216  | 15.6943           | 0            |
| 1P129618210EFF0322P2855R8M1.IMG | 114            | 16  | 15:25 | −3.9728   | 15.6943           | 0            |
| 1P133242555EFF0700P2105L8M1.IMG | 115            | 57  | 11:26 | −22.7604  | −24.9526          | 29998.08     |
| 1P133242555EFF0700P2105R8M1.IMG | 114            | 57  | 11:26 | −23.1741  | −24.9526          | 29998.08     |
| 1P133242598EFF0700P2105L8M1.IMG | 115            | 57  | 11:27 | −21.2838  | −23.9423          | 0            |
| 1P133242598EFF0700P2105R8M1.IMG | 114            | 57  | 11:27 | −21.5367  | −23.9423          | 0            |
| 1P133346212EFF0830P2105L8M1.IMG | 115            | 58  | 15:28 | −6.9416   | 14.7134           | 29998.08     |
| 1P133346212EFF0830P2105R8M1.IMG | 114            | 58  | 15:28 | −7.45038  | 14.7134           | 29998.08     |
| 1P133346281EFF0830P2105L8M1.IMG | 115            | 58  | 15:29 | −6.42383  | 14.9187           | 0            |
| 1P133346281EFF0830P2105R8M1.IMG | 114            | 58  | 15:29 | −6.77331  | 14.9187           | 0            |
| 1P133509100EFF0830P2105L8M1.IMG | 115            | 60  | 11:31 | −17.7901  | −19.0642          | 29998.08     |
| 1P133509100EFF0830P2105R8M1.IMG | 114            | 60  | 11:31 | −19.0672  | −19.0642          | 29998.08     |
| 1P133509144EFF0830P2105L8M1.IMG | 115            | 60  | 11:31 | −16.4226  | −17.5337          | 0            |
| 1P133509144EFF0830P2105R8M1.IMG | 114            | 60  | 11:31 | −17.5619  | −17.5337          | 0            |
| 1P133525695EFF0830P2105L8M1.IMG | 115            | 60  | 16:00 | −10.5855  | 12.4109           | 29998.08     |
| 1P133525695EFF0830P2105R8M1.IMG | 114            | 60  | 16:00 | −11.2611  | 12.4109           | 29998.08     |
| 1P133525768EFF0830P2105L8M1.IMG | 115            | 60  | 16:01 | −10.2258  | 12.5477           | 0            |
| 1P133525768EFF0830P2105R8M1.IMG | 114            | 60  | 16:01 | −10.7203  | 12.5477           | 0            |
| 1P139022037EFF2809P2105L8M1.IMG | 115            | 122 | 14:17 | −14.3138  | 6.22061           | 29998.08     |
| 1P139022037EFF2809P2105R8M1.IMG | 114            | 122 | 14:17 | −16.7077  | 6.22061           | 29998.08     |
| 1P139115066EFF2815P2105L8M1.IMG | 115            | 123 | 15:26 | −19.224   | −4.66652          | 29998.08     |
| 1P139115066EFF2815P2105R8M1.IMG | 114            | 123 | 15:26 | −17.7866  | −4.66652          | 29998.08     |
| 1P139115109EFF2815P2105L8M1.IMG | 115            | 123 | 15:27 | −17.9693  | −4.14592          | 0            |
| 1P139115109EFF2815P2105R8M1.IMG | 114            | 123 | 15:27 | −17.0899  | −4.14592          | 0            |
| 1P139365263EFF2829P2105L8M1.IMG | 115            | 126 | 11:06 | −31.4457  | −33.3338          | 29998.08     |
| 1P139365263EFF2829P2105R8M1.IMG | 114            | 126 | 11:06 | −32.7079  | −33.3338          | 29998.08     |
| 1P139365307EFF2829P2105L8M1.IMG | 115            | 126 | 11:06 | −30.0635  | −31.7225          | 0            |
| 1P139365307EFF2829P2105R8M1.IMG | 114            | 126 | 11:06 | −31.1439  | −31.7225          | 0            |

as  $cm_{(i)}$ , the dark-flat for column  $i$  will be referred to as  $cf_{(i)}$  (a  $1 \times 1024$  column vector), and  $cf_{(i,j)}$  is the column flat value for a given pixel  $(i, j)$ .

[20] We then normalized the array of  $cm_{(i)}$  values in each image by dividing by the calculated mean from the central box described above. We will refer to this normalized array as the “column mean dark-flat.” Ideally, the column mean dark flats would be consistent across temperature, implying the same exponential coefficient for each pixel. We found this to be the case for most columns (especially those far from the edges of the detector), but we found that approaching the edges of the CCD, the column mean dark flat values tended to increase slightly with temperature. This is consistent with our preflight model in which the exponential coefficients for each pixel increase toward the edges [Bell *et al.*, 2003, Figure 16]. In the description below, the column mean dark flat value for column  $i$  will be referred to as  $cmf_{(i)}$ .

[21] We do not yet have sufficient flight data to accurately characterize the temperature dependence of  $cmf_{(i)}$  and so we

have chosen to model it as constant with temperature. In calculating the value of  $cmf_{(i)}$ , data points are weighted by the DN value of the dark current. This gives a higher weighting to those data points with higher SNR, de-emphasizing the contribution of colder images where the dark current is a much smaller percentage of the overall signal. Plots of  $cmf_{(i)}$  are shown in Figure 8.

[22] One final step is needed for proper modeling of the masked region dark current during flight operations, to account for pixels in the masked region of the CCD that have changed their behavior or become “hot” since the start of the mission. There were no observed changes in dark current behavior during preflight calibration, but the different radiation environment during cruise and on the surface of Mars compared to the environment on Earth has apparently resulted in “damage” to a small number of pixels on the four flight Pancam CCDs.

[23] “Hot” pixels are those which accumulate charge at a much faster rate than average, and they have an interesting effect on the masked region dark current. Because of the



**Table 4.** Spirit/Pancam High-Temperature (>25°C) Preflight Dark Current Images Used in the Pancam In-Flight Dark Current Model

| Filename                        | CCD S/N |
|---------------------------------|---------|
| 020801180219_0000000_R2_103.IMG | 103     |
| 020801210245_0000000_R2_103.IMG | 103     |
| 020801230219_0000000_R2_103.IMG | 103     |
| 020802002818_0000000_R2_103.IMG | 103     |
| 020802013200_0000000_R2_103.IMG | 103     |
| 020802033319_0000000_R2_103.IMG | 103     |
| 020802071000_0000000_R2_103.IMG | 103     |
| 020802081634_0000000_R2_103.IMG | 103     |
| 020802091841_0000000_R2_103.IMG | 103     |
| 020802150210_0000000_R1_103.IMG | 103     |
| 020802180304_0000000_R1_103.IMG | 103     |
| 020802190519_0000000_R1_103.IMG | 103     |
| 020802210144_0000000_R1_103.IMG | 103     |
| 020802230153_0000000_L1_104.IMG | 103     |
| 020803000242_0000000_R1_103.IMG | 103     |
| 020803070839_0000000_R1_103.IMG | 103     |
| 020803090457_0000000_R1_103.IMG | 103     |
| 020805174528_0000000_L1_104.IMG | 104     |
| 020805191343_0000000_L1_104.IMG | 104     |
| 020805220326_0000000_L1_104.IMG | 104     |
| 020806010608_0000000_L1_104.IMG | 104     |
| 020806020737_0000000_L1_104.IMG | 104     |
| 020806040732_0000000_L1_104.IMG | 104     |
| 020806080733_0000000_L1_104.IMG | 104     |
| 020806110940_0000000_L1_104.IMG | 104     |
| 020806140841_0000000_L1_104.IMG | 104     |
| 020806151211_0000000_L1_104.IMG | 104     |
| 020806190222_0000000_L1_104.IMG | 104     |
| 020806210241_0000000_L1_104.IMG | 104     |

way rows are clocked out during readout [Bell et al., 2003], a hot pixel in the masked region will affect every pixel in the same column that is upstream (away from the readout register) of it. Therefore, instead of a smooth column dark-flat, a column with a hot pixel will have a discontinuity, as shown in Figure 9. A small number of columns in each CCD have hot pixels in the masked region that are “hot enough” to cause a noticeable effect. Most of these can be seen in the initial flight dark images taken during the first 10 sols, but some have appeared later in the mission. Lists of hot pixels for each CCD as of February 2005, along with the magnitude of their associated offset and the mission time when they were first noted, are provided in Tables 7 and 8.

[24] Because each image pixel clocks through the hot pixel for the same duration ( $\sim 5 \mu\text{sec}$ ), the effect is the same as adding a constant to  $cf_{(i,j)}$  for  $j$  greater than or equal to the row number of the hot pixel. The size of the constant can be easily calculated by choosing the constant that yields the best fit between the model and the flight data. We therefore must remove the effect of any hot pixels when calculating  $cmf_{(i)}$ . This “hot pixel correction” adds one additional term to our model, and makes the hot pixel corrected column dark-flat ( $hcf_{(i,j)}$ ) dependent upon the time when an image was taken. Thus

$$hcf_{(i,j)} = cf_{(i,j)} + hot\_offset_{(i,j)}(SCLK) \quad (3)$$

where  $cf_{(i,j)}$  are the preflight-derived column flat values for each pixel  $(i,j)$ , and  $hot\_offset_{(i,j)}(SCLK)$  are the hot pixel offset constants for pixel  $(i,j)$  listed in Tables 7 and 8. The hot pixel offset constants will only be nonzero for pixels in the same column as a hot pixel, in a row equal to or

upstream from that hot pixel, and only for images taken after the Spacecraft CLoK (SCLK) time for each rover that the hot pixel was first observed.

[25] Therefore the new model for the masked region dark current becomes

$$masked\_dark\_current_{(i,j)}(T) = a_0 \exp(a_1 T) cmf_{(i)} hcf_{(i,j)} \quad (4)$$

where  $T$  is the CCD temperature (estimated from equation (9) as described below),  $a_0$  and  $a_1$  are from equation (2),  $cmf_{(i)}$  are calculated as described above and shown in Figure 8, and  $hcf_{(i,j)}$  is from equation (3).

### 2.3.2. Active Area Dark Current Subtraction

[26] Each dark current imaging sequence taken during the mission includes a long-exposure dark image immediately followed by a zero-exposure dark image. The zero exposure image is subtracted from the long-exposure, leaving signal due exclusively to dark current accumulated in the active region of the CCD. Dividing the accumulated active region dark current by the exposure duration gives us a dark current rate.

[27] As in the model for the masked region, in our new model for the active region dark current we use a central box in the image to determine the mean value for the dark current rate. For the active region of the CCD, we use a  $256 \times 256$  pixel central box to avoid edge effects like those noted above. We then normalize the image by dividing by the mean value in the central box to generate a “dark current rate flat field” for the active region of the CCD. We fit an error-weighted exponential to this mean active dark current rate of the form

$$dark\_current\_rate_{box\_mean} = c_0 \exp(c_1 T) \quad (5)$$

where  $dark\_current\_rate_{box\_mean}$  is the dark current accumulation rate in the active region in DN per second of exposure duration.

**Table 5.** Opportunity Pancam High-Temperature (>25°C) Preflight Dark Current Images Used in the Pancam In-Flight Dark Current Model

| Filename                        | CCD S/N |
|---------------------------------|---------|
| 020905113112_0000000_R8_114.IMG | 114     |
| 020905155354_0000000_R8_114.IMG | 114     |
| 020905200320_0000000_R8_114.IMG | 114     |
| 020905234957_0000000_R8_114.IMG | 114     |
| 020906051134_0000000_R8_114.IMG | 114     |
| 020906105424_0000000_R8_114.IMG | 114     |
| 020906154507_0000000_R8_114.IMG | 114     |
| 020906195622_0000000_R8_114.IMG | 114     |
| 020906235821_0000000_R8_114.IMG | 114     |
| 020904104928_0000000_L8_115.IMG | 115     |
| 020904104943_0000000_L8_115.IMG | 115     |
| 020908090520_0000000_L8_115.IMG | 115     |
| 020908173506_0000000_L1_115.IMG | 115     |
| 020909075621_0000000_L1_115.IMG | 115     |
| 020909125759_0000000_L1_115.IMG | 115     |
| 020909170656_0000000_L1_115.IMG | 115     |
| 020909210724_0000000_L1_115.IMG | 115     |
| 020910010523_0000000_L1_115.IMG | 115     |
| 020910045954_0000000_L1_115.IMG | 115     |
| 020924180037_0000000_L8_115.IMG | 115     |
| 020924180051_0000000_L8_115.IMG | 115     |
| 020924180106_0000000_L8_115.IMG | 115     |
| 020924180121_0000000_L8_115.IMG | 115     |
| 020924180134_0000000_L8_115.IMG | 115     |

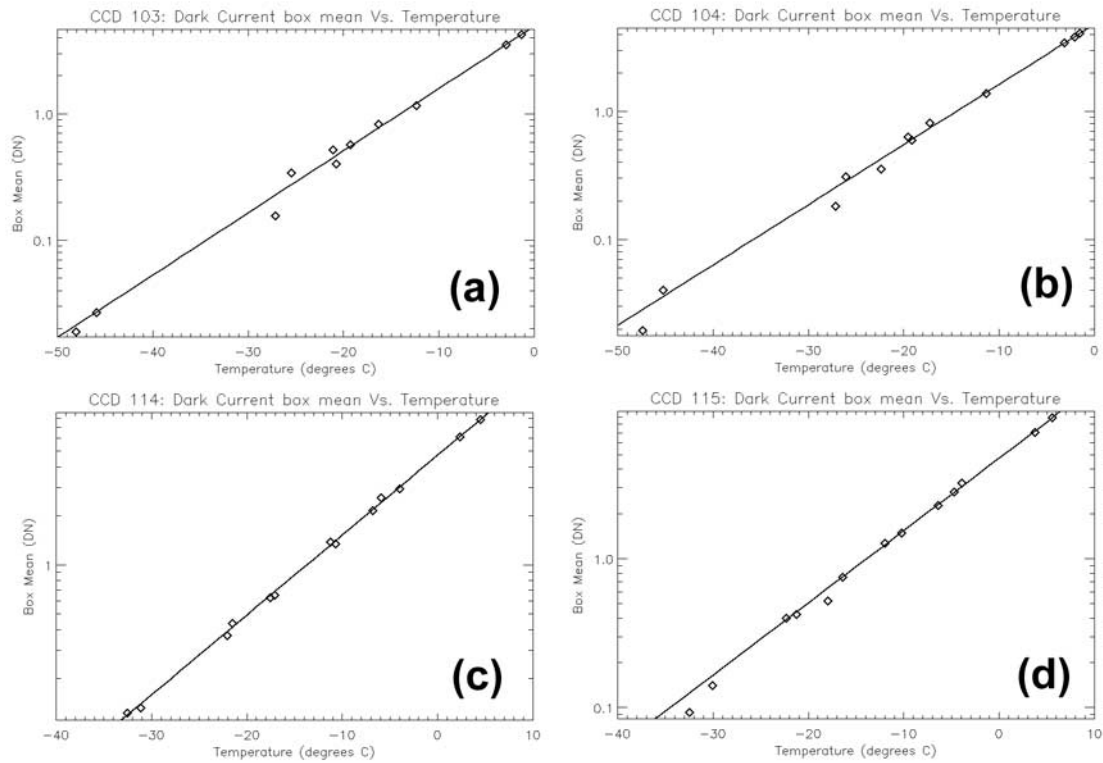


**Figure 6.** Linear-log plots of masked region dark current signal (Data Number) as a function of CCD temperature for (a) the Spirit right Pancam S/N 103; (b) the Spirit left Pancam S/N 104; (c) the Opportunity right Pancam S/N 114; and (d) the Opportunity left Pancam S/N 115. The solid curve is the fit to the data using equation (2) and the coefficients listed in Table 6.

[28] In our preflight active area dark current model [Bell *et al.*, 2003], the CCD warming that occurred during the exposure was approximated by estimating an average temperature for the duration of the exposure, based on temperature trends that were observed and manually recorded during calibration. For multiimage sequences, only a single temperature (at the beginning of the sequence) was recorded. In either case, the recorded temperature could differ from the actual temperature by 5–10°C or more if the CCD cooled between the time the temperature was recorded and the time the images were acquired. The presence of these uncertainties, analysis of CCD temperature variations seen during Microscopic Imager calibration [Herkenhoff *et al.*, 2003], and in-flight observations of the actual cooling and heating patterns of the Pancam CCD and electronics (Figure 2) compelled us to develop a model for this effect.

[29] Under steady state laboratory background conditions (a constant ambient temperature of around 25°C, which is a factor of the environmental temperature as well as other factors such as conduction through support structures, radiant

heat from nearby electronics, etc.), the maximum possible increase in CCD temperature was observed to be a constant regardless of the initial starting temperature of the CCD. To model this increase in temperature  $\Delta T$ , we used the equation

$$\Delta T(t) = m(1 - e^{(-t/c)}) \quad (6)$$

where  $m$  is the maximum possible increase in temperature,  $t$  is the exposure duration and  $c$  is a time constant in seconds (the time it takes for the temperature to increase  $(1 - 1/e)$  or about 63% of the way from the current temperature to the maximum possible temperature). From temperature measurements taken carefully during long exposures, we found the time constant  $c$  to be about 70 seconds (Figure 10). If the temperature of the CCD at the start of the exposure is above the ambient temperature by an amount  $d$ , then the equation becomes

$$\Delta T(t) = (m - d)(1 - e^{(-t/c)}) \quad (7)$$

**Table 6.** Pancam In-Flight Dark Current Model Parameters

| Camera                    | S/N | Equation (2) |          | Equation (5) |          |
|---------------------------|-----|--------------|----------|--------------|----------|
|                           |     | $a_0$ (DN)   | $a_1$    | $c_0$ (DN/s) | $c_1$    |
| MER-A (Spirit) right      | 103 | 4.93762      | 0.113328 | 14.3663      | 0.104952 |
| MER-A (Spirit) left       | 104 | 4.79902      | 0.108246 | 15.0241      | 0.106693 |
| MER-B (Opportunity) right | 114 | 4.73198      | 0.113069 | 15.0165      | 0.099872 |
| MER-B (Opportunity) left  | 115 | 4.74433      | 0.111948 | 13.4111      | 0.102246 |

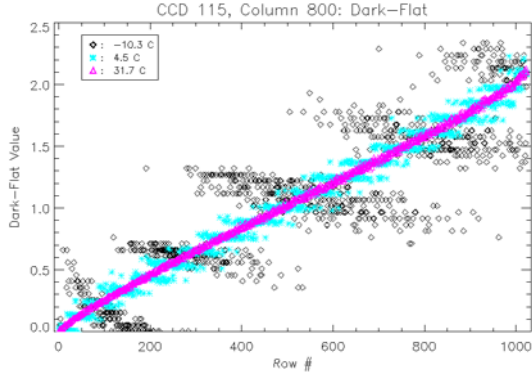


**Figure 7.** Representative “dark-flat” data for each row in CCD column 800 in the Opportunity left Pancam S/N 115, as a function of CCD temperature. The “dark-flat” value is the dark current in each pixel divided by the mean dark in that column. The SNR is lower at lower temperatures (less dark current), but the trends of the dark-flat curves are generally the same.

and therefore the temperature at time  $t$  is

$$T(t) = T_s + \Delta T(t) \quad (8)$$

where  $T_s$  is the temperature at the start of the exposure. This is slightly problematic, as it requires knowledge of the ambient temperature of the CCD and so may be difficult to

know. To generate our model from the preflight calibration data [Bell *et al.*, 2003], we used only the first image from any given set of dark images for a given exposure duration, with the assumption that the initial CCD temperature was therefore close to the ambient temperature and that the CCD had had a chance to equilibrate since the previous sequence of images.

[30] For flight data, the calculation of the ambient temperature is more problematic. The dark images that we are using to create our model are the first and only images taken during special dark imaging sequences. Therefore we are working under the assumption that the CCD temperature returned with the image is the “ambient” temperature. We hope eventually to refine this estimate using temperature telemetry data recorded separately prior to the image acquisition to help us model the “ambient” temperature for a given image. The coefficients that we used for our flight data CCD temperature increase model in equation (7) are  $m = 3$ ,  $t = 70$ , and  $d = 0$ , based on the average time constant derived from preflight data and the maximum  $\Delta T$  of the data shown in Figure 10. Therefore, modifying equation (8), we calculate  $T_{end}$ , the expected temperature at the end of an exposure of duration  $E$ , as

$$T_{end} = T_s + \Delta T(E) \quad (9)$$

We also use  $T_{end}$  as the CCD temperature in the calculation of the masked-region dark current (equation (4)) because the

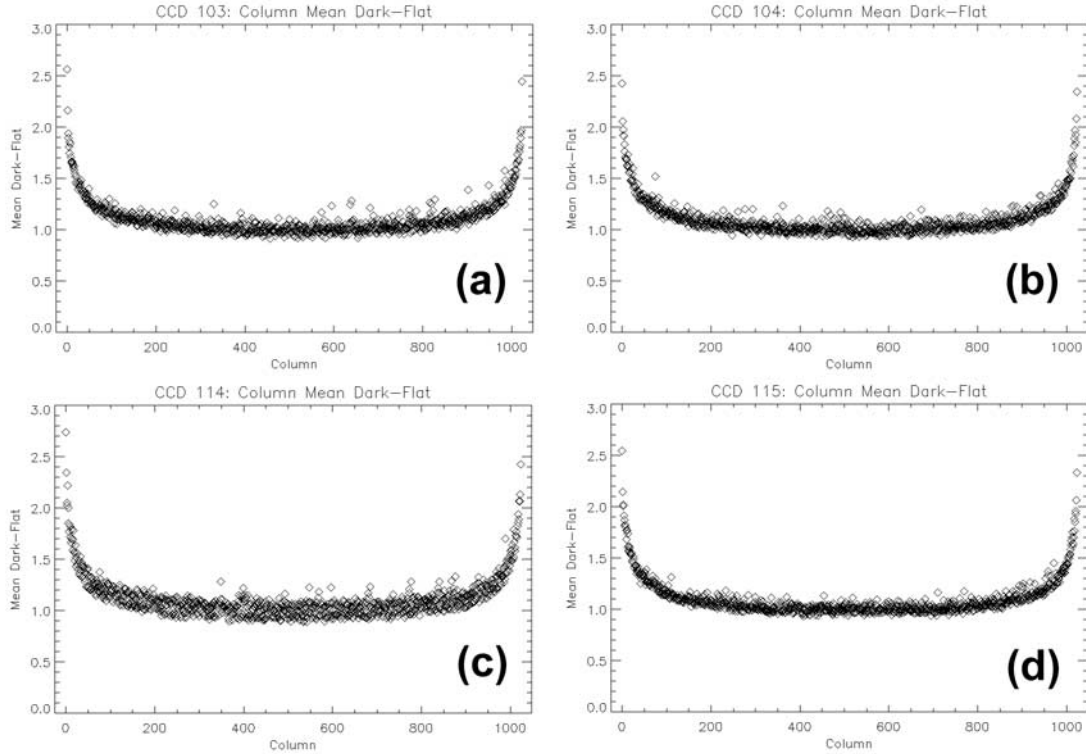


**Figure 8.** Plots of “column mean dark-flat” values for each CCD column in (a) the Spirit right Pancam S/N 103; (b) the Spirit left Pancam S/N 104; (c) the Opportunity right Pancam S/N 114; and (d) the Opportunity left Pancam S/N 115. The column mean dark-flat value for each column is the mean of the dark current in each column normalized by the average dark current value from a box in the central region of each image.

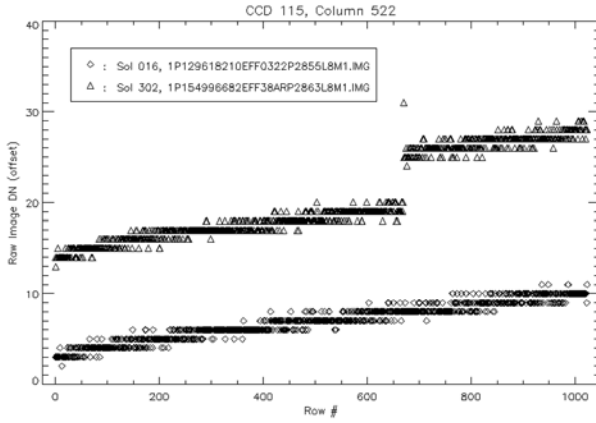


**Figure 9.** Example of the effect of a “hot pixel” in CCD column 522 in the Opportunity left Pancam S/N 115 dark-flat data. The diamonds show the dark-flat values from sol 16 (9 February 2004) data. The triangles show the dark-flat values from sol 302 (29 November 2004), and show that a new “hot” pixel appeared on the array near row 650. The effects of this hot pixel propagate downstream to other pixels and manifest themselves as an additive offset in the dark-flat value (Tables 7 and 8).

time the image spends in the masked region occurs after the end of the integration time. Because the CCD temperature is changing over the course of the exposure and the dark current rate is expected to be exponential with temperature, it follows that the dark current rate is changing over the course of the exposure. Therefore we attempt to model an average rate of dark current accumulation, which when multiplied by the exposure duration, gives the total accumulated dark current.

[31] If we assume that the instantaneous dark current accumulation rate is described by equation (5), then based on our temperature model, over the duration of an exposure of duration  $E$ , the total dark current should amount to

$$D_{\text{tot}} = \int_0^E c_0 e^{c_1 T(t)} dt \quad (10)$$

and, thus

$$D_{\text{tot}} = \int_0^E c_0 e^{c_1 [T_s + m(1 - e^{-t/c})]} dt \quad (11)$$

for which, unfortunately, we cannot compute an analytical solution. As a close approximation, however, we calculate the average temperature over the course of the exposure and use that directly.

[32] The average temperature can be estimated by integrating the temperature over the exposure duration and dividing by the exposure duration.

$$T_{\text{avg}} = T_s + \left\{ \int_0^E m(1 - e^{-t/c}) dt \right\} / E \quad (12)$$

and thus

$$T_{\text{avg}} = T_s + (m/E) [E - c(1 - e^{-E/c})] \quad (13)$$

The total mean active area dark current can then be approximated as

$$\text{active\_dark\_current}_{\text{box\_mean}} = E c_0 \exp(c_1 T_{\text{avg}}) \quad (14)$$

[33] Performing a numerical integration to check the closeness of this approximation to the precise integral, we find that this approximation results in an error in total active area dark current of less than one part in a thousand for a 60 second exposure at 0°C, and even smaller error for shorter exposures or lower temperatures, both of which are more typical for actual in-flight images.

[34] Therefore, given approximations for  $T_{\text{end}}$  and  $T_{\text{avg}}$ , we can remove the masked region dark current and fit an exponential to the mean dark current accumulation rate in the central box of the active region. An example for the Opportunity left Pancam (S/N 115) is shown in Figure 11.

**Table 7.** Spirit Pancam In-flight “Hot Pixel” Dark Offset<sup>a</sup>

| Spirit Right<br>Pancam, S/N 103 |     |        |           | Spirit Left<br>Pancam, S/N 104 |     |        |           |
|---------------------------------|-----|--------|-----------|--------------------------------|-----|--------|-----------|
| Col                             | Row | Offset | SCLK      | Col                            | Row | Offset | SCLK      |
| 994                             | 9   | 2.170  | 126470000 | 833                            | 254 | 4.364  | 126470000 |
| 980                             | 437 | 0.651  | 126470000 | 24                             | 280 | 0.625  | 126470000 |
| 549                             | 11  | 0.805  | 126470000 | 714                            | 911 | 0.937  | 126470000 |
| 330                             | 405 | 0.587  | 126470000 | 540                            | 515 | 0.814  | 126470000 |
| 158                             | 965 | 0.543  | 126470000 | 558                            | 691 | 0.748  | 126470000 |
| 336                             | 259 | 0.457  | 126470000 | 902                            | 463 | 0.574  | 126470000 |
| 675                             | 500 | 0.440  | 126470000 | 843                            | 545 | 0.510  | 126470000 |
| 453                             | 145 | 0.432  | 126470000 | 57                             | 100 | 0.397  | 126470000 |
| 182                             | 220 | 0.367  | 126470000 | 642                            | 526 | 0.485  | 126470000 |
| 482                             | 372 | 0.389  | 126470000 | 591                            | 409 | 0.427  | 126470000 |
| 928                             | 828 | 0.322  | 126470000 | 701                            | 741 | 0.429  | 126470000 |
| 198                             | 401 | 0.297  | 126470000 | 716                            | 474 | 0.461  | 126470000 |
| 998                             | 394 | 0.219  | 126470000 | 1019                           | 94  | 0.193  | 126470000 |
| 985                             | 83  | 0.200  | 126470000 | 40                             | 580 | 0.278  | 126470000 |
| 986                             | 446 | 0.182  | 126470000 | 969                            | 285 | 0.263  | 126470000 |
| 456                             | 96  | 0.261  | 126470000 | 89                             | 833 | 0.264  | 126470000 |
| 840                             | 781 | 0.218  | 126470000 | 81                             | 539 | 0.257  | 126470000 |
| 941                             | 639 | 0.200  | 126470000 | 455                            | 637 | 0.269  | 126470000 |
| 14                              | 303 | 0.142  | 126470000 | 981                            | 538 | 0.198  | 126470000 |
| 922                             | 461 | 0.188  | 126470000 | 569                            | 252 | 0.282  | 126470000 |
| 650                             | 278 | 0.215  | 126470000 | 164                            | 942 | 0.260  | 126470000 |
| 306                             | 950 | 0.200  | 126470000 | 687                            | 810 | 0.248  | 126470000 |
| 140                             | 431 | 0.157  | 126470000 | 739                            | 436 | 0.238  | 126470000 |
| 179                             | 918 | 0.180  | 126470000 | 299                            | 433 | 0.250  | 126470000 |
| 425                             | 244 | 0.174  | 126470000 | 75                             | 534 | 0.198  | 126470000 |
| 927                             | 925 | 0.153  | 126470000 | 723                            | 372 | 0.222  | 126470000 |
| 2                               | 177 | 0.079  | 126470000 | 787                            | 529 | 0.226  | 126470000 |
| 240                             | 610 | 0.143  | 126470000 | 347                            | 308 | 0.220  | 126470000 |
| 654                             | 657 | 0.155  | 126470000 | 413                            | 379 | 0.216  | 126470000 |
| 855                             | 301 | 0.772  | 127240000 | 757                            | 462 | 0.185  | 126470000 |
| 653                             | 913 | 0.378  | 127240000 | 804                            | 902 | 0.201  | 126470000 |
| 606                             | 60  | 0.343  | 127240000 | 496                            | 521 | 0.188  | 126470000 |
| 381                             | 976 | 0.186  | 127240000 | 461                            | 434 | 0.179  | 126470000 |
| 492                             | 102 | 0.219  | 127240000 | 254                            | 462 | 0.172  | 126470000 |
| 852                             | 88  | 0.158  | 127240000 | 258                            | 447 | 0.170  | 126470000 |
| 6                               | 845 | 0.309  | 133450000 | 709                            | 656 | 0.143  | 126470000 |
| 778                             | 316 | 1.022  | 154060000 | 797                            | 950 | 0.390  | 127240000 |
| 831                             | 885 | 1.946  | 154060000 | 759                            | 591 | 0.186  | 127240000 |
|                                 |     |        |           | 45                             | 458 | 0.119  | 127240000 |
|                                 |     |        |           | 498                            | 644 | 0.166  | 127240000 |
|                                 |     |        |           | 430                            | 119 | 4.049  | 133280000 |

<sup>a</sup>Notes: Col(umn) and Row are defined such that (0,0) is the pixel in the upper left corner of each image. Offset is the additive offset in DN resulting from the hot pixel at the given coordinates. SCLK is the Spacecraft Clock counter time after which the pixel at those coordinates became “hot.” By MER convention, SCLK is the number of seconds since 1 January 2000 at 11:58:55 UTC.



**Table 8.** Opportunity Pancam In-Flight “Hot Pixel” Dark Offset<sup>a</sup>

| Opportunity Right Pancam, S/N 114 |     |        |           | Opportunity Left Pancam, S/N 115 |     |        |           |
|-----------------------------------|-----|--------|-----------|----------------------------------|-----|--------|-----------|
| Col                               | Row | Offset | SCLK      | Col                              | Row | Offset | SCLK      |
| 567                               | 553 | 1.969  | 128280000 | 258                              | 487 | 0.724  | 128280000 |
| 672                               | 716 | 0.541  | 128280000 | 114                              | 445 | 0.335  | 128280000 |
| 785                               | 848 | 0.511  | 128280000 | 303                              | 682 | 0.324  | 128280000 |
| 53                                | 948 | 0.383  | 128280000 | 631                              | 832 | 0.279  | 128280000 |
| 982                               | 639 | 0.333  | 128280000 | 946                              | 201 | 0.247  | 128280000 |
| 876                               | 110 | 0.358  | 128280000 | 871                              | 308 | 0.216  | 128280000 |
| 542                               | 700 | 0.409  | 128280000 | 427                              | 143 | 0.242  | 128280000 |
| 780                               | 437 | 0.289  | 128280000 | 270                              | 117 | 0.229  | 128280000 |
| 28                                | 918 | 0.206  | 128280000 | 527                              | 231 | 0.227  | 128280000 |
| 148                               | 798 | 0.237  | 128280000 | 421                              | 155 | 0.225  | 128280000 |
| 234                               | 882 | 0.264  | 128280000 | 817                              | 656 | 0.184  | 128280000 |
| 290                               | 424 | 0.225  | 128280000 | 704                              | 36  | 0.211  | 128280000 |
| 947                               | 316 | 0.198  | 128280000 | 611                              | 118 | 0.198  | 128280000 |
| 259                               | 153 | 0.221  | 128280000 | 350                              | 121 | 0.201  | 128280000 |
| 890                               | 890 | 0.240  | 129060000 | 677                              | 492 | 0.173  | 128280000 |
| 404                               | 106 | 0.536  | 129590000 | 98                               | 88  | 0.166  | 128280000 |
| 496                               | 323 | 0.632  | 133500000 | 706                              | 366 | 0.184  | 128280000 |
|                                   |     |        |           | 253                              | 43  | 0.166  | 128280000 |
|                                   |     |        |           | 770                              | 819 | 0.144  | 128280000 |
|                                   |     |        |           | 951                              | 352 | 0.139  | 128280000 |
|                                   |     |        |           | 41                               | 31  | 0.104  | 128280000 |
|                                   |     |        |           | 235                              | 240 | 0.175  | 129060000 |
|                                   |     |        |           | 541                              | 649 | 0.173  | 129060000 |
|                                   |     |        |           | 97                               | 968 | 0.151  | 129060000 |
|                                   |     |        |           | 959                              | 849 | 0.094  | 129060000 |
|                                   |     |        |           | 133                              | 115 | 0.173  | 129590000 |
|                                   |     |        |           | 522                              | 670 | 2.960  | 133230000 |
|                                   |     |        |           | 392                              | 528 | 0.687  | 133230000 |
|                                   |     |        |           | 431                              | 210 | 0.243  | 133230000 |
|                                   |     |        |           | 471                              | 177 | 0.315  | 133500000 |
|                                   |     |        |           | 437                              | 154 | 0.239  | 133500000 |
|                                   |     |        |           | 976                              | 51  | 0.678  | 151070000 |
|                                   |     |        |           | 464                              | 855 | 1.079  | 154970000 |

<sup>a</sup>Notes: Col(umn) and Row are defined such that (0,0) is the pixel in the upper left corner of each image. Offset is the additive offset in DN resulting from the hot pixel at the given coordinates. SCLK is the Spacecraft Clock counter time after which the pixel at those coordinates became “hot.” By MER convention, SCLK is the number of seconds since 1 January 2000 at 11:58:55 UTC.

The  $c_0$  and  $c_1$  coefficients for all four Pancams are listed in Table 6. As in our preflight model, we ignore any saturated pixels and their immediate neighbors in the same column.

[35] The final step in the active region dark modeling is to generate a “dark current rate flat image,”  $F_{(i,j)}$ , which is analogous to the masked region “dark-flat” image described above and which we expect to be constant over temperature. Unlike the masked region, however, we expect no column coherence for the dark current in the active region (column coherence in the masked region is due to the gradual transfer of charge from pixel to pixel within each column over the course of the  $\sim 5$  sec readout process). The value of  $F_{(i,j)}$  for each pixel is determined by finding the weighted mean of the dark flat values of that pixel over the images used. That is,

$$F_{(i,j)} = \frac{\sum_{\text{used images}} DN(i,j)}{\sum_{\text{used images}} DN_{\text{central box mean}}} \quad (15)$$

where the numerator is simply the sum of all the pixel values in the set of images used, and the denominator is the sum of all of the central box mean values described above.

[36] For a given pixel, the data from a particular image will not be used if the pixel is saturated in that image, or if

an adjacent pixel in the same column is saturated. Also, the data from that image will not be used if it is determined that a cosmic ray hit has affected the pixel value in that image. The effect of using the “weighted mean” of dark-rate-flat values is that the longer exposure, higher temperature images (that have higher DN values and consequently higher SNR) will have a higher weighting. An example  $F_{(i,j)}$  image for the active region dark current is shown as a 3-D plot in Figure 12. Thus the final equation for the calculation of the active region dark current for an exposure of duration  $E$  is

$$\text{active\_dark\_current}_{(i,j)} = F_{(i,j)} E c_0 \exp(c_1 T) \quad (16)$$

where  $T$  is temperature,  $c_0$  and  $c_1$  are from equation (5), and  $F_{(i,j)}$  is the dark-rate-flat value for the pixel at column  $i$ , row  $j$  calculated by equation (15) as described above.

[37] Because our model uses the same exponential coefficient  $c_1$  for all pixels (based on the average pixel), it has the potential to produce significant errors for outlier pixels that have an exponential response that is much different from the average. In such cases, the dark-rate-flat value would not be constant over temperature, but instead would be an exponential (based on the assumption that the actual dark current for each pixel is a simple exponential function). In our preflight dark current modeling approach [Bell *et al.*,

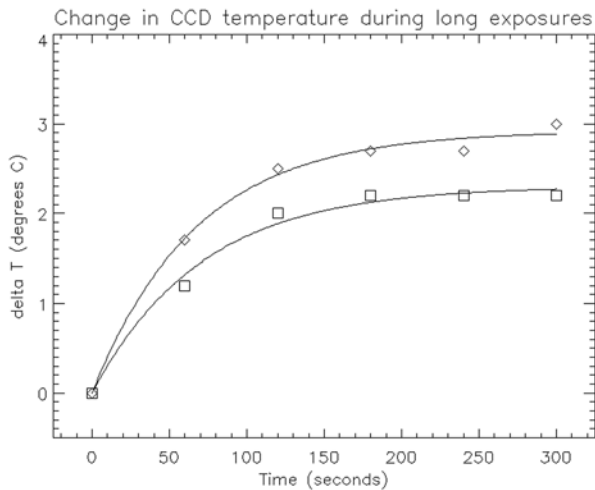


**Figure 10.** Example of typical Pancam CCD self-heating curves observed during long exposures acquired during preflight calibration in Mars-like vacuum chamber conditions. The two curves are based on temperature measurements (recorded once each minute) during 5+ minute exposure dark images. Delta T is the recorded temperature minus  $T_0$  (the temperature at the start of the exposure). The data are from preflight calibration of the Opportunity left Pancam (S/N 115). Squares are from image 020915010445\_3355392\_L8\_115.img; diamonds are from image 020915232144\_3355392\_L8\_115.img. The curves are the best fits based on equation (6).

2003], we generated  $c_0$  and  $c_1$  coefficients for each pixel. That model revealed a Gaussian distribution of coefficient values around the mean of  $c_0$  and  $c_1$ . Based on that analysis, we can calculate the expected level of uncertainty in the new in-flight dark current model that uses the  $c_1$  of the average pixel and assumes a dark-rate-flat value that is constant over temperature for each pixel. For CCD 115, for example, the  $3\sigma$  uncertainty at  $10^\circ\text{C}$  is 2.35%. This uncertainty is arrived at by assuming a pixel  $(i, j)$  for which the actual dark current accumulation rate is  $c_0 \exp(c'_1 T)$ , where  $c'_1$  is  $3\sigma$  from the  $c_1$  coefficient of the average pixel

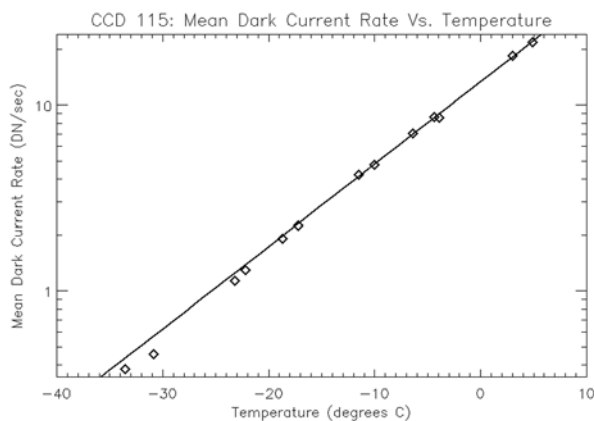


**Figure 11.** Example of data and model for the active region dark current accumulation rate for the Opportunity left Pancam (S/N 115).

from equation (5) and where  $\sigma$  itself is taken from the preflight distribution of  $c_1$  coefficients. The uncertainty is the percentage difference between the actual dark current rate that the assumed pixel has and the modeled rate using  $c_0$ ,  $c_1$  and an  $F_{(i,j)}$  of 1.0. The standard deviation of the  $c_1$  coefficient, and hence the uncertainty in dark current calculation for the outlier pixels, varies significantly between CCDs and is summarized in Table 9 (based on measurements of coefficients of individual pixels from preflight calibration data). The most important result from this analysis is that even at the (rare) warmest CCD temperatures encountered in flight, the active region dark model coefficients have uncertainties at the  $3\sigma$  level usually less than 2 DN.

[38] Currently, all pixels in a given CCD are modeled using the same  $c_0$  and  $c_1$  coefficients and a dark-rate-flat value ( $F_{(i,j)}$ ) that is constant over temperature. A future refinement of the Pancam dark current model will be to separately model the  $\sim 1000$  outlier pixels per CCD with  $c_1$  coefficients  $>3\sigma$  from the mean value and for which we can attain sufficient accuracy. This will allow us to better model the dark current in the outlier pixels while still maintaining most of the flexibility and simplicity of the fixed dark-rate-flat model. However, the reason that we abandoned our original attempt to model the  $c_0$  and  $c_1$  coefficients individually for all pixels was the lack of sufficient preflight and in-flight data to make an accurate model. The data that we currently have is sufficient for improving the modeling of some of these outlier pixels. For others, the data are too noisy to improve upon the current model. To fully implement such a refinement of our new in-flight dark current model may require a dedicated and extensive dark current acquisition campaign, which may not be possible given limited resources for acquisition of this kind of calibration data on Mars. Fortunately, the current level of accuracy of the new model appears to be adequate to continue to meet

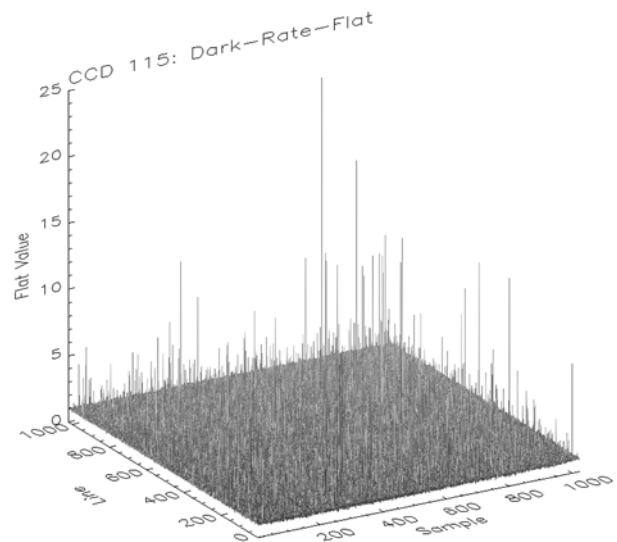


**Figure 12.** Example “dark current rate flat image” for the Opportunity left Pancam CCD (S/N 115). The vast majority of the pixels define the plane at Flat Value = 1.0. For clearer visualization, values above 25 have been capped at 25.

**Table 9.** Uncertainties in the Derived Pancam Active Region Dark Current Coefficients (Equation (5))

| Camera S/N | $c_0$ Mean | $c_0$ 1 $\sigma$ Error | $c_1$ Mean | $c_1$ 1 $\sigma$ Error | 3 $\sigma$ % Error at 10°C | 3 $\sigma$ DN/s Error at 10°C |
|------------|------------|------------------------|------------|------------------------|----------------------------|-------------------------------|
| 103        | 14.79      | 1.31                   | 0.0941     | 0.00080                | 2.38                       | 0.92                          |
| 104        | 19.25      | 1.74                   | 0.0861     | 0.00114                | 3.36                       | 1.58                          |
| 114        | 14.92      | 1.47                   | 0.0915     | 0.00205                | 5.97                       | 2.36                          |
| 115        | 15.06      | 1.33                   | 0.0880     | 0.00079                | 2.35                       | 0.87                          |

the scientific and operational requirements defined for the Pancam investigation [Bell et al., 2003].

### 2.3.3. Dark Current Variations During the Mission

[39] If the dark current is observed to change over time as the mission progresses, an adjustment can be applied to the new model by simply calculating new  $c_0$  and  $c_1$  coefficients for the central box using newly acquired data (equation (5)). If zero exposure images exist for several different temperatures, then the  $a_0$  and  $a_1$  masked region dark model parameters (equation (2)) may be similarly recalculated. It is also possible to modify the dark-flat field images based on new data, even if only a single new temperature has been sampled. However, in order to modify the dark-flat, it would be necessary to use multiple new images at multiple new temperatures which would result in a significantly higher SNR.

[40] While our analysis shows that the mean  $c_0$  and  $c_1$  coefficients appear to have remained stable during the mission so far ( $\sim$ sol 400 on both rovers), we have observed some sudden jumps in the dark-rate-flat values of individual pixels over time. These jumps appear to occur at specific points in time and may be related to the appearance of the new hot pixels discussed above. The extent of this effect should lead to a noticeable increase in the mean  $c_0$  coefficient over time, but because we exclude values that are  $>3\sigma$  from the mean, such changes are not large enough to influence our dark model calculations.

[41] These increases in dark current rate for individual pixels are assumed to be the result of radiation damage or some other aging effect in the electronics or detectors. We have measured the effect by counting the number of pixels that have shown a measurable dark current rate increase over the life of the instruments on Mars. The result is a Poisson-like distribution of slightly higher dark current

accumulation rates with time as shown in Figure 13. The increase factor is defined as the ratio of  $F_{(i,j)}$  postjump to  $F_{(i,j)}$  prejump.

[42] The fact that these jumps are observed to occur at specific points in time has allowed us to model the pixels that have changed their dark-rate-flat value over the course of the mission. We have identified  $\sim 4000$  pixels in each camera that have undergone a jump in dark-rate-flat value that is above the noise threshold that we are able to detect. Measured jumps range from a factor of 1.05 to 321, with a median near a factor of 2. The detections are made by calculating the dark-rate-flat value for each pixel in each dedicated dark image. A pixel is determined to have jumped if the following two conditions are met: (1) all of the measured values prior to some point in time are less than all the measured values after that point in time and (2) the upper 1 $\sigma$  dark-rate-flat value of the prejump measurements is less than the lower 1 $\sigma$  dark-rate-flat value of postjump measurements. These pixels are stored in a table that indicates the SCLK times when the jump was detected and the new dark-rate-flat value for that pixel, which is used to adjust the dark-rate-flat image after the given mission time. By modifying  $F_{(i,j)}$  to model the observed jumps in dark accumulation rate, we are assuming that these jumps are changes to the linear coefficient ( $c_0$ ) in the dark current response of the pixel, but the aging events may also be affecting the exponential coefficient ( $c_1$ ). We intend to search for this possibility, but as with  $c_1$ -outlier pixels, all but very large changes to the  $c_1$  coefficient will be difficult to detect without a more extensive in-flight dark current imaging campaign.

[43] During preflight calibration activities, we searched for but could not identify any evidence of noise or bias/dark current variations induced in the Pancam images by the

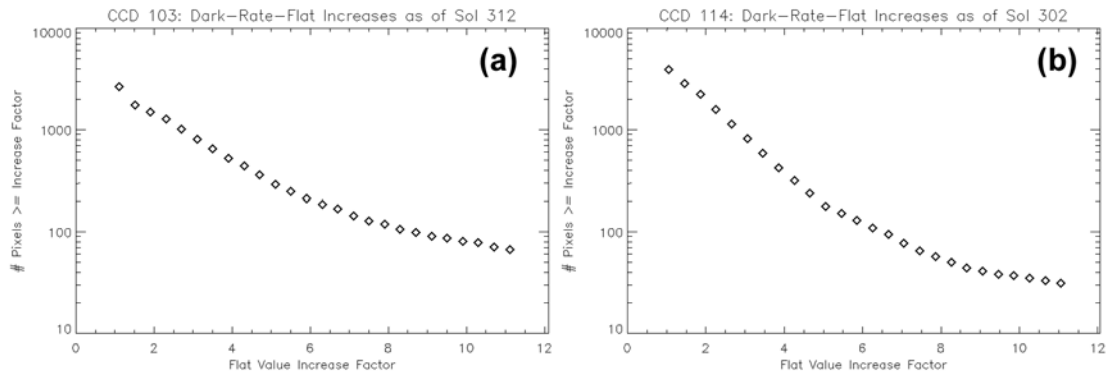


**Figure 13.** Number of potentially “damaged” pixels recorded by (a) the Spirit rover right Pancam S/N 103 as of MER-A Sol 312 and (b) the Opportunity rover right Pancam S/N 114 as of MER-B Sol 302. The ordinate shows the number of pixels on each detector (out of  $2 \times 10^6$  total) that have increased their dark current rate by the multiplicative factor indicated on the abscissa. For example, on each rover,  $\sim 1000$  pixels (0.05% of the total) appear to have increased their dark current accumulation rate by a factor of two over the course of the missions so far.

operation of other instruments/systems during imaging. As an additional test, we performed an experiment on Spirit sol 231 to see if operations by the Rock Abrasion Tool (RAT) would induce noise in Pancam images. We obtained two sets of dark current images, one during RAT operations and one immediately afterward. Analysis of these images revealed no evidence for coherent noise in the images obtained during the RAT grind, and if there is an increase in overall system noise or bias/dark current level, it is at or below the statistically significant detection level ( $\leq 0.1$  DN).

#### 2.4. “Shutter Smear” Subtraction

[44] After the image integration phase is done, the charge in the CCD is rapidly ( $\sim 5$  msec) shifted from the active region of the CCD to the masked region of the CCD. Because there is no physical shutter to block out the light as the charge is shifted row by row under the mask, those rows that are still within the active region are still accumulating signal from the scene. The additional charge that is accumulated during this shifting process is called the “shutter smear.” Due to the confined space on the camera bar, the left Pancam is rotated  $180^\circ$  relative to the right Pancam. The downlinked EDRs, however, have already been rotated so that “up” in the image (higher row number) corresponds to “gravitational up” in the scene. As a result, shutter smear effects appear to be in opposite directions in the left and right images. We refer to the direction toward the serial readout register as “down” or “downstream” in CCD space. Each row accumulates some additional charge from each downstream row until it reaches the masked region, resulting in a linear “ramp” of additional scene-dependent charge added to each image.

[45] An equivalent amount of charge is also accumulated during the flush prior to image integration as the CCD transfers charge in the opposite direction (upstream). Prior to integration, all the charge is transferred upstream and off the “top” of the CCD. As each row is shifted off the top, the bottom row has zeros shifted into it. As the zero-charge rows are shifted into the active region, though, they begin to accumulate charge. When the flush is done, all rows of the CCD have only the charge they have accumulated since they began shifting through the active region.

[46] A particular row will shift through exactly the same rows (and for the same amount of time) on its way upstream prior to integration as it shifts through downstream once integration is complete. Hence, if the illumination in the scene does not change over the duration of the exposure, the shutter smear component prior to integration as the buffer is flushed will be the same as the shutter smear component after the integration as the charge is transferred to the masked region. As a result, if correction for this effect is not performed by the onboard software, and the shutter smear needs to be calculated analytically, it is sufficient to perform the calculation for one of those transfers and simply double the result.

[47] In order to analytically remove the shutter smear for a given row, it is necessary to know the component of the signal that results from light from the scene for all of the downstream rows. As a result, analytical shutter smear removal can only be done on full-frame (either full resolution or down-sampled) images or subframed images that start at row 1 in CCD space. The algorithm we use to

calculate the shutter smear for a given row is recursive and uses the following equations:

$$scene(n) = signal(n) - smear(n) \quad (17)$$

$$smear(n) = 2 \sum_{i=1}^{n-1} (scene(i)/exposure) \cdot 5 \mu\text{sec} \quad (18)$$

$$smear(1) = 0 \quad (19)$$

where *signal* is the observed DN values from the raw data files, *smear* is the shutter smear component of *signal*, and *scene* is the shutter smear corrected DN value. The shutter smear is calculated and removed on a row-by-row basis, starting at row  $n = 1$  and progressing upstream through row  $n = 1024$ .

[48] Uncertainties in the analytical shutter smear removal algorithm can arise from cosmic ray hits, saturated pixels, imperfect removal of bias and dark current, brightness values in the scene changing over the duration of the exposure, or pixel averaging (downsampling). Cosmic ray hits can alter the DN value of one or more pixels in an unpredictable way. Saturation of one or more pixels will result in the “true” DN values of those pixels being an unknown amount higher than recorded in the image. Neighboring pixels in the same column could also be affected (and therefore their true values unknown) if there is blooming as a result of the saturation. In both of these cases, the value of *scene* for any pixels upstream of the affected pixels cannot be calculated precisely. These effects will typically be obvious but localized in problematic images. For example, the bright trail upstream of a saturated pixel is often not completely removed during analytic shutter smear correction because the effect of that pixel on the shutter smear has been underestimated. A cosmic-ray hit may leave a slight dark trail behind it in a calibrated image because the effect of that pixel on the shutter smear has been overestimated.

[49] Some of the sources of uncertainty associated with analytic shutter smear removal can affect the entire calibrated image. For example, there is uncertainty in the models for bias and dark current, and as a result, when those are subtracted out of the raw image, there will be an uncertainty in the resulting estimate of *scene*. The relative magnitude of this uncertainty will depend upon the temperature and exposure duration. For images taken at colder temperatures, the effect of dark current will be much smaller. As exposure time decreases, the relative value of masked-region dark current to *scene* will increase, whereas the relative value of active region dark current to *scene* should remain the same. As another example, for longer exposures near sunrise or sunset, it is possible that a brightening or darkening sky over the course of the exposure will cause the algorithm to overestimate or underestimate *smear*. However, our experience indicates that this is an extremely minor effect for such small monotonic variations of brightness expected over several seconds. In a few cases, such as for small rapidly varying Sun glints off metallic spacecraft surfaces, shutter smear artifacts cannot be properly removed using either this calibration approach or the onboard shutter smear removal method. Finally, the effect of pixel downsampling could introduce a small level



**Table 10.** Spirit/Pancam In-Flight Flatfield Images of the Martian Sky

| Filename                        | S/N | Sol | LTST  | $\lambda$ ,<br>$\mu\text{m}$ | Temperatures, °C |          |          | Exp., ms | Camera     |            | Sun        |            | Note |
|---------------------------------|-----|-----|-------|------------------------------|------------------|----------|----------|----------|------------|------------|------------|------------|------|
|                                 |     |     |       |                              | L<br>Elec        | L<br>CCD | R<br>CCD |          | az,<br>deg | el,<br>deg | az,<br>deg | el,<br>deg |      |
| 2P127268212EFF0224P2701R2M1.IMG | 103 | 10  | 16:06 | 754                          | -12.33           | -10.12   | -10.86   | 399.36   | 0.00       | 45.00      | 265.42     | 30.13      |      |
| 2P137032451EFF4100P2880R1M1.IMG | 103 | 120 | 16:20 | 436                          | -17.73           | -22.11   | -22.43   | 9241.60  | 109.94     | 18.06      | 288.92     | 20.13      | a    |
| 2P137032481EFF4100P2880R2M1.IMG | 103 | 120 | 16:21 | 754                          | -17.15           | -22.45   | -22.14   | 552.96   | 109.94     | 18.06      | 288.88     | 20.02      | a    |
| 2P137032503EFF4100P2880R3M1.IMG | 103 | 120 | 16:21 | 803                          | -16.78           | -22.58   | -22.18   | 901.12   | 109.94     | 18.06      | 288.84     | 19.94      | a    |
| 2P137032525EFF4100P2880R4M1.IMG | 103 | 120 | 16:22 | 864                          | -16.44           | -22.72   | -22.18   | 1679.36  | 109.94     | 18.06      | 288.81     | 19.86      | a    |
| 2P137032548EFF4100P2880R5M1.IMG | 103 | 120 | 16:22 | 904                          | -16.11           | -22.83   | -22.16   | 1259.52  | 109.94     | 18.06      | 288.78     | 19.77      | a    |
| 2P137032571EFF4100P2880R6M1.IMG | 103 | 120 | 16:22 | 934                          | -15.79           | -22.92   | -22.18   | 1797.12  | 109.94     | 18.06      | 288.74     | 19.69      | a    |
| 2P137032594EFF4100P2880R7M1.IMG | 103 | 120 | 16:23 | 1009                         | -15.49           | -23.03   | -22.16   | 2216.96  | 109.94     | 18.06      | 288.71     | 19.60      | a    |
| 2P151219172EFF8982P2884R1M1.IMG | 103 | 280 | 12:16 | 436                          | -27.10           | -29.44   | -29.38   | 15595.50 | 179.51     | 34.88      | 354.12     | 50.43      |      |
| 2P151219209EFF8982P2884R2M1.IMG | 103 | 280 | 12:17 | 754                          | -26.26           | -29.69   | -29.00   | 1018.88  | 179.51     | 34.88      | 353.91     | 50.41      |      |
| 2P151219231EFF8982P2884R3M1.IMG | 103 | 280 | 12:17 | 803                          | -25.88           | -29.80   | -29.07   | 1607.68  | 179.51     | 34.88      | 353.78     | 50.40      |      |
| 2P151219254EFF8982P2884R4M1.IMG | 103 | 280 | 12:17 | 864                          | -25.43           | -29.84   | -29.00   | 2995.20  | 179.51     | 34.88      | 353.65     | 50.39      |      |
| 2P151219278EFF8982P2884R5M1.IMG | 103 | 280 | 12:18 | 904                          | -24.98           | -29.87   | -28.98   | 2247.68  | 179.51     | 34.88      | 353.51     | 50.38      |      |
| 2P151219301EFF8982P2884R6M1.IMG | 103 | 280 | 12:18 | 934                          | -24.60           | -29.91   | -28.89   | 3210.24  | 179.51     | 34.88      | 353.38     | 50.37      |      |
| 2P151219326EFF8982P2884R7M1.IMG | 103 | 280 | 12:18 | 1009                         | -24.17           | -29.91   | -28.85   | 3957.76  | 179.51     | 34.88      | 353.24     | 50.36      |      |
| 2P159835126EFAA2HPP2886R1M1.IMG | 103 | 377 | 13:46 | 436                          | 1.62             | -4.97    | -6.39    | 7736.32  | 120.95     | 35.20      | 314.78     | 52.08      |      |
| 2P159835155EFAA2HPP2886R2M1.IMG | 103 | 377 | 13:46 | 754                          | 2.10             | -5.24    | -6.05    | 302.08   | 120.95     | 35.20      | 314.65     | 52.00      |      |
| 2P159835177EFAA2HPP2886R3M1.IMG | 103 | 377 | 13:47 | 803                          | 2.37             | -5.37    | -6.03    | 486.40   | 120.95     | 35.20      | 314.55     | 51.94      |      |
| 2P159835199EFAA2HPP2886R4M1.IMG | 103 | 377 | 13:47 | 864                          | 2.65             | -5.46    | -5.98    | 901.12   | 120.95     | 35.20      | 314.45     | 51.88      |      |
| 2P159835222EFAA2HPP2886R5M1.IMG | 103 | 377 | 13:47 | 904                          | 2.92             | -5.56    | -5.98    | 675.84   | 120.95     | 35.20      | 314.35     | 51.81      |      |
| 2P159835245EFAA2HPP2886R6M1.IMG | 103 | 377 | 13:48 | 934                          | 3.17             | -5.60    | -5.98    | 967.68   | 120.95     | 35.20      | 314.24     | 51.75      |      |
| 2P159835268EFAA2HPP2886R7M1.IMG | 103 | 377 | 13:48 | 1009                         | 3.42             | -5.69    | -5.98    | 1192.96  | 120.95     | 35.20      | 314.14     | 51.68      |      |
| 2P127268212EFF0224P2701L2M1.IMG | 104 | 10  | 16:06 | 753                          | -12.33           | -10.12   | -10.86   | 394.24   | 0.00       | 45.00      | 265.41     | 30.11      |      |
| 2P137032404EFF4100P2880L1M1.IMG | 104 | 120 | 16:20 | 739                          | -19.00           | -21.41   | -23.10   | 35.84    | 107.84     | 17.93      | 288.99     | 20.31      | a    |
| 2P137032251EFF4100P2880L2M1.IMG | 104 | 120 | 16:17 | 753                          | -23.54           | -22.27   | -22.68   | 547.84   | 107.84     | 17.93      | 289.22     | 20.87      | a    |
| 2P137032273EFF4100P2880L3M1.IMG | 104 | 120 | 16:17 | 673                          | -23.13           | -21.93   | -22.75   | 829.44   | 107.84     | 17.93      | 289.19     | 20.79      | a    |
| 2P137032295EFF4100P2880L4M1.IMG | 104 | 120 | 16:18 | 601                          | -22.48           | -21.80   | -22.79   | 885.76   | 107.84     | 17.93      | 289.16     | 20.71      | a    |
| 2P137032317EFF4100P2880L5M1.IMG | 104 | 120 | 16:18 | 535                          | -21.78           | -21.68   | -22.86   | 1935.36  | 107.84     | 17.93      | 289.12     | 20.63      | a    |
| 2P137032340EFF4100P2880L6M1.IMG | 104 | 120 | 16:19 | 482                          | -21.03           | -21.59   | -22.93   | 2600.96  | 107.84     | 17.93      | 289.09     | 20.54      | a    |
| 2P137032364EFF4100P2880L7M1.IMG | 104 | 120 | 16:19 | 432                          | -20.26           | -21.55   | -22.99   | 9287.68  | 107.84     | 17.93      | 289.05     | 20.46      | a    |
| 2P151219120EFF8982P2884L1M1.IMG | 104 | 280 | 12:15 | 739                          | -28.72           | -28.68   | -30.41   | 61.44    | 177.09     | 35.10      | 354.43     | 50.45      |      |
| 2P151218930EFF8982P2884L2M1.IMG | 104 | 280 | 12:12 | 753                          | -35.70           | -30.38   | -30.37   | 998.40   | 177.09     | 35.10      | 355.52     | 50.51      |      |
| 2P151218951EFF8982P2884L3M1.IMG | 104 | 280 | 12:12 | 673                          | -35.12           | -29.89   | -30.32   | 1530.88  | 177.09     | 35.10      | 355.40     | 50.51      |      |
| 2P151218974EFF8982P2884L4M1.IMG | 104 | 280 | 12:13 | 601                          | -34.34           | -29.66   | -30.30   | 1628.16  | 177.09     | 35.10      | 355.26     | 50.50      |      |
| 2P151218997EFF8982P2884L5M1.IMG | 104 | 280 | 12:13 | 535                          | -33.39           | -29.44   | -30.26   | 3568.64  | 177.09     | 35.10      | 355.13     | 50.49      |      |
| 2P151219022EFF8982P2884L6M1.IMG | 104 | 280 | 12:14 | 482                          | -32.43           | -29.28   | -30.32   | 4787.20  | 177.09     | 35.10      | 354.99     | 50.48      |      |
| 2P151219075EFF8982P2884L7M1.IMG | 104 | 280 | 12:14 | 432                          | -30.38           | -28.57   | -30.37   | 13071.40 | 177.09     | 35.10      | 354.68     | 50.47      |      |
| 2P159835079EFAA2HPP2886L1M1.IMG | 104 | 377 | 13:45 | 739                          | 0.55             | -4.40    | -7.07    | 15.36    | 118.55     | 34.80      | 315.00     | 52.21      |      |
| 2P159834889EFAA2HPP2886L2M1.IMG | 104 | 377 | 13:42 | 753                          | -4.36            | -5.51    | -6.93    | 302.08   | 118.55     | 34.80      | 315.89     | 52.73      |      |
| 2P159834911EFAA2HPP2886L3M1.IMG | 104 | 377 | 13:42 | 673                          | -4.04            | -5.17    | -6.93    | 455.68   | 118.55     | 34.80      | 315.78     | 52.67      |      |
| 2P159834933EFAA2HPP2886L4M1.IMG | 104 | 377 | 13:43 | 601                          | -3.48            | -4.95    | -6.96    | 481.28   | 118.55     | 34.80      | 315.68     | 52.61      |      |
| 2P159834955EFAA2HPP2886L5M1.IMG | 104 | 377 | 13:43 | 535                          | -2.86            | -4.85    | -6.96    | 1059.84  | 118.55     | 34.80      | 315.58     | 52.55      |      |
| 2P159834990EFAA2HPP2886L6M1.IMG | 104 | 377 | 13:43 | 482                          | -1.86            | -4.65    | -6.98    | 1848.32  | 118.55     | 34.80      | 315.41     | 52.46      |      |
| 2P159835029EFAA2HPP2886L7M1.IMG | 104 | 377 | 13:44 | 432                          | -0.79            | -4.36    | -7.02    | 6589.44  | 118.55     | 34.80      | 315.23     | 52.35      |      |

Notes: a, used to generate final in-flight flatfield file.

of uncertainty in the analytic smear correction process because smear effects of groups of pixels are all averaged together. We have not been able to detect any calibration problems associated with this effect, however.

[50] Regardless of what effects are causing uncertainty in the correction, those effects will be magnified when calculating the correction for very short exposures, as the ratio of *smear* to *signal* becomes large. And of course, as exposure time increases, the ratio of *smear* to *signal* becomes increasingly small, to the point where onboard or analytic shutter smear correction is usually ignored for exposure times longer than about 700 msec in Pancam flight images. For both rovers, ~60% of Pancam images undergo onboard “automatic” shutter smear correction and ~30% more undergo the analytic shutter smear correction later as part of the in-flight calibration pipeline. The remaining 10% of the images are subframed scenes for which onboard shutter smear correction was not performed and for which an analytic correction cannot be performed because the required

range of CCD rows is not available as part of the subframe. Most of these latter kinds of images were acquired primarily for morphologic analyses, and so obtaining the highest-fidelity radiometric calibration is not particularly critical.

## 2.5. Correction of Pixel-to-Pixel Responsivity (Flatfield) Variations

### 2.5.1. Observations

[51] During preflight calibration activities, normalized flatfield files (mean value = 1.0) were generated for each possible filter/CCD combination [Bell et al., 2003, 2004a], except for the neutral density 5 solar filters L8 and R8, which could not be adequately illuminated to obtain flatfield images. These initial preflight flatfield images proved adequate to remove many of the pixel-to-pixel responsivity variations from raw Pancam flight data. However, because of limitations in the preflight calibration setup, some of these initial flatfield images were ultimately found to yield unacceptable levels of residual high-frequency flatfield

**Table 11.** Opportunity/Pancam In-Flight Flatfield Images of the Martian Sky

| Filename                        | S/N | Sol | LTST  | $\lambda$ ,<br>nm | Temperatures (°C) |          |          | Exp.,<br>ms | Camera     |            | Sun        |            | Note |
|---------------------------------|-----|-----|-------|-------------------|-------------------|----------|----------|-------------|------------|------------|------------|------------|------|
|                                 |     |     |       |                   | L<br>Elec         | L<br>CCD | R<br>CCD |             | az,<br>deg | el,<br>deg | az,<br>deg | el,<br>deg |      |
| 1P128551144EFF0205P2701R1M1.IMG | 114 | 4   | 14:52 | 436               | 25.02             | 3.21     | 1.09     | 5703.68     | 0.00       | 45.00      | 260.39     | 46.55      | a    |
| 1P128551095EFF0205P2701R2M1.IMG | 114 | 4   | 14:52 | 754               | 25.04             | 3.23     | 0.87     | 373.76      | 0.00       | 45.00      | 260.36     | 46.74      | a    |
| 1P128551190EFF0205P2701R3M1.IMG | 114 | 4   | 14:53 | 803               | 25.00             | 3.21     | 1.23     | 527.36      | 0.00       | 45.00      | 260.42     | 46.36      | a    |
| 1P128551237EFF0205P2701R4M1.IMG | 114 | 4   | 14:54 | 864               | 25.02             | 3.19     | 1.39     | 916.48      | 0.00       | 45.00      | 260.44     | 46.17      | a    |
| 1P128551279EFF0205P2701R5M1.IMG | 114 | 4   | 14:55 | 904               | 25.02             | 3.25     | 1.46     | 624.64      | 0.00       | 45.00      | 260.47     | 46.00      | a    |
| 1P128551322EFF0205P2701R6M1.IMG | 114 | 4   | 14:55 | 934               | 25.04             | 3.14     | 1.68     | 936.96      | 0.00       | 45.00      | 260.49     | 45.83      | a    |
| 1P128551361EFF0205P2701R7M1.IMG | 114 | 4   | 14:56 | 1009              | 25.04             | 3.14     | 1.73     | 1146.88     | 0.00       | 45.00      | 260.51     | 45.68      | a    |
| 1P136544216EFF1900P2860R1M1.IMG | 114 | 94  | 16:15 | 436               | -21.29            | -21.80   | -19.72   | 7096.32     | 103.92     | 18.00      | 283.06     | 25.16      |      |
| 1P136544245EFF1900P2860R2M1.IMG | 114 | 94  | 16:16 | 754               | -20.50            | -22.04   | -19.34   | 537.60      | 103.92     | 18.00      | 283.04     | 25.05      |      |
| 1P136632882EFF2000P2861R3M1.IMG | 114 | 95  | 16:14 | 803               | -18.46            | -21.06   | -20.98   | 834.56      | 104.27     | 18.04      | 283.31     | 25.48      |      |
| 1P136632903EFF2000P2861R4M1.IMG | 114 | 95  | 16:14 | 864               | -17.85            | -21.37   | -20.46   | 1510.40     | 104.27     | 18.04      | 283.30     | 25.40      |      |
| 1P136632926EFF2000P2861R5M1.IMG | 114 | 95  | 16:14 | 904               | -17.29            | -21.55   | -20.17   | 1131.52     | 104.27     | 18.04      | 283.28     | 25.31      |      |
| 1P136632948EFF2000P2861R6M1.IMG | 114 | 95  | 16:15 | 934               | -16.81            | -21.66   | -20.01   | 1617.92     | 104.27     | 18.04      | 283.27     | 25.22      |      |
| 1P136632971EFF2000P2861R7M1.IMG | 114 | 95  | 16:15 | 1009              | -16.36            | -21.73   | -19.88   | 1996.80     | 104.27     | 18.04      | 283.26     | 25.13      |      |
| 1P157578341ETH40B0P2864R1M1.IMG | 114 | 331 | 15:34 | 436               | 0.39              | -16.96   | -18.62   | 8811.52     | 116.15     | 30.03      | 292.19     | 33.71      | b    |
| 1P157578371ETH40B0P2864R2M1.IMG | 114 | 331 | 15:35 | 754               | 0.50              | -17.23   | -18.21   | 440.32      | 116.15     | 30.03      | 292.16     | 33.59      | b    |
| 1P157578392ETH40B0P2864R3M1.IMG | 114 | 331 | 15:35 | 803               | 0.54              | -17.34   | -18.15   | 670.72      | 116.15     | 30.03      | 292.13     | 33.52      | b    |
| 1P157578414ETH40B0P2864R4M1.IMG | 114 | 331 | 15:36 | 864               | 0.59              | -17.39   | -18.10   | 1249.28     | 116.15     | 30.03      | 292.11     | 33.43      | b    |
| 1P157578436ETH40B0P2864R5M1.IMG | 114 | 331 | 15:36 | 904               | 0.64              | -17.45   | -18.03   | 936.96      | 116.15     | 30.03      | 292.08     | 33.35      | b    |
| 1P157578458ETH40B0P2864R6M1.IMG | 114 | 331 | 15:36 | 934               | 0.68              | -17.50   | -17.97   | 1336.32     | 116.15     | 30.03      | 292.06     | 33.27      | b    |
| 1P157578496ETH40B0P2864R7M1.IMG | 114 | 331 | 15:37 | 1009              | 0.73              | -17.57   | -18.26   | 1648.64     | 116.15     | 30.03      | 292.02     | 33.12      | b    |
| 1P159535525EFF40EEP2867R1M1.IMG | 114 | 353 | 16:45 | 436               | -12.69            | -20.39   | -21.54   | 13035.50    | 105.21     | 35.01      | 284.57     | 17.64      |      |
| 1P159535559EFF40EEP2867R2M1.IMG | 114 | 353 | 16:46 | 754               | -12.15            | -20.70   | -21.20   | 860.16      | 105.21     | 35.01      | 284.55     | 17.50      |      |
| 1P159535581EFF40EEP2867R3M1.IMG | 114 | 353 | 16:46 | 803               | -11.83            | -20.84   | -21.27   | 1331.20     | 105.21     | 35.01      | 284.54     | 17.41      |      |
| 1P159535603EFF40EEP2867R4M1.IMG | 114 | 353 | 16:46 | 864               | -11.56            | -20.95   | -21.25   | 2478.08     | 105.21     | 35.01      | 284.53     | 17.33      |      |
| 1P159535626EFF40EEP2867R5M1.IMG | 114 | 353 | 16:47 | 904               | -11.27            | -21.06   | -21.20   | 1858.56     | 105.21     | 35.01      | 284.52     | 17.24      |      |
| 1P159535649EFF40EEP2867R6M1.IMG | 114 | 353 | 16:47 | 934               | -11.00            | -21.13   | -21.22   | 2657.28     | 105.21     | 35.01      | 284.51     | 17.15      |      |
| 1P159535673EFF40EEP2867R7M1.IMG | 114 | 353 | 16:47 | 1009              | -10.75            | -21.24   | -21.22   | 3276.80     | 105.21     | 35.01      | 284.50     | 17.05      |      |
| 1P128551144EFF0205P2701L1M1.IMG | 115 | 4   | 14:52 | 739               | 25.02             | 3.21     | 1.09     | 20.48       | 0.00       | 45.00      | 260.39     | 46.55      | a    |
| 1P128551095EFF0205P2701L2M1.IMG | 115 | 4   | 14:52 | 753               | 25.04             | 3.23     | 0.87     | 389.12      | 0.00       | 45.00      | 260.36     | 46.74      | a    |
| 1P128551190EFF0205P2701L3M1.IMG | 115 | 4   | 14:53 | 673               | 25.00             | 3.21     | 1.23     | 619.52      | 0.00       | 45.00      | 260.42     | 46.36      | a    |
| 1P128551237EFF0205P2701L4M1.IMG | 115 | 4   | 14:54 | 601               | 25.02             | 3.19     | 1.39     | 578.56      | 0.00       | 45.00      | 260.44     | 46.17      | a    |
| 1P128551279EFF0205P2701L5M1.IMG | 115 | 4   | 14:55 | 535               | 25.02             | 3.25     | 1.46     | 1361.92     | 0.00       | 45.00      | 260.47     | 46.00      | a    |
| 1P128551322EFF0205P2701L6M1.IMG | 115 | 4   | 14:55 | 482               | 25.04             | 3.14     | 1.68     | 1879.04     | 0.00       | 45.00      | 260.49     | 45.83      | a    |
| 1P128551361EFF0205P2701L7M1.IMG | 115 | 4   | 14:56 | 432               | 25.04             | 3.14     | 1.73     | 6824.96     | 0.00       | 45.00      | 260.51     | 45.68      | a    |
| 1P136544121EFF1900P2860L2M1.IMG | 115 | 94  | 16:14 | 753               | -24.28            | -22.34   | -20.48   | 532.48      | 101.82     | 18.00      | 283.11     | 25.54      |      |
| 1P136544163EFF1900P2860L7M1.IMG | 115 | 94  | 16:14 | 432               | -23.25            | -21.46   | -20.50   | 7772.16     | 101.82     | 18.00      | 283.09     | 25.38      |      |
| 1P136632852EFF2000P2861L1M1.IMG | 115 | 95  | 16:13 | 739               | -19.40            | -20.90   | -20.98   | 35.84       | 102.17     | 17.96      | 283.33     | 25.60      |      |
| 1P136632751EFF2000P2861L3M1.IMG | 115 | 95  | 16:12 | 673               | -22.46            | -21.75   | -20.75   | 824.32      | 102.17     | 17.96      | 283.39     | 26.00      |      |
| 1P136632772EFF2000P2861L4M1.IMG | 115 | 95  | 16:12 | 601               | -22.03            | -21.40   | -20.80   | 890.88      | 102.17     | 17.96      | 283.37     | 25.91      |      |
| 1P136632794EFF2000P2861L5M1.IMG | 115 | 95  | 16:12 | 535               | -21.38            | -21.19   | -20.86   | 1945.60     | 102.17     | 17.96      | 283.36     | 25.83      |      |
| 1P136632817EFF2000P2861L6M1.IMG | 115 | 95  | 16:13 | 482               | -20.62            | -21.06   | -20.89   | 2616.32     | 102.17     | 17.96      | 283.35     | 25.74      |      |
| 1P157578292ETH40B0P2864L1M1.IMG | 115 | 331 | 15:34 | 739               | -0.14             | -16.33   | -19.52   | 25.60       | 113.84     | 30.02      | 292.25     | 33.89      | b    |
| 1P157578122ETH40B0P2864L2M1.IMG | 115 | 331 | 15:31 | 753               | -2.11             | -17.27   | -19.22   | 435.20      | 113.84     | 30.02      | 292.45     | 34.53      | b    |
| 1P157578143ETH40B0P2864L3M1.IMG | 115 | 331 | 15:31 | 673               | -1.97             | -17.01   | -19.29   | 660.48      | 113.84     | 30.02      | 292.43     | 34.45      | b    |
| 1P157578165ETH40B0P2864L4M1.IMG | 115 | 331 | 15:32 | 601               | -1.70             | -16.89   | -19.34   | 706.56      | 113.84     | 30.02      | 292.40     | 34.37      | b    |
| 1P157578187ETH40B0P2864L5M1.IMG | 115 | 331 | 15:32 | 535               | -1.45             | -16.78   | -19.38   | 1541.12     | 113.84     | 30.02      | 292.38     | 34.28      | b    |
| 1P157578210ETH40B0P2864L6M1.IMG | 115 | 331 | 15:32 | 482               | -1.16             | -16.71   | -19.40   | 2068.48     | 113.84     | 30.02      | 292.35     | 34.20      | b    |
| 1P157578250ETH40B0P2864L7M1.IMG | 115 | 331 | 15:33 | 432               | -0.66             | -16.33   | -19.45   | 10168.30    | 113.84     | 30.02      | 292.30     | 34.05      | b    |
| 1P159535465EFF40EEP2867L1M1.IMG | 115 | 353 | 16:44 | 739               | -14.11            | -19.56   | -22.55   | 51.20       | 102.77     | 34.98      | 284.59     | 17.87      |      |
| 1P159535302EFF40EEP2867L2M1.IMG | 115 | 353 | 16:41 | 753               | -18.57            | -20.48   | -22.10   | 839.68      | 102.77     | 34.98      | 284.67     | 18.51      |      |
| 1P159535324EFF40EEP2867L3M1.IMG | 115 | 353 | 16:42 | 673               | -18.23            | -20.14   | -22.16   | 1290.24     | 102.77     | 34.98      | 284.66     | 18.43      |      |
| 1P159535348EFF40EEP2867L4M1.IMG | 115 | 353 | 16:42 | 601               | -17.60            | -20.05   | -22.21   | 1377.28     | 102.77     | 34.98      | 284.65     | 18.33      |      |
| 1P159535370EFF40EEP2867L5M1.IMG | 115 | 353 | 16:42 | 535               | -16.93            | -19.90   | -22.28   | 3010.56     | 102.77     | 34.98      | 284.64     | 18.24      |      |
| 1P159535394EFF40EEP2867L6M1.IMG | 115 | 353 | 16:43 | 482               | -16.18            | -19.78   | -22.34   | 4044.80     | 102.77     | 34.98      | 284.63     | 18.15      |      |
| 1P159535419EFF40EEP2867L7M1.IMG | 115 | 353 | 16:43 | 432               | -15.46            | -19.69   | -22.41   | 14448.60    | 102.77     | 34.98      | 284.62     | 18.05      |      |

Notes: a, used to generate final in-flight flatfield file; b, only “thumbnail” versions of these images exist because the full resolution files were accidentally deleted from the rover prior to downlink.

artifacts once implemented in the flight calibration pipeline. For those cases, new flatfield images had to be synthesized or approximated from the available preflight data. These limitations, plus the general desire to obtain as much calibration data as possible in a flight-like configuration, compelled us to acquire new in-flight Pancam flatfield data using images of the Martian sky.

[52] During flight operations, several sets of losslessly compressed images of the sky were taken through all 14 nonsolar filter positions on both Spirit (Table 10) and Opportunity (Table 11) with the intent to use these images to validate, augment, or, if possible, replace the flatfields created with preflight data. Early in the mission, these so-called “sky flat” images were acquired with the Pancams on

**Table 12.** Pancam In-Flight Flatfield Planar Fit Parameters

| Filename <sup>d</sup>           | Plane Fit Parameters (a + bx + cy + dxy) |            |            |            | X <sup>a</sup> , % | Y <sup>a</sup> , % |
|---------------------------------|--|------------|------------|------------|--------------------|--------------------|
|                                 | a  | b          | c          | d          |                    |                    |
| Spirit                          |  |            |            |            |                    |                    |
| 2P137032404EFF4100P2880L1M1.IMG | 0.711                                    | −2.804E-05 | 6.256E-04  | −4.060E-08 | 5.0                | 61.9               |
| 2P137032251EFF4100P2880L2M1.IMG | 0.716                                    | −2.561E-05 | 6.158E-04  | −4.758E-08 | 5.1                | 60.6               |
| 2P137032273EFF4100P2880L3M1.IMG | 0.734                                    | −4.926E-05 | 5.839E-04  | −8.687E-09 | 5.5                | 59.3               |
| 2P137032295EFF4100P2880L4M1.IMG | 0.732                                    | −4.033E-05 | 5.856E-04  | −2.044E-08 | 5.2                | 58.9               |
| 2P137032317EFF4100P2880L5M1.IMG | 0.736                                    | −3.094E-05 | 5.667E-04  | −1.885E-08 | 4.2                | 57.0               |
| 2P137032340EFF4100P2880L6M1.IMG | 0.756                                    | −5.268E-05 | 5.632E-04  | −4.776E-08 | 7.9                | 55.2               |
| 2P137032364EFF4100P2880L7M1.IMG | 0.751                                    | −6.660E-05 | 5.915E-04  | −5.590E-08 | 9.8                | 57.6               |
| 2P137032451EFF4100P2880R1M1.IMG | 0.770                                    | −4.619E-05 | 5.207E-04  | −3.046E-08 | 6.3                | 51.7               |
| 2P137032481EFF4100P2880R2M1.IMG | 0.733                                    | −3.611E-05 | 5.893E-04  | −4.039E-08 | 5.8                | 58.2               |
| 2P137032503EFF4100P2880R3M1.IMG | 0.704                                    | −3.708E-05 | 6.623E-04  | −7.037E-08 | 7.5                | 64.1               |
| 2P137032525EFF4100P2880R4M1.IMG | 0.686                                    | −2.419E-05 | 6.716E-04  | −4.101E-08 | 4.6                | 66.6               |
| 2P137032548EFF4100P2880R5M1.IMG | 0.738                                    | −3.184E-05 | 5.697E-04  | −3.228E-08 | 5.0                | 56.6               |
| 2P137032571EFF4100P2880R6M1.IMG | 0.717                                    | −3.090E-05 | 6.144E-04  | −3.970E-08 | 5.2                | 60.8               |
| 2P137032594EFF4100P2880R7M1.IMG | 0.732                                    | −3.104E-05 | 5.888E-04  | −4.642E-08 | 5.6                | 57.9               |
| Opportunity                     |  |            |            |            |                    |                    |
| 1P128551144EFF0205P2701L1M1.IMG | 1.055                                    | −1.968E-04 | 6.251E-05  | 4.834E-08  | 17.6               | 8.9                |
| 1P128551095EFF0205P2701L2M1.IMG | 1.044                                    | −1.862E-04 | 7.464E-05  | 4.911E-08  | 16.5               | 10.2               |
| 1P128551190EFF0205P2701L3M1.IMG | 1.055                                    | −1.743E-04 | 3.966E-05  | 4.816E-08  | 15.3               | 6.6                |
| 1P128551237EFF0205P2701L4M1.IMG | 1.043                                    | −1.643E-04 | 6.003E-05  | 3.674E-08  | 14.9               | 8.1                |
| 1P128551279EFF0205P2701L5M1.IMG | 1.077                                    | −2.099E-04 | 2.803E-05  | 5.642E-08  | 18.5               | 5.8                |
| 1P128551322EFF0205P2701L6M1.IMG | 1.096                                    | −2.484E-04 | 2.813E-05  | 5.559E-08  | 22.5               | 5.8                |
| 1P128551361EFF0205P2701L7M1.IMG | 1.114                                    | −2.744E-04 | 1.967E-05  | 5.563E-08  | 25.2               | 4.9                |
| 1P128551144EFF0205P2701R1M1.IMG | 1.143                                    | −2.897E-04 | −3.263E-05 | 7.300E-08  | 25.8               | 0.5                |
| 1P128551095EFF0205P2701R2M1.IMG | 1.064                                    | −2.173E-04 | 6.353E-05  | 5.195E-08  | 19.5               | 9.2                |
| 1P128551190EFF0205P2701R3M1.IMG | 1.058                                    | −2.319E-04 | 9.196E-05  | 4.813E-08  | 21.2               | 11.9               |
| 1P128551237EFF0205P2701R4M1.IMG | 1.065                                    | −2.274E-04 | 7.054E-05  | 5.275E-08  | 20.5               | 10.0               |
| 1P128551279EFF0205P2701R5M1.IMG | 1.113                                    | −2.492E-04 | −9.730E-06 | 6.722E-08  | 22.0               | 2.5                |
| 1P128551322EFF0205P2701R6M1.IMG | 1.091                                    | −2.427E-04 | 3.117E-05  | 5.966E-08  | 21.7               | 6.3                |
| 1P128551361EFF0205P2701R7M1.IMG | 1.134                                    | −2.880E-04 | −1.525E-05 | 7.227E-08  | 25.7               | 2.2                |

<sup>a</sup>X and Y are the percentage gradients of the fit plane across the center of the CCD along the X and Y axes.

each spacecraft pointing to the North ( $0^\circ$  azimuth) and  $45^\circ$  above the horizon. At the times these images were acquired, this resulted in the cameras being pointed about  $100^\circ$  (Spirit) and  $95^\circ$  (Opportunity) away from the sun in azimuth. Later in the mission, after additional sky profile information had been obtained and analyzed from separate sky imaging sequences [Lemmon *et al.*, 2004], additional sky flat images were acquired with the cameras pointed toward a theoretically “flatter” part of the sky, closer to  $130^\circ$  to  $160^\circ$  in azimuth from the Sun.

### 2.5.2. Processing of In-Flight Sky Flat Images

[53] The first set of Opportunity sky flat images taken on Mars were used to create new in-flight flatfield images for the Opportunity Pancams. This set was chosen because of their good SNR and the likely minimal effects of any dust build up on the cameras’ outer sapphire window in these early mission images. Unfortunately, most of the similar first set of Spirit sky flat images were lost from the rover’s onboard storage memory during the sol 18 computer anomaly. Thus a set of sky images exhibiting good SNR but acquired later in the mission was used to create new in-flight flatfield images for the Spirit Pancams.

[54] The Martian sky is not uniformly flat, even near its theoretically “flattest” part [e.g., Tomasko *et al.*, 1999; Lemmon *et al.*, 2004]. There can often be a significant gradient in each of the sky images caused by the nonuniformity of the sky, but over the relatively narrow field of view of the Pancams ( $16^\circ$ ), this gradient can be modeled as a simple plane. In processing sky images to create flatfield images, this planar background was modeled and removed.

[55] Flight flatfield images for both Spirit and Opportunity were created from sky flat images through the following process: First, the sky images were shutter smear, bias, and dark current corrected using the in-flight calibration pipeline procedures described above. Second, the resulting calibrated images were normalized by dividing each image by the mean of its calibrated values, excluding the 10 rows or columns of pixels closest to each edge of the CCD. Third, a best-fit 2-dimensional planar background was fit to each normalized image (again, excluding the 10 edge pixels) and this plane was divided out of each image. Table 12 provides a summary of the planar backgrounds removed from the sky images for each filter. Next, “problematic” pixels that were not corrected through the normal calibration pipeline procedures (because of cosmic ray hits or dark current saturation in the warmer flight sky flat images) were located through three methods: (1) an automatic routine found the pixels in each image that differed from the median of that image by more than 2 standard deviations; (2) more subtle pixel-scale artifacts were identified manually by comparing the sky flat images to preflight flatfield images [Bell *et al.*, 2003]; and (3) an automatic routine identified pixels in each sky flat image where the ratio of the sky flat to preflight flat differed from the median of that sky flat by more than 3 standard deviations. All of these problematic pixels were replaced with values calculated by dividing the value of that pixel in the preflight flatfield image by the median value of the pixel in the preflight flatfield image and multiplying by the median value for that pixel in the sky flat image. Because of detector edge effects [Bell *et al.*, 2003], all of

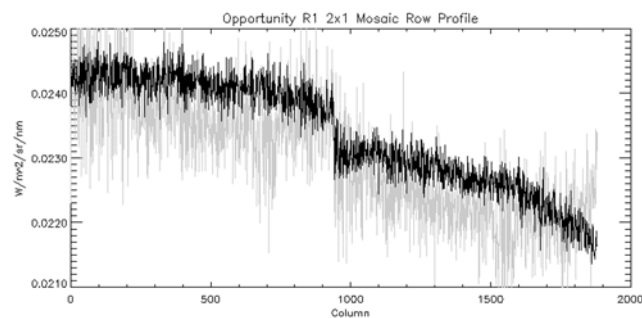


**Figure 14.** Row profiles from a transect of sky pixels within a mosaic created from Opportunity sol 85 sequence P2432, filter R1 images. The gray points are from a row profile of this mosaic calibrated using the preflight flatfield. The black points are from a profile of the same row of this mosaic calibrated using the flight flatfield. The  $x$  axis is column number, and the  $y$  axis is calibrated radiance value, in  $\text{W/m}^2/\text{sr/nm}$ .

the uncalibrated sky flat images had unusable values in the edge two columns (columns 0 and 1023). In addition to this, the Spirit (MER-A) L1 filter sky flat had unusable values in columns 1 and 1022, and the Opportunity (MER-B) L1 filter sky flat had unusable values in columns 1, 2 and 1022. Thus all of the values in the two edge columns in each flight flatfield image and the additional columns in the MER-A and MER-B L1 flight flatfield images were replaced with values of 1.0.

### 2.5.3. Application and Validation

[56] The processing steps described above resulted in the generation of a complete set of flight flatfield images for all 28 nonsolar filters on the four flight Pancams.

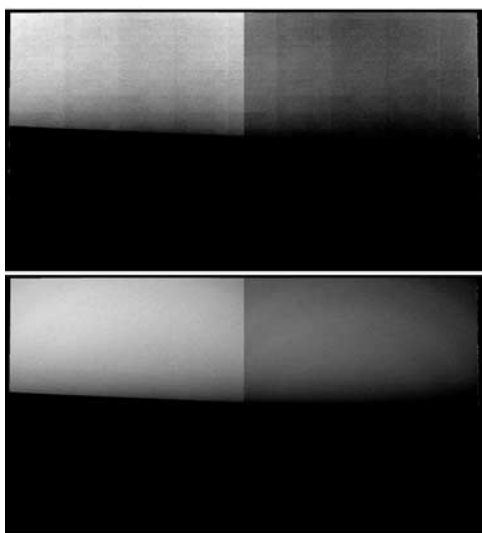


**Figure 15.** (top) The mosaic used to create the row profiles in Figure 14 (Opportunity sol 85 sequence P2432, filter R1), calibrated with the preflight flatfield and stretched to bring out details in the part of the mosaic that imaged the sky. (bottom) The same mosaic, calibrated with the flight flatfield and stretched to bring out details in the part of the mosaic that imaged the sky.

Visually, most of the new in-flight flatfields are indistinguishable from the preflight flats shown by *Bell et al.* [2003]. However, we have found that the flight flatfield images perform either as well as or better than the preflight flatfield images with respect to removing high- and low-frequency flatfield effects from flight images. For example, the Opportunity R1 (430 nm) filter flight flatfield is a significant improvement over the preflight version. Figure 14 shows row profiles of a mosaic that imaged part of the sky calibrated using both the preflight flatfield and the flight flatfield. The noise is greatly reduced with the use of the flight flatfield for this camera/filter combination. Figure 15 shows a comparison of the same R1 filter mosaic calibrated with the preflight flat and the flight flatfield, both contrast enhanced to show subtle detail in the sky portion of the images. The improvement for the R1 filter on Opportunity is the most dramatic example, and the improvements are important scientifically, as much of the subtle morphologic evidence for laminations within Meridiani outcrop materials comes from Pancam images through the blue filters [e.g., *Bell et al.*, 2004b; *Grotzinger et al.*, 2005]. Figures 16 and 17 show examples of results typical for the other Pancam filters, and Table 13 summarizes the similarities in noise levels between the preflight and in-flight flatfield images.

[57] The largest source of uncertainty in the flight flatfield creation process is the modeling and removal of the planar background for each in-flight sky flat image. As described above, the planar background removed from each image was determined by calculating the best fit plane for each image. We tested whether any additional “tilt” of this plane might be needed by examining several mosaics that imaged part of the sky in each filter. Figure 18 shows typical examples of possible evidence of a small additional tilt that might be needed to remove better the low-frequency component of the Pancam flatfield. The magnitude of the image-to-image offsets in sky radiance is 2% to 4% in the worst cases that we have analyzed. We found that while we can derive sets of tilt factors to apply to the flatfields to minimize these

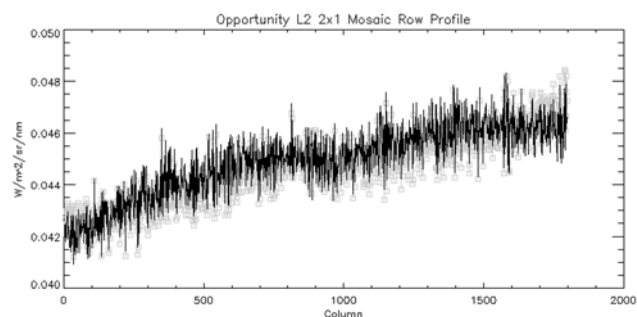


**Figure 16.** Row profiles from a transect of sky pixels within a mosaic created from Opportunity sol 24 sequence P2382, filter L2 images. The gray points are from a row profile of this mosaic calibrated using the preflight flatfield. The black points are from a profile of the same row of this mosaic calibrated using the flight flatfield. The  $x$  axis is column number, and the  $y$  axis is calibrated radiance value, in  $\text{W/m}^2/\text{sr/nm}$ .



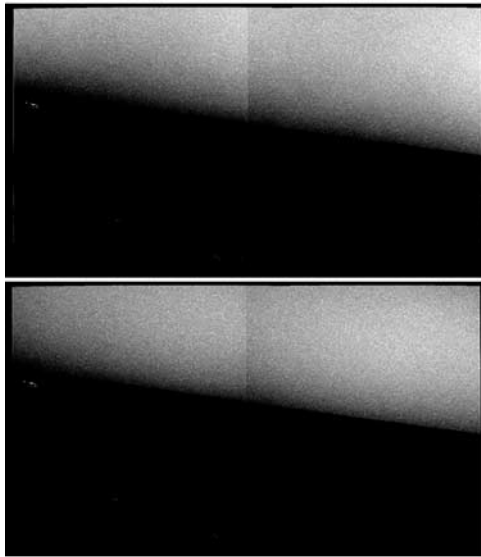


**Figure 17.** (top) The mosaic used to create the row profiles in Figure 16 (Opportunity sol 24 sequence P2382, filter L2), calibrated with the preflight flatfield and stretched to bring out details in the part of the mosaic that imaged the sky. (bottom) The same mosaic, calibrated with the flight flatfield and stretched to bring out details in the part of the mosaic that imaged the sky.

small image-to-image offsets for individual sequences, the magnitude and even direction of the required tilt are not consistent for different sequences with the same camera/filter combination. Thus we cannot apply a single set of tilts that will minimize these effects in all images, and so we conclude that these kinds of image-to-image variations are probably indicating real variations in sky brightness with time and azimuth during the course of mosaic acquisition. Therefore no additional residual tilt corrections were applied to the flight flatfields. Researchers interested in modeling low-spatial-frequency Pancam radiance information (e.g., for sky brightness or surface albedo studies) and who require accuracy better than 5-10% should examine carefully and perhaps revisit the methods and uncertainties used in our flatfield in-flight calibration procedure.

## 2.6. Bad Pixel Correction

[58] Hot pixels in the masked region were mentioned earlier, and dealing with them is straightforward because even in the worst case they are not observed to supply enough dark current to cause saturation. This is not always the case with hot pixels in the active region, however. At high enough temperatures, and long enough exposure times, hot pixels in the active region of the CCD can easily saturate the CCD with dark current alone. No pixels were observed to be truly “bad” (always saturated with dark current) during preflight calibration, and only one Pancam active region pixel (out of  $>4 \times 10^6$ ) has been observed to become bad during the course of the mission to date (Opportunity left Pancam S/N 114, pixel (10,553), which became saturated with dark current in every dark image acquired after SCLK 133242555, on sol 57). If it is determined that a pixel is saturated with dark current even

**Table 13.** Comparison of Noise Levels in Pancam Preflight and In-Flight Flatfields

| Filter             | Preflight $1\sigma$ | Flight $1\sigma$ |
|--------------------|---------------------|------------------|
| <i>Spirit</i>      |                     |                  |
| L1                 | 0.0308              | 0.0289           |
| L2                 | 0.0314              | 0.0288           |
| L3                 | 0.0344              | 0.0298           |
| L4                 | 0.0357              | 0.0329           |
| L5                 | 0.0348              | 0.0312           |
| L6                 | 0.0356              | 0.0319           |
| L7                 | 0.0337              | 0.0304           |
| R1                 | 0.0327              | 0.0310           |
| R2                 | 0.0215              | 0.0209           |
| R3                 | 0.0224              | 0.0215           |
| R4                 | 0.0239              | 0.0194           |
| R5                 | 0.0196              | 0.0180           |
| R6                 | 0.0181              | 0.0192           |
| R7                 | 0.0185              | 0.0191           |
| <i>Opportunity</i> |                     |                  |
| L1                 | 0.0229              | 0.0246           |
| L2                 | 0.0242              | 0.0249           |
| L3                 | 0.0259              | 0.0260           |
| L4                 | 0.0295              | 0.0309           |
| L5                 | 0.0297              | 0.0311           |
| L6                 | 0.0328              | 0.0334           |
| L7                 | 0.0366              | 0.0361           |
| R1                 | 0.0327              | 0.0266           |
| R2                 | 0.0256              | 0.0269           |
| R3                 | 0.0264              | 0.0256           |
| R4                 | 0.0251              | 0.0254           |
| R5                 | 0.0233              | 0.0227           |
| R6                 | 0.0213              | 0.0227           |
| R7                 | 0.0222              | 0.0232           |

without additional signal from the scene, that pixel is deemed to be a “dark-saturated pixel” in the image, and its value in the calibrated image is replaced by the median of adjacent good pixels. Also, because saturated pixels bleed charge into adjacent pixels in the same column, adjacent pixels in the same column are also marked as “bad.” We distinguish between these bad pixels due to dark-current saturation, and other pixels that are saturated because of the combined effects of dark current and signal from the scene (scene-saturated).

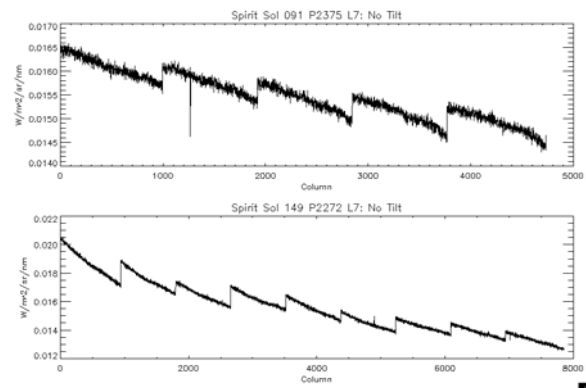


**Figure 18.** Row profiles from a transect of sky pixels within a mosaic created from Spirit Pancam data. (top) The sol 091 data is a 5 column mosaic, and (bottom) the sol 149 data is a 9 column mosaic. All of the images used to make these mosaics were calibrated using the flight flatfields. The  $x$  axis is column number, and the  $y$  axis is calibrated radiance value, in  $\text{W}/\text{m}^2/\text{sr}/\text{nm}$ .

[59] Scene-saturated pixels are handled differently than those pixels determined to be bad solely because of dark current. Because the extent of the saturation may vary, and various approaches could be taken to deal with such pixels, the calibration process does not attempt to interpolate these values based on surrounding data. Instead, the scene-saturated pixels are specially marked by being set equal to the value of the INVALID\_CONSTANT keyword denoted in the PDS image label, and it is left to the user to determine how best to deal with them. In the rare event of a dark-saturated pixel surrounded by scene-saturated pixels, the interpolated value will be “scene-saturated” and set to the value of the INVALID\_CONSTANT.

[60] Unfortunately, when pixels are saturated (regardless of whether it is due to dark current or not), this will also lead to a breakdown in the analytical shutter smear removal algorithm, which relies on being able to determine the scene-dependent component of the pixel value. In the case of dark-saturated pixels, the interpolated value will be used, but in the case of scene-saturated pixels, the only knowledge of the actual scene-dependent component is that it is larger than what can be measured by the CCD. In these cases, the shutter smear removal algorithm will remove the maximum measurable component, which is a lower bound on the actual value. When working with calibrated images that were not shutter-corrected on board, users will have to be aware that scene-saturated pixels can result in unremoved shutter smear upstream of the saturated pixel.

## 2.7. Radiance Calibration

[61] Absolute calibration of Pancam images is required in order to generate true-color data products or to extract spectra from surface units to compare directly with laboratory mineral and mineral mixture spectra. The Pancam calibration pipeline generates output files known as “RAD” images, where RAD refers to radiance. RAD images are data that have been converted to units of scene radiance, in  $\text{W}/\text{m}^2/\text{nm}/\text{sr}$ , as sampled at the effective wavelength ( $\lambda_{\text{eff}}$ ) of the filter used.

[62] In general, the scene radiance viewed by the detector,  $L$ , is related to the average DN value measured by the camera via a radiance conversion coefficient,  $K(T)$ , such that

$$L = K(T) \cdot \text{dn\_per\_s}, \quad (20)$$

where  $\text{dn\_per\_s}$  is the bias, dark, flatfield-corrected DN value divided by the exposure time, and  $T$  is the CCD temperature of the camera. The functional form of the temperature dependence of  $K$  is assumed to be

$$K(T) = K_0 + K_S \cdot T \quad (21)$$

[63] The linear nature of the responsivity versus temperature relationship was determined from preflight calibration observations over a wide range of Pancam flight operating temperatures [Bell et al., 2004a]. The responsivity coefficients  $K_0$  and  $K_S$  are calculated for each camera/filter combination by performing a linear fit to values of  $K(T)$  derived during preflight calibration. The derived values for  $K_0$  and  $K_S$  that were used for Pancam images calibrated using the preflight models are given by Bell et al. [2003].

Here we describe additional details of the radiometric calibration process, including modifications based on in-flight measurements and performance.

[64] For the Pancam preflight integrating sphere calibration measurements,  $L$  equals the calibrated integrating sphere radiance incidence on the camera,  $\text{Sp}(\lambda)$ , in  $\text{W}/\text{m}^2/\text{nm}/\text{sr}$  at the effective wavelength of the Pancam filter used. Therefore

$$L = \text{Sp}(\lambda_{\text{eff}}) \quad (22)$$

so that

$$\text{Sp}(\lambda_{\text{eff}}) = K \cdot \text{dn\_per\_s} \quad (23)$$

where  $\text{dn\_per\_s}$  is understood in this case to refer to the mean value of (DN/sec) for the approximately 10 to 50 images of the integrating sphere obtained during calibration at each camera/filter/temperature combination, divided by the exposure time used for those images.

[65]  $\text{Sp}(\lambda_{\text{eff}})$  values are derived from data obtained during thermal vacuum calibration where the voltage output of a NIST-calibrated diode was recorded at 50 nm intervals between 350 and 1100 nm. These voltage readings were converted to absolute radiances using a diode calibration performed at the JPL standards lab.

[66] Next, we could just divide  $\text{Sp}(\lambda_{\text{eff}})$  by  $\text{dn\_per\_s}$  to get  $K$ , but this assumes that the input spectrum on Mars (sunlight) will be the same shape as the spectrum of the integrating sphere in the lab. We know this to be false based on the sphere diode measurements. However, this method can be used to generate approximate radiance coefficients for validation of the more rigorously derived coefficients described below.

[67] To be more rigorous, we need to proceed as follows: Let  $\text{Rp}(\lambda)$  be the responsivity of the camera system (CCD QE, optics and filter transmissivities) as a function of wavelength, in unknown units, from the normalized monochromator-derived Pancam geology filter profiles [Bell et al., 2003]. Also let  $\text{Rk}(\lambda) = C \cdot \text{Rp}(\lambda)$  be the responsivity of the camera system as a function of wavelength in known units  $[(\text{DN}/\text{sec}/\text{nm})/(\text{W}/\text{m}^2/\text{nm}/\text{sr})]$ , where  $C$  is the responsivity conversion coefficient. First we need to find  $\text{Rk}$ . We start with:

$$\text{dn\_per\_s} = \int \{\text{Sp}(\lambda) \cdot \text{Rk}(\lambda)\} d\lambda \quad (24)$$

and thus

$$\text{dn\_per\_s} = \int \{\text{Sp}(\lambda) \cdot C \cdot \text{Rp}(\lambda)\} d\lambda \quad (25)$$

$C$  is the only unknown, and it is a constant so we can pull it out, yielding

$$C = \text{dn\_per\_s} / \int \{\text{Sp}(\lambda) \cdot \text{Rp}(\lambda)\} d\lambda \quad (26)$$

And so we have

$$\text{Rk}(\lambda) = \text{Rp}(\lambda) \cdot \text{dn\_per\_s} / \int \{\text{Sp}(\lambda') \cdot \text{Rp}(\lambda')\} d\lambda' \quad (27)$$

and thus we know the camera responsivity in general as a function of wavelength.

[68] On Mars, however, the input source is not the integrating sphere, but is sunlight filtered through and scattered by the Martian atmosphere and then modulated by the reflectivity of the Martian surface. We used Pathfinder IMP data [Maki *et al.*, 1999] to generate a “typical” input radiance spectrum,  $St(\lambda)$ , expected from average bright regions on Mars. Based on past experience, we can assume that the actual radiance measured by Pancam,  $Sa(\lambda)$ , will be some scalar multiple of this typical spectrum, such that  $Sa(\lambda) = a \cdot St(\lambda)$ , where  $a$  is a unitless scaling constant. Substituting this source instead of the sphere into equation (24) above, on Mars we will have

$$dn\_per\_s = \int \{a \cdot St(\lambda) \cdot Rk(\lambda)\} d\lambda \quad (28)$$

or

$$a = dn\_per\_s / \int \{St(\lambda) \cdot Rk(\lambda)\} d\lambda \quad (29)$$

[69] Since the input radiance  $L = a \cdot St(\lambda_{eff})$  (equation (22), on Mars), then

$$a \cdot St(\lambda_{eff}) = K \cdot dn\_per\_s \quad (30)$$

(from equation (23)), and thus

$$K = a \cdot St(\lambda_{eff}) / dn\_per\_s \quad (31)$$

[70] Substituting into equation (29):

$$K = St(\lambda_{eff}) / \int \{St(\lambda) \cdot Rk(\lambda)\} d\lambda \quad (32)$$

[71] Thus equation (32) provides a rigorous way to estimate the radiometric conversion coefficients on Mars, using equation (27) to determine the camera responsivity, and assuming a “typical” Mars radiance spectrum as input.

## 2.8. Deriving Relative Reflectance: I/F, $R^*$ , and Estimated Bolometric Albedo

### 2.8.1. Reflectance Units

[72] Pancam reflectance products are generated as “IOF” files. IOF is defined as the ratio of the bidirectional reflectance of a surface to that of a normally illuminated perfectly diffuse surface. This is also known as the *radiance factor* [Hapke, 1993]. If the effects of the Martian atmosphere are neglected, then we can also say that

$$IOF = \frac{I}{\pi F} \quad (33)$$

where  $I$  is equal to the measured scene radiance, and  $\pi F$  is equal to the solar irradiance at the top of the Martian atmosphere at the time of the observation and through a particular Pancam bandpass. Our terminology “IOF” comes from the analogy with many previous spacecraft imaging data sets where “ $I/F$ ” is generated as a common reflectance product. IOF is useful in that it places the data in the same

context as laboratory or telescopic reflectance measurements or radiance factor data from previous Mars orbiter or lander missions.

[73] A related parameter,  $R^*$  (“R-star”), was defined and utilized by Reid *et al.* [1999] for Imager for Mars Pathfinder (IMP) reflectance products.  $R^*$  was defined by Reid *et al.* [1999] as “the brightness of the surface divided by the brightness of an RT (Radiometric Calibration Target) scaled to its equivalent Lambert reflectance.” Some researchers have called this quantity “relative reflectance” because it is the reflectance of the scene relative to that of a perfectly Lambertian albedo = 1.0 surface in an identical geometry. In general,  $R^*$  can be defined as the ratio of the reflectance of a surface to that of a perfectly diffuse surface under the same conditions of illumination and measurement. This is also known as the *reflectance factor* or *reflectance coefficient* [Hapke, 1993], and it is essentially an approximation of the Lambert albedo within each Pancam bandpass. Units of  $R^*$  can be obtained by dividing Pancam IOF images by the cosine of the solar incidence angle at the time of the observation.

[74]  $R^*$  is useful in that it allows for direct comparison between spectra taken at different times of day, and more straightforward comparison with laboratory spectra. Images calibrated to  $R^*$  also have the advantage of being at least partially “atmospherically corrected,” because observations of the Pancam calibration target also include the average diffuse sky illumination component of the scene radiance [e.g., Reid *et al.*, 1999; Thomas *et al.*, 1999]. Thus, for flat-lying surfaces in the same plane as the surface of the calibration target, the diffuse sky component is essentially removed by calibrating relative to the target. It should be noted that IOF and  $R^*$  differ only by a constant multiplicative scaling factor, and not in the shape of their spectra, as long as all of the images in a multispectral sequence are acquired in rapid-enough succession that there have not been significant variations in solar incidence angle as a function of wavelength.

[75]  $R^*$  images acquired using the L1 (EMPTY) filter provide a good estimate of the Lambert bolometric albedo. It is only an approximation, partly because the L1 filter bandpass does not sample all of the solar visible wavelengths, and partly because the Pancam calibration target is not perfectly Lambertian and our model does not perfectly compensate for its non-Lambertian nature [Bell *et al.*, 2003]. However, the uncertainties associated with each of these factors is small, and so  $R^*$  images through the L1 filter produce quick-look estimates of the bolometric albedo that are remarkably similar to those derived from orbital MGS/TES and Viking/IRTM bolometric albedos [Bell *et al.*, 2004a, 2004b].

### 2.8.2. Approximating I/F Using the Radiance Data

[76] Pancam radiance data can be used to quickly estimate the approximate reflectivity of the scene through each filter by dividing the derived radiances in the RAD files by an estimate of the radiance of the scene. Without using observations of the calibration target or a detailed sky diffuse illumination model, the simplest approach is to use the radiance spectrum of sunlight at the top of the Earth’s atmosphere, scaled for the appropriate heliocentric distance of Mars at the time of the observations, as the incident radiance spectrum. Table 14 provides such an



**Table 14.** Pancam Radiance to “Approximate Reflectivity” Scale Factors

| Filter              | $\lambda_{\text{eff}}$ , nm | Bandpass, nm | Scale Factor |
|---------------------|-----------------------------|--------------|--------------|
| <i>Left Camera</i>  |                             |              |              |
| L1                  | 739                         | 338          | 0.18122      |
| L2                  | 753                         | 20           | 0.17854      |
| L3                  | 673                         | 16           | 0.21574      |
| L4                  | 601                         | 17           | 0.24793      |
| L5                  | 535                         | 20           | 0.27290      |
| L6                  | 482                         | 30           | 0.29164      |
| L7                  | 432                         | 32           | 0.23626      |
| <i>Right Camera</i> |                             |              |              |
| R1                  | 436                         | 37           | 0.25896      |
| R2                  | 754                         | 20           | 0.17825      |
| R3                  | 803                         | 20           | 0.16015      |
| R4                  | 864                         | 17           | 0.13942      |
| R5                  | 904                         | 26           | 0.12464      |
| R6                  | 934                         | 25           | 0.11813      |
| R7                  | 1009                        | 38           | 0.10161      |

estimate of the incident sunlight through each Pancam filter, using as the incident radiance the weighted average of solar irradiance spectrum of *Colina et al.* [1996] over the Pancam bandpasses divided by  $\pi$  and divided by  $(1.50 \text{ AU})^2$  (the average heliocentric distance of Mars during the first 30 sols of the MER missions). Dividing the Pancam radiance data by the appropriate value from Table 14 results in a fast but simplistic estimate of the reflectivity of the scene that could provide a useful start toward comparing Pancam spectra to laboratory mineral or mineral mixture reflectivity spectra. However, note that the results will only be approximate: estimated reflectivity spectra derived this way will include additional spectral features induced by the presence of significant (reddening) scattered radiance from the dust-laden Martian atmosphere, and the estimated absolute reflectance levels would need to be corrected for the  $e^{-\tau}$  effect of attenuation by atmospheric dust at the time of the observation [Lemmon et al., 2004].

### 2.8.3. Deriving I/F and R\* Using Observations of the Pancam Calibration Target

[77] A more rigorous calibration approach used during tactical rover operations on Mars is to use near-in-time observations of the Pancam calibration target to derive estimated scene reflectances relative to the standard reflectance materials on the target [Bell et al., 2003]. This approach minimizes the spectral effects of atmospheric dust scattering and absorption and provides absolute reflectance levels to within 5-10% for flat-lying surfaces with well-behaved photometric functions. However, this approach requires the use of a photometric model of the calibration target standard reflectance materials as well as a model of the spectral effects of the time-dependent airborne dust deposition on the target [Bell et al., 2003; J. Sohl-Dickstein et al., Radiative transfer modeling of dust-coated calibration target materials: Application to calibration target observations on Mars and the Pancam Calibration Pipeline, manuscript in preparation, 2005 (hereinafter referred to as Sohl-Dickstein et al., manuscript in preparation, 2005)]. This approach can also benefit from the use of a sky illumination model [e.g., Tomasko et al., 1999; Lemmon et al., 2004] to estimate and separate the diffuse versus direct sources of illumination.

### 2.8.3.1. Assumptions

[78] Both IOF and R\* calibrated images are restricted by the following set of assumptions: (1) All illumination comes directly from a point source at the Sun. This assumption is most critical for the IOF images, where the overall scene brightness scales with  $\cos i$ , the cosine of the solar incidence angle; (2) The scene being imaged is perfectly flat. It should be possible to use surface normal maps to remove this restriction for many observations, but this is not currently performed as part of the normal Pancam flight calibration pipeline; and (3) The scene elements being imaged are Lambertian. Without knowing the full Bidirectional Reflectance Distribution Function (BRDF) for a scene element, this is the most productive assumption which can currently be made. There are many sets of photometry observations which may be used in the future for a more accurate characterization of the BRDF of some limited subset of scene elements [e.g., Seelos et al., 2004; Johnson et al., 2006].

### 2.8.3.2. Pancam Calibration Target

[79] Each rover carries a calibration target to allow characterization of the lighting environment. As described in detail by Bell et al. [2003], the target consists of seven silicone RTV (GE RTV655) regions. These regions are pigmented with either titanium dioxide or carbon black to raise or lower their reflectivity and generate three gray regions, and with submicron powders of hematite, goethite, chromium oxide, and cobalt aluminate to generate red, yellow, green, and blue color chips. There is also a shadow-casting gnomon in the center, allowing regions illuminated only by diffuse sky illumination to be sampled as well. The BRDF of the calibration target was thoroughly characterized across both wavelength and temperature before launch. This allowed the development of a model of the target's reflectance as measured by Pancam in any lighting environment. Further details about the target, the BRDF model, and laboratory spectra of calibration target materials are presented by Bell et al. [2003]. Once on Mars, however, the calibration target began to rapidly accumulate dust and its appearance deviated significantly from that measured preflight (Figure 19). In order to compensate for this, a model of the effect of dust on the calibration target was developed, as described below.

### 2.8.3.3. Preflight Pancam Calibration Target Measurements and Model

[80] As described by Bell et al. [2003, 2004c], the Pancam calibration target materials were characterized prior to flight from (1) hemispheric reflectances measured from 348 to 1200 nm at 4 nm spectral sampling using a Cary-14 directional-hemispheric spectrometer at the NASA Johnson Space Center [e.g., Morris et al., 1985]; (2) directional hemispheric reflectances measured as a function of temperature from 199 K to 318 K and over a wavelength range from 350 nm to 2500 nm by R. Clark and colleagues at the United States Geologic Survey Denver Spectroscopy Laboratory [Clark et al., 1993]; (3) full BRDF characterization by M. Shepard using the Bloomsburg University Goniometer facility [Shepard, 2001]; and (4) in-plane BRDF characterization through a set of flight spare Pancam filters and a second set of 19 narrowband filters with effective wavelengths between 400 nm and 1050 nm by P. Pinet, Y. Daydou and P. Depoix at CNES



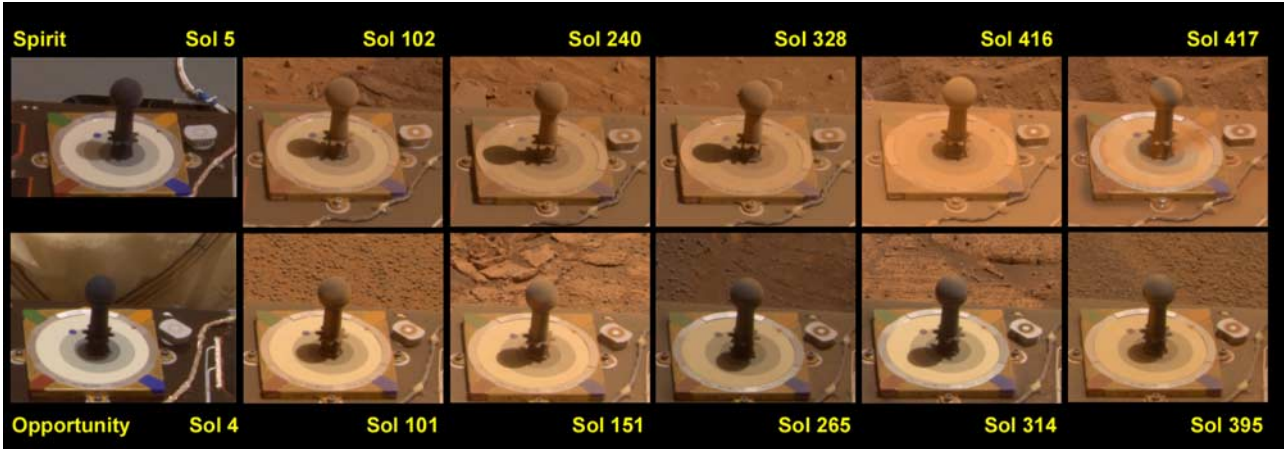


**Figure 19.** Approximate true color images of the Spirit (top row) and Opportunity (bottom row) Pancam calibration target over the course of each mission, showing visual evidence for a significant amount of dust accumulation on the targets. Target images that have the same or similar lighting geometry for each rover are compared here in order to minimize any photometric effects on the observed color. In general, the targets have reddened with time; however, there is visual evidence for occasional “cleaning” of some dust from each target (e.g., between Opportunity sols 151 and 265 and most dramatically between Spirit sols 416 and 417). Each image was processed identically using the true color techniques described in section 3.2.

in Toulouse, France [Pinet *et al.*, 2001]. Subsets of these measurements were used to construct a mathematical model of the BRDF of the calibration target materials, consisting of the physically based He-Torrance model [He *et al.*, 1991], borrowed from the realm of computer science, combined with the Hapke backscatter term [Hapke, 1993]. The function developed, referred to as  $R_{\text{pre-flight}}(\lambda, az, el, az', el')$ , returns a reflectance coefficient as a function of wavelength, azimuth and elevation of incident ( $az, el$ ) and emitted ( $az', el'$ ) light. The azimuth and elevation of the observer (Pancam) is fixed by the geometry of the rover. Specifically, the calibration target is viewed at a fixed emission angle of  $el' = 53.5^\circ$  as measured in the traditional photometric sense of up from the plane of the rover deck, with the emission vector pointing toward the cameras (however, in the PDS image file header, this angle is reported as an “elevation” of about  $36.5^\circ$ ; Pancam elevation angles are defined with positive elevation angles measured down from a reference plane parallel to the rover deck and at the height of the cameras, with the elevation vector pointing away from the cameras in the opposite sense as the emission vector), and at fixed azimuth angles of  $az' = 354.2^\circ$  for the left Pancam and  $az' = 349.1^\circ$  for the right Pancam. More details on the preflight Pancam calibration target model are given by Bell *et al.* [2003].

#### 2.8.3.4. Flight Pancam Calibration Target Model

[81] After RAD files are produced for a calibration target sequence using the procedure outlined in section 2.7, calibration analysts manually select Regions of Interest (ROIs) from calibration target images. One ROI is chosen from each of the 4 color chips and 3 gray rings. In addition, ROIs are chosen in the shadowed regions of each of the rings if they are available (see Figure 20). The average and standard deviations of the pixel values within each region of interest are calculated.

[82] Using the known position of the Sun in the sky to derive the elevation and azimuth of the incident illumination,

simplified predicted calibration target reflectance values are then calculated for the 7 RTV regions by taking a weighted average of the  $R_{\text{pre-flight}}$  calibration target model over the appropriate Pancam bandpass:

$$R_{\text{predicted}}^{\text{simple}} = \frac{\int R_k(\lambda) \cdot R_{\text{pre-flight}}(\lambda, az, el, az', el') \cdot d\lambda}{\int R_k(\lambda) \cdot d\lambda} \quad (34)$$

where  $R_k(\lambda)$  is the responsivity of the camera system as a function of wavelength in known units [(DN/sec/nm)/

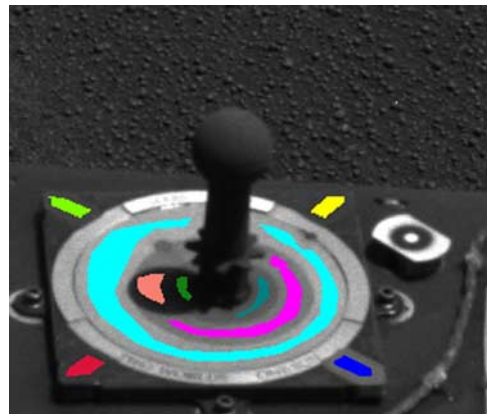


**Figure 20.** Regions of interest selected by calibration analysts on an image of the Pancam calibration target. Each color represents groups of pixels selected either manually or via an automated routine from each of the seven distinct colored or gray scale regions of the target surface plus, if available, shadowed parts of the same surfaces. This particular image was acquired through the L7 filter on Opportunity sol 365 as part of Pancam imaging sequence P2093.

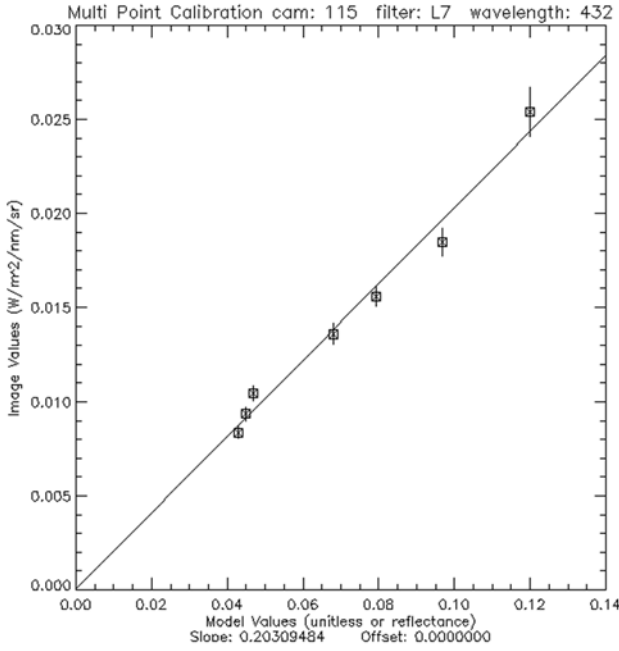


**Figure 21.** Plot showing an example of the modeled ( $R_{\text{predicted}}$ ) versus measured mean pixel values in each of the 7 nonshadowed Regions of Interest on the Pancam Calibration Target. The slope of the best fit line to these points is used to convert near-in-time Pancam images from units of radiance into units of relative reflectance.

( $\text{W/m}^2/\text{sr/nm}$ ), as defined in section 2.7,  $az'$  and  $el'$  are the calibration target emission angles as defined above, and appropriate values for ( $az, el$ ) are filled in using the rover orientation and solar position keywords from the PDS file headers (Appendix B).

[83] A best fit line is then found relating the measured average calibration target region RAD values for all 7 regions to their model values of  $R_{\text{predicted}}$  (see Figure 21). Because the bias and dark current models (especially at cold temperatures) are more accurate than the calibration target model, and because properly calibrated images should yield zero signal levels for zero input radiance, the offset of the best fit line is constrained to pass through the origin. Investigation of a subset of cases using unconstrained fits yielded offset values of approximately zero, within the noise of the data, validating our forced-constraint approach. Visual inspection of the fit line by calibration analysts is used to verify the quality of the fit and to iterate on the selection of ROIs in cases where problems exist (e.g., cosmic ray hits, decompression artifacts, saturation/Sun glints, shadows from other rover deck structures, etc.). The slope of the fit line,  $m$ , is then used, along with the assumed  $\cos i$  falloff in IOF relative to the BRDF, to convert between RAD and IOF in the absence of any other effects:

$$IOF = RAD \cdot m \cdot \cos(i_{\text{caltarget}}) \quad (35)$$

[84] The simple form of  $R_{\text{predicted}}$  as described above is modified, however, to take into account dust on the caltarget.

### 2.8.3.5. Modification for Dust Accumulation

[85] Over the course of the rover missions, the calibration targets on both vehicles have become increasingly dusty (Figure 19). It is necessary to correct for the spectral effects of this dust, otherwise the calibration target's reflectance properties become increasingly skewed by the spectrum of the dust component, and the derived calibration becomes increasingly inaccurate. The effect of the dust is particularly visible in the blue and near-UV Pancam filters, where the dust is most strongly absorbing.

[86] In order to correct for this, the Hapke model of bidirectional reflectance of a two-layer medium [Hapke, 1993; p. 251] was modified to accept the preflight caltarget material as a substrate. Hapke's initial bidirectional radiance integral was broken down into  $\tau < \tau_0$  and  $\tau > \tau_0$  regions (where  $\tau$  is the total opacity from the top of the upper layer), and the  $\tau > \tau_0$  region was reduced to surface effects at a membrane covering the top of the substrate, producing a modified version of Hapke's equation for radiance at the detector of

$$I_D(\Omega) = \int_0^{\tau_0} \frac{1}{\mu} [F(\tau, \Omega) + \omega_U \varphi(\tau)] e^{-\tau/\mu} d\tau + [F(\tau_0, \Omega) + \omega_L I_2(\tau_0)] e^{-\tau_0/\mu} \quad (36)$$

where all symbols represent the quantities as defined by Hapke [1993].

[87] The lower level volume angular scattering function  $p_L(g)$ , which depends only on phase angle, was then replaced with an analogous bidirectional scattering function  $q_L(az, el, az', el')$ , where again  $az, el$  define the incident vector, and  $az', el'$  define the emission vector. The bidirectional scattering function was defined as

$$q_L(az, el, az', el') = R_{\text{predicted}}(az, el, az', el')/r_S \quad (37)$$

where  $r_S$  is the spherical reflectance of each of the calibration target materials (as measured at NASA/JSC), convolved to the same Pancam bandpass as  $R_{\text{predicted}}$ . The bidirectional scattering function simplifies to the angular scattering function in the case of a Lambertian substrate. As well, the bidirectional scattering function fulfills an analogue of the angular scattering function's normalization constraint:

$$\int_{2\pi} \int_{2\pi} p(g) d\Omega d\Omega' = (2\pi)^2 \quad (38)$$

[88] The derivation of a modified two-layer bidirectional scattering function based on the modified assumptions outlined above is described in detail by Sohl-Dickstein et al. (manuscript in preparation, 2005).

[89] All the coating parameters were fitted to this model using a large number of calibration target images acquired for each rover over the course of the mission. The opacity of the dust layer,  $\tau_0$ , was allowed to vary as a 6th order polynomial over the course of the mission, but all other parameters were allowed only one value over the entirety of the mission for each rover. All illumination was assumed to come from a point source at the Sun, though this could be

changed in future iterations of the model. The fit was performed using a Levenberg-Marquardt least-squares minimization algorithm. Evaluation of the local slope was performed using numerical derivatives. In order to remove any effect of varying illumination intensity, one degree of freedom was sacrificed from the fit, and it was performed on ratios of reflectances between caltarget regions rather than on direct measures of reflectance. That is, it attempted to satisfy the series of equations

$$\frac{R_{predicted}^i}{R_{predicted}^j} = \frac{R_{measured}^i}{R_{measured}^j} \quad (39)$$

where  $i$  and  $j$  are indexes to caltarget subregions. More details on this derivation of this model and examples of its application and effects are given by Sohl-Dickstein et al. (manuscript in preparation, 2005).

## 2.9. Accuracy and Precision of the Calibration

[90] Uncertainties in the RAD calibration pipeline are difficult to quantify for the Pancam data, because they represent a complex combination of errors accumulated by the bias, dark current, and flatfield modeling/correction processes as well as the uncertainties in the preflight integrating sphere radiance scaling procedure. Based on preflight calibration data analysis, we estimated that our typical absolute radiance uncertainty would be  $\leq 7\%$ , an assumption that was validated by independent calibrated diode measurements from an engineering model Pancam [Bell et al., 2003]. In flight, Lemmon et al. [2004] attempted to estimate the level of uncertainty of calibrated Pancam data by comparing calibrated radiances from sky images to their model of expected sky radiance for the specific observing geometries and dust opacities encountered. For the Pancam filters at 432, 535, 601, 753, 864, and 1009 nm, they found an average difference between modeled and measured radiances of  $0.98 \pm 0.06$  for Spirit and  $1.11 \pm 0.08$  for Opportunity. Given the uncertainties and assumptions inherent in their sky model, these results appear to indicate that the absolute radiance calibration of Pancam flight data from Mars, calibrated using the methods and data files described above, is probably at least accurate to within the  $\sim 10\%$  level, and is probably actually slightly more accurate, especially for the longer wavelength, higher SNR filter observations.

[91] Uncertainties in the IOF calibration pipeline are even more difficult to quantify. Primary sources of error include the uncertainty in the photometric characterization of calibration target material BRDF ( $\sim 15\%$  absolute,  $\sim 5\%$  relative (M. Shepard, personal communication, 2004), errors based on the inaccuracy of our simplified assumptions about the diffuse sky illumination component of the scene signal (e.g., not all regions are viewed at the same solar incidence angle as the calibration target;  $\sim 30\text{--}50\%$  of illumination is diffuse in a typical image, though the majority of diffuse illumination comes from a region near the Sun, etc.), unevenness or rapid time variations in the dust distribution on the calibration target ( $< 15\%$  change in relative region intensity), and even minor remaining uncertainties in the camera bandpass characterization ( $< 10\%$ ). Combining these estimates would lead to a conservative error estimation of

$\sim 55\%$  in IOF values, *before* the poorly characterized errors in the dust model itself are incorporated. However, examination of the data indicates that the “real world” error is actually much smaller. For example, when considering the consistency of the (presumed nearly constant) global dust spectrum over the course of the mission, as well as when comparing the spectral shape of Pancam’s global dust measurements against those made during the Mars Pathfinder mission [e.g., Bell et al., 2000], the errors in our IOF calibration process appear to be  $\sim 10\%$  or less in spectral shape. Relative uncertainties in IOF, from filter-to-filter and between cameras on the same rover, are even smaller (typically  $1\text{--}5\%$  based on comparison of calibrated left and right camera data for images of the same scenes through overlapping filters), providing good confidence in the identification of even relatively weak spectral features in IOF-calibrated Pancam multispectral data sets. Relative precision from pixel-to-pixel in each Pancam image is best assessed from examination of the variance within regions extracted from the Pancam calibration target gray scale rings (e.g., Figure 21) which are, at least early in the mission, the only “known” uniform reflectance sources in the scene. The level of these pixel-to-pixel variations depends on the scene radiance (as expected for photon-dominated noise), and varies from about  $0.5\%$  to  $3.5\%$  for typical calibration target data sets, with a level below  $1\%$  for radiance levels consistent with those typical of average Mars surface materials.

## 2.10. Ancillary Calibration Files, Formats, Labels, and Other Sources of Information

[92] The procedures described in this section, which follow schematically the flowchart outlined in Figure 1, collectively define the Pancam in-flight calibration pipeline. Several of the steps in the pipeline involve the use or application of specialized ancillary tables and/or data files developed by the Pancam team as part of the calibration process. A list of these ancillary files is provided in Table 15. Researchers interested in reproducing or refining the calibration of Pancam images can obtain these files by request from the first author.

[93] A significant amount of additional information about Pancam images and their calibration state can also be obtained from the PDS label information that is included as an ASCII header on every archived Pancam EDR or RDR data file. A list and definitions of the PDS label keywords that are most relevant to Pancam calibration are included as Appendix B.

[94] Finally, Appendix C contains useful additional information and details about where to find archived Pancam EDRs and RDRs and how to decipher the information “stored” within the filenames themselves for Pancam (and all other MER camera) images.

## 3. Applications

[95] The Pancam in-flight calibration procedures and philosophies described in this paper have enabled a wide range of scientific and mission support activities. Three particular examples are described here: (1) identification and interpretation of visible to near-IR multispectral units based on 13 filter (11-color) Pancam radiance factor data;



**Table 15.** Ancillary Files Required for the Pancam In-Flight Calibration Pipeline<sup>a</sup>

| Filename                                       | Purpose                                    |
|--|--|
| <i>8-Bit to 12-Bit Resampling (Appendix A)</i> |  |
| mer_lut_N.txt                                  | 12-bit to 8-bit lookup table #N            |
| mer_inverse_lut_N.txt                          | 8-bit to 12-bit inverse lookup table #N    |
| <i>Bias Model</i>                              |  |
| mer_ccd_SSS_bias_coeffs_vv.dat                 | mean bias exponential coefficients         |
| mer_ccd_SSS_bias_offset_vv.img                 | row offset from mean bias (1D array)       |
| <i>Masked Region Dark Current Model</i>        |  |
| mer_ccd_SSS_dark_shutter_exp_coeffs_vv.dat     | mean shutter dark exponential coefficients |
| mer_ccd_SSS_dark_shutter_col_mn_flat_vv.img    | column-mean-flat values (1D array)         |
| mer_ccd_SSS_dark_shutter_col_flat_vv.img       | dark-flat values (2D array)                |
| mer_ccd_SSS_dark_shutter_hot_vv.dat            | hot-pixel information (table)              |
| <i>Active Region Dark Current Model</i>        |  |
| mer_ccd_SSS_dark_active_exp_coeffs_vv.dat      | mean active dark rate exponential coeffs   |
| mer_ccd_SSS_dark_active_flat_vv.img            | dark-rate-flat values (2D array)           |
| mer_ccd_SSS_dark_active_change_vv.dat          | pixels that have changed over time (table) |
| mer_ccd_SSS_dark_active_outlier_vv.dat         | special coefficients for outliers (table)  |
| <i>Flatfields</i>                              |  |
| MER_FLAT_SN_SSS_ff_Vvv.IMG                     | flatfield image, mean normalized to 1.0    |
| MER_FLAT_STDDEV_SN_SSS_ff_Vvv.IMG              | standard deviation of each pixel in flat   |

<sup>a</sup>Notes: SSS is the Pancam camera serial number, vv is a two-digit file version number designator, and ff is the two-character Pancam filter designation.

(2) derivation and utility of “true color” and scene chromaticity information based on calibrated Pancam radiance data; and (3) derivation and interpretation of “super resolution” morphology information based on calibrated Pancam images.

### 3.1. 13-Filter Pancam Multispectral Analysis

[96] Examples of both typical and end-member 13 filter (11 unique wavelength) multispectral units extracted from radiance factor (IOF) calibrated Pancam imaging sequences from both rovers are shown in Figure 22. Pancam spectra of typical bright and dark soil units at the Gusev and Meridiani landing sites compare favorably to previous telescopic spectra of classical bright and dark regions [e.g., *Bell et*

*al.*, 1990; *Mustard and Bell*, 1994] and IMP multispectral data for bright and dark soils at the Pathfinder landing site [*Smith et al.*, 1997; *Bell et al.*, 2000]. However, several new spectral classes unlike those previously seen have also been discovered in the Pancam data. At Gusev these are primarily dark, spectrally flat, ferrous-rich interiors of rocks, but at least one new class of bright soil has also been discovered. At Meridiani, unique new spectral units include the bright outcrop materials in Eagle crater and elsewhere, ferrous-rich rock cobbles and interiors, and even an iron-nickel meteorite. Additional details and compositional/mineralogic interpretations gleaned from Pancam multispectral imaging data for these and other spectral units are given by, for example, *Bell et al.* [2004a, 2004b], J. F. Bell et al. (Multispectral

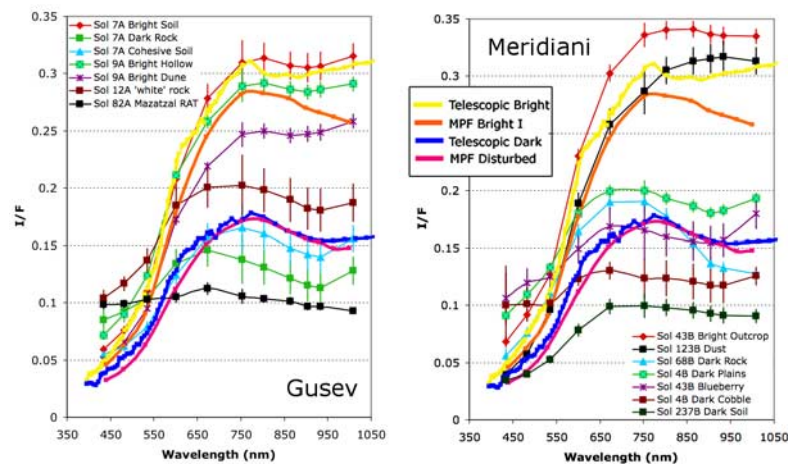


**Figure 22.** Spectral diversity discovered at the MER (left) Gusev and (right) Meridiani landing sites using Pancam 13 filter (11-color) multispectral radiance factor imaging data, calibrated using the in-flight calibration pipeline described here. The telescopic bright and dark region spectra are from *Bell et al.* [1990] and *Mustard and Bell* [1994]. The Mars Pathfinder (MPF) Bright I and dark Disturbed soil spectra are from *Bell et al.* [2000].



analyses of fine-grained materials at the Mars Exploration Rover Spirit landing site in Gusev crater, manuscript in preparation, 2005), *McSween et al.* [2004, 2006], *Lemmon et al.* [2004], *Soderblom et al.* [2004], *Bertelsen et al.* [2004], *Farrand et al.* [2006], W. H. Farrand et al. (VNIR analysis of rock outcrops at the Opportunity landing site, Meridiani Planum, Mars: Spectral properties, stratigraphy, and anomaly detection, manuscript in preparation, 2005), A. Wang et al. (Evidence of phyllosilicates in Woolly Patch, an altered rock encountered at West Spur, Columbia Hills, by the Spirit rover in Gusev crater, Mars, manuscript in preparation, 2005), and C. Weitz et al. (Soil grain analyses at Meridiani Planum, Mars, manuscript in preparation, 2005).

### 3.2. “True Color” and Chromaticity Derivation

[97] Calibration of Pancam images to absolute radiometric units enables us to generate estimates of the color of each multispectral scene as it would be perceived by an average person if they were viewing the scene on Mars. The process of creating such so-called “true color” images has an extensive literature and involves converting calibrated Spectral Power Distribution (SPD) information to the standard XYZ color space [e.g., *Carter et al.*, 2004]. The XYZ color space is modeled closely after a human’s perception of colors. The space can accurately describe the vast majority of the colors that can be registered by the human eye. Color representations within this space are strictly linear: a pair of colors separated by some arbitrary geometric distance will appear to be twice as different to the eye as another pair separated by only half the distance within the color space. The XYZ space tristimulus values represent the relative proportions of the three color primaries (red, green and blue) necessary to produce the color being measured. Chromaticity values ( $x$ ,  $y$ , and  $z$ ) are the X, Y, and Z tristimulus values normalized by their common sum, are often used as a way to compare color values from different locations and recorded by different instruments. The Pancam RAD images calibrated as described above to units of  $W/m^2/nm/sr$  are assumed to accurately describe the spectral power distribution of each image at each of the sampled Pancam wavelengths.

[98] Our true color calculation process is similar to the process developed by *Maki et al.* [1999] for IMP multispectral data. Image data are treated as a matrix of rectangular arrays, each of which represents radiance values per pixel for a specific wavelength. Pancam filters L2 through L7 (sampling approximately 360 to 830 nm) are used to provide the best possible coverage of the human visible spectral response. Initial colorimetry values are calculated as Commission Internationale de l’Eclairage (CIE) tristimulus values (the red, green, and blue components of human color vision [e.g., *Carter et al.*, 2004]). For an emissive source’s SPD, tristimulus values can be written in the form

$$\begin{aligned} X &= \int x(\lambda) SPD(\lambda) d\lambda \\ Y &= \int y(\lambda) SPD(\lambda) d\lambda \\ Z &= \int z(\lambda) SPD(\lambda) d\lambda \end{aligned} \quad (40)$$

where the integrals are over the products of the spectral power distribution and the standard CIE color matching

function values integrated over the range of the human visible spectrum. As the Pancam data sample the range of human spectral response through narrow, nonoverlapping bandpasses [*Bell et al.*, 2003] rather than via a continuous function, we apply a two point Newton-Cotes formula to the integrals, which then become sums of the products of the measured SPD and the color matching functions, scaled by a common factor.

[99] Since the final color is determined by ratios of the tristimulus values rather than their absolute magnitudes, we can neglect the common scaling factor and use only the summations. While this is mathematically correct, it makes comparison of tristimulus values problematic. Therefore we calculate chromaticity values (normalized tristimulus values), and since the three chromaticity values ( $x$ ,  $y$ , and  $z$ ) represent the three tristimulus values scaled by their sum, only the  $x$  and  $y$  values ultimately need to be reported [*Maki et al.*, 1999].

[100] Because the CIE standard color matching functions  $x(\lambda)$ ,  $y(\lambda)$ , and  $z(\lambda)$  vary significantly throughout the visible spectrum, it is necessary to describe them with a high degree of accuracy. We model these functions in increments of 1 nm in the 360 to 830 nm range for a total of 471 data points per function. To create an equal number of data points for the SPD data, a cubic spline is applied to the discrete wavelength Pancam RAD values. Multiplying this by the CIE function values and summing produces tristimulus values for each pixel in the image that can then be used to generate normalized chromaticity values.

[101] We augment this process by then transforming the images further into the sRGB color space, which is a common standard presently used by many Internet browsers and image processing/display programs and devices [*Stokes et al.*, 1996]. The sRGB space can be defined in terms of standard CIE colorimetric values, which themselves can be calculated from a defined reference viewing environment and knowledge of the spectral sensitivities of the display or output device used. Since sRGB tristimulus values are linear combinations of CIE tristimulus values they can be computed by convolving the CIE tristimulus set for a given pixel with a standard matrix [*Stokes et al.*, 1996]. The final nonlinear sRGB values are created by fitting the tristimulus values to a 2.2 gamma curve, which corresponds to the standard used in most CRT monitors.

[102] The standard matrix is calculated from CIE chromaticities for the red, green, and blue ITU-R BT.709 colorimetry standard reference primaries, and the Standard Illuminant D65 [e.g., *Stokes et al.*, 1996; *Carter et al.*, 2004]. Following the standard procedure, the produced values are nonlinearized by multiplying by 12.92 for values less than 0.00304 and by applying the equation  $1.055 \bullet [R,G,B]^{1/24} - 0.055$  for all other values. Finally, values are scaled to the range of 0 to 255 with 24 bit encoding (8 bits/channel) used by the majority of color displays.

[103] This method has been applied to images from both rovers taken during the first 400 sols of each mission. Examples of some typical true color image products are shown in Figure 23. Our calculated average chromaticity values from soil, rock, and sky Pancam images compare well to those derived from previous Viking and Mars Pathfinder imaging studies (Table 16). We have also analyzed changes in the chromaticities of the rover calibration

targets (Figure 19) during the course of each mission. The results (Figure 24) show that the  $x$  and  $y$  chromaticities are generally trending toward average bright soil/dust chromaticity values (toward a color defined as “dark yellowish brown”), providing a quantitative measure of the degree of aeolian dust covering on each target as the mission progresses. A more detailed study of soil, rock, and sky

chromaticities throughout the mission is being conducted by D. Savransky and J. F. Bell III (Chromaticity of the Martian sky as observed by the Mars Exploration Rover Pancam instruments, manuscript in preparation, 2005), and additional details about modeling of the Pancam calibration target for dust deposition effects is presented by Sohl-Dickstein et al. (manuscript in preparation, 2005).

[104] Study of the splined spectra from multiple images shows that two average normalized sets of radiance values can be calculated for sky and ground pixels which fit over 83% of all pixels of each type to within 2%. By using these normalized spectra, it is possible to produce approximations for missing filter values in images which do not have the complete six filter set of left eye Pancam filters described above. Using the average normalized spectra as a guide, approximations can be made for the missing values, and a more accurate estimate of the true color can be generated than if only the available filters had been used. This approach yields reasonably good performance when using three or more Pancam filters, with chromaticities differing by only about 3% on average from those calculated from the same images using all six filters.

### 3.3. “Super Resolution” Imaging

[105] Combining the information from a series of slightly offset images of the same scene in order to extrapolate a new image at an effectively higher than native resolution is often referred to as “super resolution” imaging. The process works by leveraging knowledge of the relative pointing of each contributing image and the pixel Point Spread Function (PSF) of the camera. The only limitations on attainable resolution are the precision to which these two factors can be determined. It is difficult to quantify the effective increase in resolution achieved by our occasional implementation of super resolution imaging using Pancam. Measures of scene entropy, for instance, cannot distinguish between added noise and added detail. However, as can be seen in Figure 25, super resolution can be a useful tool when examining features at the limit of Pancam’s native resolution (0.28 mrad/pixel).

[106] Our implementation involves coregistration of a set of 15 to 20 images acquired in rapid succession at slightly different pointings for the same scene. Table 17 provides a summary of Pancam super resolution sequences acquired as of August 2005. Coregistration is performed using pyramid alignment software developed at NASA/Ames [Sargent et al., 2005]. Iterative deconvolution is then performed using a naïve spatial domain backpropagation algorithm [Irani and

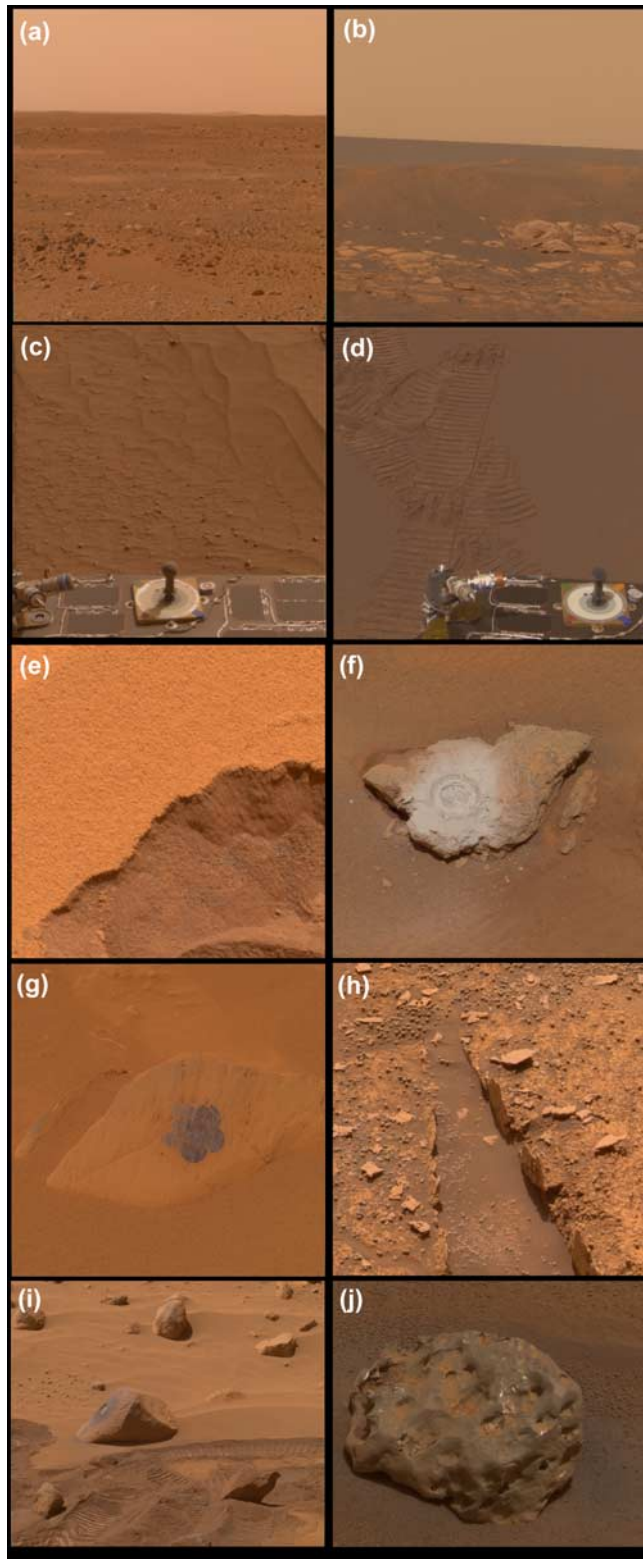


**Figure 23.** Examples of “true color” Pancam images from Spirit (left column) and Opportunity (right column) generated using calibrated Pancam radiance data. (a) Spirit sol 9, sequence P2354, 14:27 LTST; (b) Opportunity sol 4, sequence P2356, 13:20 LTST; (c) Spirit sol 56, sequence P2584, 14:56 LTST; (d) Opportunity sol 13, sequence P2548, 10:38 LTST; (e) Spirit sol 73, sequence P2557, 10:36 LTST; (f) Opportunity sol 68, sequence P2581, 13:01 LTST; (g) Spirit sol 100, sequence P2544, 11:58 LTST; (h) Opportunity sol 170, sequence P2598, 09:11 LTST; (i) Spirit sol 342, sequence P2571, 12:36 LTST; (j) Opportunity sol 346, sequence P2591, 12:25 LTST.

**Table 16.** Comparison of Measured Chromaticity Values With Previous Mission Findings<sup>a</sup>

|             | Sky       |           | Rock      |           | Soil      |           |
|-------------|-----------|-----------|-----------|-----------|-----------|-----------|
|             | x         | y         | x         | y         | x         | y         |
| Pathfinder  | 0.39–0.41 | 0.37–0.38 | 0.38–0.41 | 0.35–0.39 | 0.43–0.45 | 0.38–0.41 |
| Viking 1    | 0.4       | 0.38      | —         | —         | 0.43–0.46 | 0.39–0.40 |
| Viking 2    | 0.4       | 0.38      | —         | —         | 0.43–0.44 | 0.39      |
| Spirit      | 0.39–0.42 | 0.37–0.38 | 0.40–0.43 | 0.38–0.40 | 0.44–0.46 | 0.38–0.39 |
| Opportunity | 0.38–0.40 | 0.37      | 0.39–0.42 | 0.37–0.39 | 0.42–0.45 | 0.38–0.40 |

<sup>a</sup>Pathfinder and Viking values from *Maki et al.* [1999].

*Peleg*, 1991]. The component images are first forward-mapped into the high-resolution scratch space. A back-propagation algorithm is then repeatedly applied to this scratch space, iteratively improving the high-resolution image held in scratch space. This process is described by the equation

$$S^j = \begin{cases} \frac{1}{N} \sum_i m(i, s_i) & (j = 0) \\ S^{j-1} - \frac{1}{N} \sum_i m(i, M(i, S^{j-1}) - s_i) & (j > 0) \end{cases}, \quad (41)$$

where  $S^j$  is the scratch space after iteration  $j$ ,  $s_i$  is contributing image  $i$ ,  $N$  is the number of contributing images,  $m$  is a forward mapping function relying on both coregistration and pixel PSF information, and  $M$  is the backward mapping inverse of  $m$ .

[107] The spatial weighting of the PSF used in the mapping functions  $M$  and  $m$  above is shown in Figure 26. This function equally weights all data within the solid angle subtended by the pixel, then falls off to 1% of the contribution at a third of a pixel width past the edge of the pixel, with the shape of the falloff described by an exponential. It is then scaled to conserve energy incident on each point, such that the sum of the overlaid PSFs of all pixels is unity everywhere. Although empirically this PSF has been effective at providing rapid results useful for tactical rover operations planning and initial scientific analyses [e.g., *Grotzinger et al.*, 2005], it lacks a physical basis. It should eventually be possible to calculate a more accurate PSF using the Modulation Transfer Function data or other measurements collected during Pancam calibration [Bell et al., 2003].

[108] The point of greatest effective resolution (the step after which more noise than useful information is added by the deconvolution algorithm, and the identification of which is one of the most difficult parts of the process to automate) is judged by eye. All super resolution sequences to date have used the shortpass blue filters (L7 and R1; 430 nm) because the shorter wavelength filters yield a narrower Pancam PSF [Bell et al., 2003], and because atmospheric dust scatters less at the shorter wavelengths, yielding less noise in the deconvolution process for blue filter images of distant targets than in red filter images.

#### 4. Future Refinements

[109] We have good confidence in the accuracy and precision of the Pancam in-flight calibration procedures described here, but it is a universal truth that calibration could always be better. Several areas of potential improve-

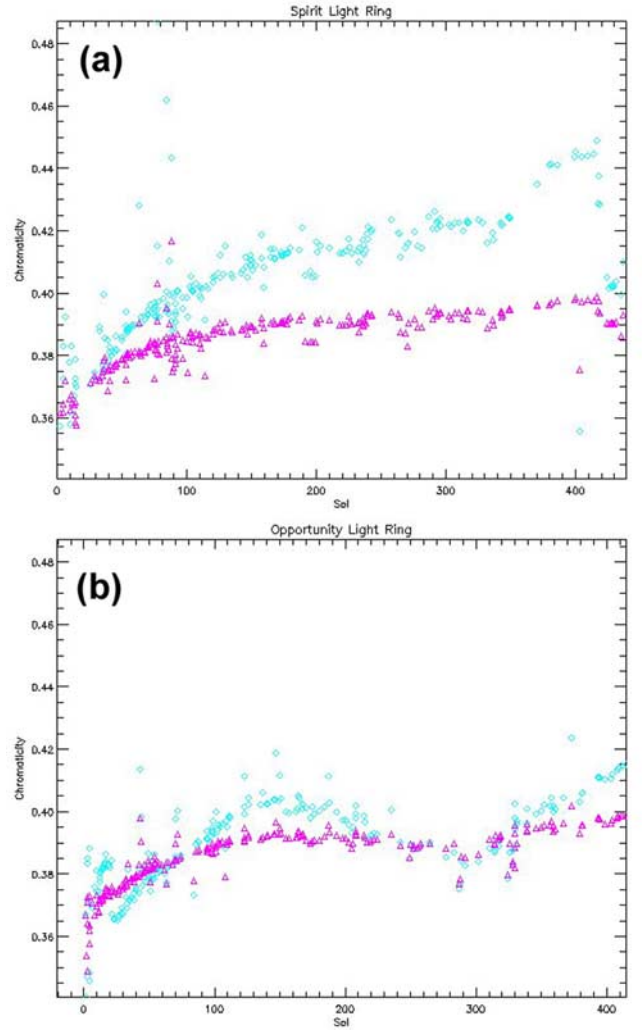


**Figure 24.** Plots of Pancam calibration target white ring chromaticity values versus time (sol on Mars) for (a) Spirit and (b) Opportunity. The cyan data are the chromaticity  $x$  values, and the magenta data are the chromaticity  $y$  values. Both targets' chromaticity values generally trend toward typical bright soil/dust averages ( $x, y \approx 0.44, 0.39$ ), but significant perturbations associated with “dust cleaning” events (Figure 19) can be seen in the data. The  $x$  axes of these plots are offset by 20.5 sols so that data points that are vertically aligned between the two rovers were acquired on the same Martian day.



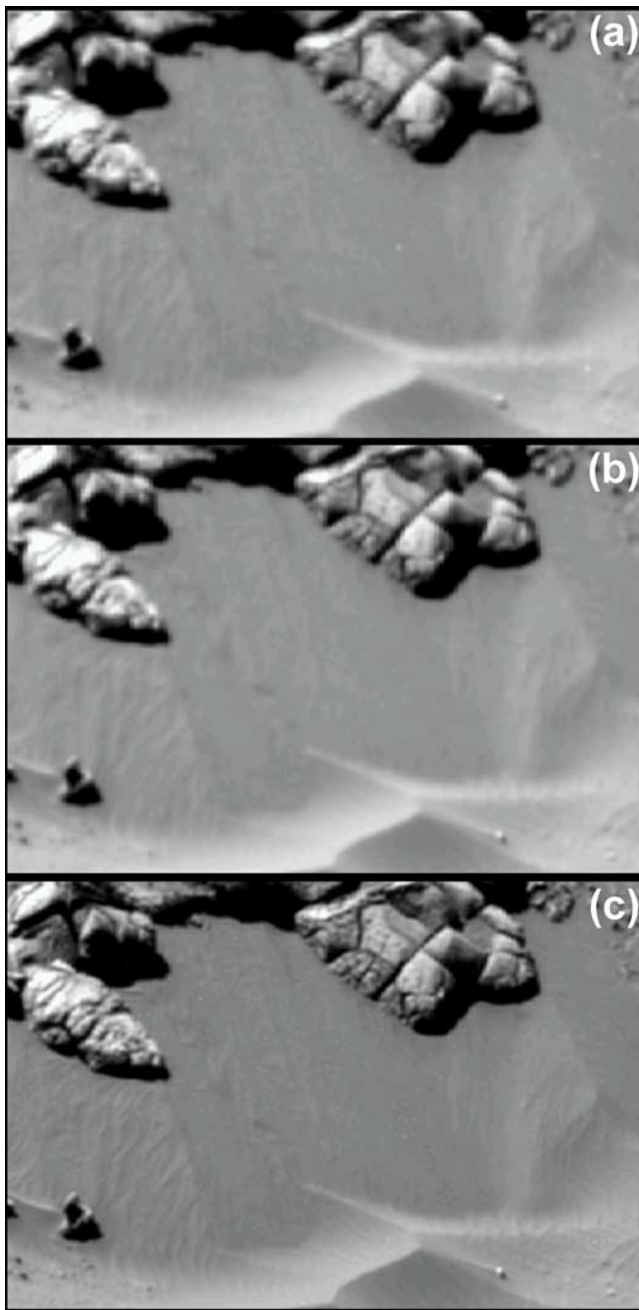


**Figure 25.** Super resolution example. This is an image of several small dune forms immediately below the Tsumeb feature on the north side of Endurance Crater acquired on Opportunity sol 168 using Pancam sequence P2596. (a) The image is formed by a single contributing image linearly interpolated to 8 times its native resolution. (b) The image is formed by the simple coregistration and summing of 17 contributing images. The image is extrapolated to 8 times native resolution by means of the super resolution algorithm described here applied to 17 contributing images. Note the many secondary ripple forms which are visible only in the super resolution image.

ment have already been noted above. For example, additional dark current images obtained on Mars could provide better temperature sampling for refinements of the dark current model and better characterization of the behavior of

**Table 17.** Pancam Super Resolution Imaging Sequences as of August 2005

| Rover | Sol | Sequence ID | Description                               |
|-------|-----|-------------|---|
| A     | 494 | P2533       | Larry's Outcrop, Columbia Hills           |
| A     | 85  | P2875       | Bonneville Crater, Heatshield             |
| B     | 453 | P2534       | Etched Terrain, Erebus Highway            |
| B     | 449 | P2532       | Etched Terrain, Erebus Highway            |
| B     | 291 | P2550       | Endurance Crater, Burns Cliff, Bartlett   |
| B     | 289 | P2549       | Endurance Crater, Burns Cliff, Whatanga   |
| B     | 288 | P2545       | Endurance Crater, Burns Cliff, Wellington |
| B     | 288 | P2544       | Endurance Crater, Burns Cliff, Crossbed   |
| B     | 282 | P2538       | Endurance Crater, Burns Cliff             |
| B     | 211 | P2568       | Endurance Crater, Central Dunes, Tendril  |
| B     | 168 | P2596       | Endurance Crater, Tsumeb                  |
| B     | 167 | P2594       | Endurance Crater, Victory                 |
| B     | 167 | P2592       | Endurance Crater, Katutura                |
| B     | 147 | P2569       | Endurance Crater, Sonora                  |
| B     | 147 | P2567       | Endurance Crater, Kalahari                |
| B     | 146 | P2559       | Endurance Crater, Namib                   |
| B     | 145 | P2557       | Endurance Crater, Burns                   |
| B     | 66  | P2859       | Backshell, Meridiani Plains               |

outlier pixels; more sky flat images acquired on Mars could provide a better assessment of the low-frequency component of the CCD flatfield pattern; further laboratory photometric investigations and analyses of the calibration target materials could help to refine models of the targets' scattering properties (especially close to specular geometries) and the variation in these properties as a function of target dustiness; additional constraints from preflight geometric calibration data could be used to refine the Pancam PSF and potentially enhance the effective resolution of super-resolution sequences.

[110] Despite the room for potential improvement in a number of aspects of the Pancam calibration pipeline, the present implementation of the calibration described here has

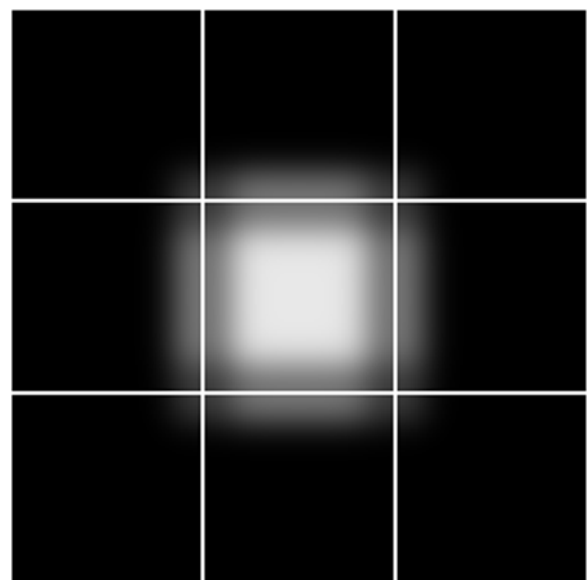


**Figure 26.** The pixel Point Spread Function (PSF) used in superresolution analysis. The PSF is shown in the spatial domain in the plane of the CCD. The grid markings delineate the boundaries of the underlying pixels. This function is a first approximation of the camera PSF only, and lacks both physical significance and an empirical basis.



**Table A1.** Pancam 8-Bit to 12-Bit Inverse Lookup Table 1

| 8 Bit | 12 Bit | 8 Bit | 12 Bit | 8 Bit | 12 Bit | 8 Bit | 12 Bit | 8 Bit | 12 Bit | 8 Bit | 12 Bit | 8 Bit | 12 Bit | 8 Bit | 12 Bit |
|-------|--------|-------|--------|-------|--------|-------|--------|-------|--------|-------|--------|-------|--------|-------|--------|
| 0     | 20     | 32    | 95     | 64    | 288    | 96    | 607    | 128   | 1054   | 160   | 1629   | 192   | 2331   | 224   | 3161   |
| 1     | 21     | 33    | 99     | 65    | 296    | 97    | 619    | 129   | 1070   | 161   | 1649   | 193   | 2355   | 225   | 3189   |
| 2     | 22     | 34    | 103    | 66    | 304    | 98    | 631    | 130   | 1086   | 162   | 1669   | 194   | 2379   | 226   | 3217   |
| 3     | 23     | 35    | 108    | 67    | 312    | 99    | 644    | 131   | 1102   | 163   | 1689   | 195   | 2403   | 227   | 3245   |
| 4     | 24     | 36    | 112    | 68    | 321    | 100   | 656    | 132   | 1119   | 164   | 1709   | 196   | 2428   | 228   | 3273   |
| 5     | 25     | 37    | 117    | 69    | 329    | 101   | 668    | 133   | 1135   | 165   | 1730   | 197   | 2452   | 229   | 3302   |
| 6     | 27     | 38    | 121    | 70    | 338    | 102   | 681    | 134   | 1152   | 166   | 1750   | 198   | 2477   | 230   | 3330   |
| 7     | 28     | 39    | 126    | 71    | 346    | 103   | 694    | 135   | 1169   | 167   | 1771   | 199   | 2501   | 231   | 3359   |
| 8     | 30     | 40    | 131    | 72    | 355    | 104   | 707    | 136   | 1185   | 168   | 1792   | 200   | 2526   | 232   | 3388   |
| 9     | 31     | 41    | 136    | 73    | 364    | 105   | 720    | 137   | 1202   | 169   | 1813   | 201   | 2551   | 233   | 3417   |
| 10    | 33     | 42    | 141    | 74    | 374    | 106   | 733    | 138   | 1220   | 170   | 1834   | 202   | 2576   | 234   | 3446   |
| 11    | 35     | 43    | 147    | 75    | 383    | 107   | 746    | 139   | 1237   | 171   | 1855   | 203   | 2602   | 235   | 3475   |
| 12    | 36     | 44    | 152    | 76    | 392    | 108   | 760    | 140   | 1254   | 172   | 1877   | 204   | 2627   | 236   | 3505   |
| 13    | 38     | 45    | 158    | 77    | 402    | 109   | 773    | 141   | 1272   | 173   | 1898   | 205   | 2652   | 237   | 3534   |
| 14    | 40     | 46    | 164    | 78    | 412    | 110   | 787    | 142   | 1290   | 174   | 1920   | 206   | 2678   | 238   | 3564   |
| 15    | 42     | 47    | 170    | 79    | 422    | 111   | 801    | 143   | 1308   | 175   | 1942   | 207   | 2704   | 239   | 3594   |
| 16    | 45     | 48    | 176    | 80    | 432    | 112   | 815    | 144   | 1326   | 176   | 1964   | 208   | 2730   | 240   | 3624   |
| 17    | 47     | 49    | 182    | 81    | 442    | 113   | 829    | 145   | 1344   | 177   | 1986   | 209   | 2756   | 241   | 3654   |
| 18    | 49     | 50    | 188    | 82    | 452    | 114   | 843    | 146   | 1362   | 178   | 2008   | 210   | 2782   | 242   | 3684   |
| 19    | 52     | 51    | 194    | 83    | 462    | 115   | 857    | 147   | 1380   | 179   | 2030   | 211   | 2808   | 243   | 3714   |
| 20    | 54     | 52    | 201    | 84    | 472    | 116   | 871    | 148   | 1398   | 180   | 2052   | 212   | 2834   | 244   | 3744   |
| 21    | 57     | 53    | 207    | 85    | 483    | 117   | 886    | 149   | 1417   | 181   | 2075   | 213   | 2861   | 245   | 3775   |
| 22    | 60     | 54    | 214    | 86    | 493    | 118   | 900    | 150   | 1435   | 182   | 2097   | 214   | 2887   | 246   | 3805   |
| 23    | 63     | 55    | 220    | 87    | 504    | 119   | 915    | 151   | 1454   | 183   | 2120   | 215   | 2914   | 247   | 3836   |
| 24    | 66     | 56    | 227    | 88    | 515    | 120   | 930    | 152   | 1473   | 184   | 2143   | 216   | 2941   | 248   | 3867   |
| 25    | 69     | 57    | 234    | 89    | 526    | 121   | 945    | 153   | 1492   | 185   | 2166   | 217   | 2968   | 249   | 3898   |
| 26    | 72     | 58    | 242    | 90    | 537    | 122   | 960    | 154   | 1511   | 186   | 2189   | 218   | 2995   | 250   | 3929   |
| 27    | 76     | 59    | 249    | 91    | 549    | 123   | 976    | 155   | 1530   | 187   | 2213   | 219   | 3022   | 251   | 3960   |
| 28    | 80     | 60    | 257    | 92    | 560    | 124   | 991    | 156   | 1550   | 188   | 2236   | 220   | 3050   | 252   | 3991   |
| 29    | 83     | 61    | 264    | 93    | 572    | 125   | 1007   | 157   | 1569   | 189   | 2260   | 221   | 3077   | 253   | 4023   |
| 30    | 87     | 62    | 272    | 94    | 583    | 126   | 1022   | 158   | 1589   | 190   | 2283   | 222   | 3105   | 254   | 4055   |
| 31    | 91     | 63    | 280    | 95    | 595    | 127   | 1038   | 159   | 1609   | 191   | 2307   | 223   | 3133   | 255   | 4083   |

proven to be more than adequate for assisting with sol-to-sol tactical rover measurement and driving decisions as well as enabling many kinds of detailed quantitative spectroscopic and photometric studies using Pancam images.

## Appendix A

[111] If an onboard 12 to 8 bit Lookup Table (LUT) was used to scale the original 12-bit Pancam imaging data prior to downlink, a corresponding inverse 8 to 12 bit LUT is required to restore the Pancam data to the closest possible approximation to its original 12 bit (linearly proportional to radiance) format. Three such LUTs and their corresponding Inverse Lookup Tables (ILUTs) were used during Pancam mission operations. ILUT #1 is listed in Table A1, ILUT #2 is listed in Table A2, and ILUT #3 is listed in Table A3. The specific LUT that was used for each image is indicated in the SAMPLE\_BIT\_MODE\_ID field in each image's PDS file label.

## Appendix B: PDS Label Keywords Pertaining to Pancam Radiometric Calibration

[112] The following keywords pertaining to calibration are found in the SITE\_DERIVED\_IMAGE\_PARMS and ROVER\_COORDINATE\_SYSTEM groups of the PDS label [Jet Propulsion Laboratory (JPL), 2005]:

[113] INSTRUMENT\_AZIMUTH: Azimuth angle of the center of the Pancam field of view at the time of the observation, defined in SITE frame with 0° azimuth to the north.

[114] INSTRUMENT\_ELEVATION: Elevation angle of the center of the Pancam field of view at the time of the

observation, defined with positive elevation angles measured down from a reference plane parallel to the rover deck and at the height of the cameras. The traditionally defined emission angle is 90° minus this reported value of INSTRUMENT\_ELEVATION.

[115] SOLAR\_AZIMUTH: Azimuth angle of the Sun at the time of the observation, defined in SITE frame with 0° azimuth to the north.

[116] SOLAR\_ELEVATION: Elevation angle of the Sun at the time of the observation, defined with positive elevation angles measured down from a reference plane parallel to the rover deck and at the height of the cameras. The traditionally defined solar incidence angle is 90° minus this reported value of SOLAR\_ELEVATION.

[117] ORIGIN\_ROTATION\_QUATERNION: Rotation matrices required to convert rover frame azimuth (0° is straight forward) and elevation (0° is parallel to the rover deck) coordinates to absolute "site frame" coordinates (north = azimuth 0°, horizon = elevation 0°).

[118] The following keywords pertaining to calibration are found in the DERIVED\_IMAGE\_PARMS group of the PDS label.

[119] SOFTWARE\_LANGUAGE: string, programming language that the software is written in (e.g., IDL).

[120] SOFTWARE\_MODULE\_NAME: string, name of the primary software module used to generate this product. This is the module to which the parameters (SOFTWARE\_PARAMETER\_\*) and keywords (SOFTWARE\_KEYWORD\_\*) apply.

[121] SOFTWARE\_MODULE\_TYPE: string, type of module (e.g., PROCEDURE, FUNCTION).

**Table A2.** Pancam 8-Bit to 12-Bit Inverse Lookup Table 2

| 8 Bit | 12 Bit | 8 Bit | 12 Bit | 8 Bit | 12 Bit | 8 Bit | 12 Bit | 8 Bit | 12 Bit | 8 Bit | 12 Bit | 8 Bit | 12 Bit | 8 Bit | 12 Bit |
|-------|--------|-------|--------|-------|--------|-------|--------|-------|--------|-------|--------|-------|--------|-------|--------|
| 0     | 0      | 32    | 75     | 64    | 268    | 96    | 587    | 128   | 1034   | 160   | 1609   | 192   | 2311   | 224   | 3141   |
| 1     | 1      | 33    | 79     | 65    | 276    | 97    | 599    | 129   | 1050   | 161   | 1629   | 193   | 2335   | 225   | 3169   |
| 2     | 2      | 34    | 83     | 66    | 284    | 98    | 611    | 130   | 1066   | 162   | 1649   | 194   | 2359   | 226   | 3197   |
| 3     | 3      | 35    | 88     | 67    | 292    | 99    | 624    | 131   | 1082   | 163   | 1669   | 195   | 2383   | 227   | 3225   |
| 4     | 4      | 36    | 92     | 68    | 301    | 100   | 636    | 132   | 1099   | 164   | 1689   | 196   | 2408   | 228   | 3253   |
| 5     | 5      | 37    | 97     | 69    | 309    | 101   | 648    | 133   | 1115   | 165   | 1710   | 197   | 2432   | 229   | 3282   |
| 6     | 7      | 38    | 101    | 70    | 318    | 102   | 661    | 134   | 1132   | 166   | 1730   | 198   | 2457   | 230   | 3310   |
| 7     | 8      | 39    | 106    | 71    | 326    | 103   | 674    | 135   | 1149   | 167   | 1751   | 199   | 2481   | 231   | 3339   |
| 8     | 10     | 40    | 111    | 72    | 335    | 104   | 687    | 136   | 1165   | 168   | 1772   | 200   | 2506   | 232   | 3368   |
| 9     | 11     | 41    | 116    | 73    | 344    | 105   | 700    | 137   | 1182   | 169   | 1793   | 201   | 2531   | 233   | 3397   |
| 10    | 13     | 42    | 121    | 74    | 354    | 106   | 713    | 138   | 1200   | 170   | 1814   | 202   | 2556   | 234   | 3426   |
| 11    | 15     | 43    | 127    | 75    | 363    | 107   | 726    | 139   | 1217   | 171   | 1835   | 203   | 2582   | 235   | 3455   |
| 12    | 16     | 44    | 132    | 76    | 372    | 108   | 740    | 140   | 1234   | 172   | 1857   | 204   | 2607   | 236   | 3485   |
| 13    | 18     | 45    | 138    | 77    | 382    | 109   | 753    | 141   | 1252   | 173   | 1878   | 205   | 2632   | 237   | 3514   |
| 14    | 20     | 46    | 144    | 78    | 392    | 110   | 767    | 142   | 1270   | 174   | 1900   | 206   | 2658   | 238   | 3544   |
| 15    | 22     | 47    | 150    | 79    | 402    | 111   | 781    | 143   | 1288   | 175   | 1922   | 207   | 2684   | 239   | 3574   |
| 16    | 25     | 48    | 156    | 80    | 412    | 112   | 795    | 144   | 1306   | 176   | 1944   | 208   | 2710   | 240   | 3604   |
| 17    | 27     | 49    | 162    | 81    | 422    | 113   | 809    | 145   | 1324   | 177   | 1966   | 209   | 2736   | 241   | 3634   |
| 18    | 29     | 50    | 168    | 82    | 432    | 114   | 823    | 146   | 1342   | 178   | 1988   | 210   | 2762   | 242   | 3664   |
| 19    | 32     | 51    | 174    | 83    | 442    | 115   | 837    | 147   | 1360   | 179   | 2010   | 211   | 2788   | 243   | 3694   |
| 20    | 34     | 52    | 181    | 84    | 452    | 116   | 851    | 148   | 1378   | 180   | 2032   | 212   | 2814   | 244   | 3724   |
| 21    | 37     | 53    | 187    | 85    | 463    | 117   | 866    | 149   | 1397   | 181   | 2055   | 213   | 2841   | 245   | 3755   |
| 22    | 40     | 54    | 194    | 86    | 473    | 118   | 880    | 150   | 1415   | 182   | 2077   | 214   | 2867   | 246   | 3785   |
| 23    | 43     | 55    | 200    | 87    | 484    | 119   | 895    | 151   | 1434   | 183   | 2100   | 215   | 2894   | 247   | 3816   |
| 24    | 46     | 56    | 207    | 88    | 495    | 120   | 910    | 152   | 1453   | 184   | 2123   | 216   | 2921   | 248   | 3847   |
| 25    | 49     | 57    | 214    | 89    | 506    | 121   | 925    | 153   | 1472   | 185   | 2146   | 217   | 2948   | 249   | 3878   |
| 26    | 52     | 58    | 222    | 90    | 517    | 122   | 940    | 154   | 1491   | 186   | 2169   | 218   | 2975   | 250   | 3909   |
| 27    | 56     | 59    | 229    | 91    | 529    | 123   | 956    | 155   | 1510   | 187   | 2193   | 219   | 3002   | 251   | 3940   |
| 28    | 60     | 60    | 237    | 92    | 540    | 124   | 971    | 156   | 1530   | 188   | 2216   | 220   | 3030   | 252   | 3971   |
| 29    | 63     | 61    | 244    | 93    | 552    | 125   | 987    | 157   | 1549   | 189   | 2240   | 221   | 3057   | 253   | 4003   |
| 30    | 67     | 62    | 252    | 94    | 563    | 126   | 1002   | 158   | 1569   | 190   | 2263   | 222   | 3085   | 254   | 4035   |
| 31    | 71     | 63    | 260    | 95    | 575    | 127   | 1018   | 159   | 1589   | 191   | 2287   | 223   | 3113   | 255   | 4073   |

**Table A3.** Pancam 8-Bit to 12-Bit Inverse Lookup Table 3

| 8 Bit | 12 Bit | 8 Bit | 12 Bit | 8 Bit | 12 Bit | 8 Bit | 12 Bit | 8 Bit | 12 Bit | 8 Bit | 12 Bit | 8 Bit | 12 Bit | 8 Bit | 12 Bit |
|-------|--------|-------|--------|-------|--------|-------|--------|-------|--------|-------|--------|-------|--------|-------|--------|
| 0     | 0      | 32    | 76     | 64    | 271    | 96    | 594    | 128   | 1045   | 160   | 1626   | 192   | 2336   | 224   | 3175   |
| 1     | 1      | 33    | 80     | 65    | 279    | 97    | 606    | 129   | 1062   | 161   | 1647   | 193   | 2361   | 225   | 3204   |
| 2     | 2      | 34    | 84     | 66    | 287    | 98    | 618    | 130   | 1078   | 162   | 1667   | 194   | 2385   | 226   | 3232   |
| 3     | 3      | 35    | 88     | 67    | 295    | 99    | 630    | 131   | 1094   | 163   | 1687   | 195   | 2409   | 227   | 3261   |
| 4     | 4      | 36    | 93     | 68    | 304    | 100   | 643    | 132   | 1111   | 164   | 1708   | 196   | 2434   | 228   | 3289   |
| 5     | 5      | 37    | 98     | 69    | 312    | 101   | 655    | 133   | 1127   | 165   | 1729   | 197   | 2459   | 229   | 3318   |
| 6     | 7      | 38    | 102    | 70    | 321    | 102   | 668    | 134   | 1144   | 166   | 1749   | 198   | 2484   | 230   | 3347   |
| 7     | 8      | 39    | 107    | 71    | 330    | 103   | 681    | 135   | 1161   | 167   | 1770   | 199   | 2509   | 231   | 3376   |
| 8     | 10     | 40    | 112    | 72    | 339    | 104   | 694    | 136   | 1178   | 168   | 1791   | 200   | 2534   | 232   | 3405   |
| 9     | 11     | 41    | 117    | 73    | 348    | 105   | 707    | 137   | 1196   | 169   | 1813   | 201   | 2559   | 233   | 3435   |
| 10    | 13     | 42    | 123    | 74    | 357    | 106   | 721    | 138   | 1213   | 170   | 1834   | 202   | 2585   | 234   | 3464   |
| 11    | 15     | 43    | 128    | 75    | 367    | 107   | 734    | 139   | 1230   | 171   | 1856   | 203   | 2610   | 235   | 3494   |
| 12    | 17     | 44    | 134    | 76    | 376    | 108   | 748    | 140   | 1248   | 172   | 1877   | 204   | 2636   | 236   | 3523   |
| 13    | 19     | 45    | 139    | 77    | 386    | 109   | 762    | 141   | 1266   | 173   | 1899   | 205   | 2662   | 237   | 3553   |
| 14    | 21     | 46    | 145    | 78    | 396    | 110   | 775    | 142   | 1284   | 174   | 1921   | 206   | 2688   | 238   | 3583   |
| 15    | 23     | 47    | 151    | 79    | 406    | 111   | 789    | 143   | 1302   | 175   | 1943   | 207   | 2714   | 239   | 3613   |
| 16    | 25     | 48    | 157    | 80    | 416    | 112   | 803    | 144   | 1320   | 176   | 1965   | 208   | 2740   | 240   | 3643   |
| 17    | 27     | 49    | 163    | 81    | 426    | 113   | 818    | 145   | 1338   | 177   | 1987   | 209   | 2766   | 241   | 3674   |
| 18    | 29     | 50    | 170    | 82    | 436    | 114   | 832    | 146   | 1356   | 178   | 2010   | 210   | 2792   | 242   | 3704   |
| 19    | 32     | 51    | 176    | 83    | 447    | 115   | 846    | 147   | 1375   | 179   | 2032   | 211   | 2819   | 243   | 3735   |
| 20    | 35     | 52    | 182    | 84    | 457    | 116   | 861    | 148   | 1393   | 180   | 2055   | 212   | 2845   | 244   | 3765   |
| 21    | 37     | 53    | 189    | 85    | 468    | 117   | 875    | 149   | 1412   | 181   | 2077   | 213   | 2872   | 245   | 3796   |
| 22    | 40     | 54    | 196    | 86    | 478    | 118   | 890    | 150   | 1431   | 182   | 2100   | 214   | 2899   | 246   | 3827   |
| 23    | 43     | 55    | 202    | 87    | 489    | 119   | 905    | 151   | 1450   | 183   | 2123   | 215   | 2926   | 247   | 3858   |
| 24    | 46     | 56    | 210    | 88    | 500    | 120   | 920    | 152   | 1469   | 184   | 2146   | 216   | 2953   | 248   | 3889   |
| 25    | 50     | 57    | 217    | 89    | 512    | 121   | 935    | 153   | 1488   | 185   | 2170   | 217   | 2981   | 249   | 3921   |
| 26    | 53     | 58    | 224    | 90    | 523    | 122   | 951    | 154   | 1507   | 186   | 2193   | 218   | 3008   | 250   | 3952   |
| 27    | 56     | 59    | 232    | 91    | 534    | 123   | 966    | 155   | 1527   | 187   | 2217   | 219   | 3036   | 251   | 3984   |
| 28    | 60     | 60    | 239    | 92    | 546    | 124   | 982    | 156   | 1547   | 188   | 2241   | 220   | 3063   | 252   | 4016   |
| 29    | 64     | 61    | 247    | 93    | 558    | 125   | 998    | 157   | 1566   | 189   | 2264   | 221   | 3091   | 253   | 4047   |
| 30    | 68     | 62    | 255    | 94    | 570    | 126   | 1013   | 158   | 1586   | 190   | 2288   | 222   | 3119   | 254   | 4079   |
| 31    | 72     | 63    | 263    | 95    | 582    | 127   | 1029   | 159   | 1606   | 191   | 2312   | 223   | 3147   | 255   | 4095   |

[122] (NOTE: in the following keywords, ?? is a 2-digit string: 01, 02, etc). These keywords, if present, describe the parameters and optional keywords passed to the calibration routine.

[123] NUM\_SOFTWARE\_PARAMETERS: integer, number of positional parameters that were supplied to the generating software. The PDS keywords that contain the values, names and types (if any) will be numbered 01, 02, 03, etc. A PDS keyword named SOFTWARE\_PARAMETER\_VALUE\_?? is required for each software parameter.

[124] SOFTWARE\_PARAMETER\_VALUE\_?: any valid PDS value, the value of positional parameter.

[125] SOFTWARE\_PARAMETER\_NAME\_?: string, descriptive name of corresponding parameter.

[126] NUM\_SOFTWARE\_KEYWORDS: integer, number of keyword parameters that were supplied to the generating software. The PDS keywords that contain the names, values and types (if any) will be numbered 01, 02, 03, etc. PDS keywords named SOFTWARE\_KEYWORD\_NAME\_?? and SOFTWARE\_KEYWORD\_VALUE\_?? are required for each software keyword supplied.

[127] SOFTWARE\_KEYWORD\_NAME\_?: string, name of supplied keyword.

[128] SOFTWARE\_KEYWORD\_VALUE\_?: any valid PDS value, the value of the corresponding keyword.

[129] RESPONSIVITY\_CONSTANTS: float array, the responsivity constants used in calibrating the image.

[130] RESPONSIVITY\_CONSTANTS\_FILE: string, name of the responsivity constants file used in calibrating the image.

[131] The responsivity constants filename will follow the following convention:

rc\_<scid><eye><filt>\_<sclk>\_<site><pos><seq>\_<ver>.txt

where <scid>, <eye>, <filt>, <sclk>, <site>, <pos>, <seq> are as defined for EDRs and RDRs in section 4.1 and in the SIS (and will be the same as the values in the image used to generate the responsivity constants file).

[132] <ver> is a version number of the responsivity constants file, and will increment if a new responsivity constants file is generated from the same image.

[133] FLAT\_FIELD\_FILE: string array, name of flat-field files used in calibration.

[134] FLAT\_FIELD\_FILE\_DESCRIPTION: string array, description of corresponding flat field file (e.g., “flat field image,” “flat field standard deviation image”).

[135] ZERO\_EXPOSURE\_IMAGE: string, name of zero-exposure image subtracted during calibration to account for shutter smear and masked-region dark current. Only set if a zero-exposure image product was used during on-ground calibration. Not set when onboard shutter-subtraction is done.

[136] REFERENCE\_PIXEL\_IMAGE: string, the product ID of the reference pixel image used to remove bias during calibration. Not set if no reference pixel image was returned in the same image sequence. If a reference pixel image is not available, the modeled bias is used.

[137] BIAS\_COEFFS\_FILE: string, name of bias coefficients file used in calibrating the image.

[138] BIAS\_COEFFS\_DESCRIPTION: string, description of corresponding bias coefficients file.

[139] INVERSE\_LUT\_FILE: string, name of inverse-lookup-table file used in calibration. If raw images are already 12-bit (have not been LUT-ed) then no inverse-LUT file is used.

[140] DARK\_CURRENT\_FILE: string array, names of dark current files used in calibration.

[141] DARK\_CURRENT\_FILE\_DESCRIPTION: string array, description of corresponding dark current files (e.g., “Shutter dark coefficients image,” “Active dark coefficients image”).

[142] INPUT\_IMAGE: string array, images used to generate this RDR. For Radiometrically calibrated RDRs, this will be the name of the raw RDR.

## Appendix C: Pancam (and Other MER Camera) File Naming Convention

### C1. Pancam Science EDRs and RDRs

[143] As defined in the MER Software Interface Specification document [JPL, 2005], each MER Raw Experiment Data Record (EDR) is uniquely identified by incorporating into the product filename a rover mission identifier, an instrument identifier, the starting Spacecraft Clock count (SCLK) of the camera event, the data product type, the rover site location, the rover position within the site, the sequence number, the camera eye, the spectral filter, a product creator identifier and a version number.

[144] These identifiers are strung together into the following MER Camera filename convention:

<scid><inst><sclk><prod><site><pos><seq><eye><filt>  
<who><ver>.<ext>

where

**scid** = (1 integer) MER rover Spacecraft Identifier.

Valid values:

2: Spirit = MER-A = MER-2

1: Opportunity = MER-B = MER-1

**inst** = (1 alpha character) MER science instrument identifier.

Valid values for MER camera instruments:

**P** - Pancam

**N** - Navcam

**F** - Front Hazcam

**R** - Rear Hazcam

**M** - Microscopic Imager

**E** - EDLcam (Descent Imager)

**sclk** = (9 integers) Starting Spacecraft Clock time.

[145] This is the number of seconds since January 1, 2000 at 11:58:55.816 UTC.

**prod** = (3 alpha characters) Product Type identifier of input data.

[146] Product types are differentiated as having camera-induced distortion removed (geometrically “linearized”) or

not removed (nominal), and, as being Thumbnail-sized or not.

[147] Four special flag characters exist:

[148] a) Beginning **E** - Type of EDR, which are raw with no camera model linearization or radiometric correction. If no beginning E, then it is a Reduced Data Record (RDR).

[149] b) Ending **T** - EDR or RDR that is Thumbnail-sized.

[150] c) Ending **L** - If no beginning E, denotes an RDR that is **L**inearized, except for Thumbnail sized RDRs.

[151] d) Ending **N** - If no beginning E, denotes an RDR that is Thumb**N**ail-sized and **L**iNearized.

[152] Valid values for MER Pancam raw EDR data products that are most relevant for scientific and calibration purposes are:

| Data Product         | Identifier |
|----------------------|------------|
| Full frame EDR       | <b>EFF</b> |
| Sub-frame EDR        | <b>ESF</b> |
| Downsampled EDR      | <b>EDN</b> |
| Thumbnail EDR        | <b>ETH</b> |
| Reference Pixels EDR | <b>ERP</b> |

[153] Valid values for MER Pancam instrument calibrated RDR data products generated by the Pancam team using the procedures described in this paper are:

| Data Product   | Identifier |
|--|------------|
| Radiometrically-calibrated full-frame RDR (DN units)       | <b>CCD</b> |
| Radiometrically-calibrated thumbnail RDR (DN units)        | <b>CCT</b> |
| Radiometrically-calibrated full-frame RDR (absolute units) | <b>RAD</b> |
| Radiometrically-calibrated thumbnail RDR (absolute units)  | <b>RAT</b> |
| Calibrated Full-frame RDR (relative reflectance units)     | <b>IOF</b> |
| Calibrated thumbnail RDR (relative reflectance units)      | <b>IOT</b> |

[154] Files having any other Product Type identifiers were not created by the Pancam team and thus may not be suitable for quantitative scientific analyses.

**site** = (2 alphanumeric) Site location count (indicates rover's location). Use of both ntegers and alphas allows for a total range of 0 thru 1295. A value greater than 1295 is denoted by "##" (2 pound signs), requiring the user to extract actual value from label.

[155] The valid values, in their progression, are as follows:

|                       |   |
|-----------------------|---|
| Range 0 thru 99       | - "00", "01", "02"... "99"                                    |
| Range 100 thru 1035   | - "A0", "A1" ... "A9", "AA", "AB"... "AZ", "B0", "B1"... "ZZ" |
| Range 1036 thru 1295  | - "0A", "0B"... "0Z", "1A", "1B"... "9Z"                      |
| Range 1296 or greater | - "##" (2 pound signs)  |

[156] Example value is "AK" for value of 120.

**pos** = (2 alphanumeric) Position-within-Site count (indicates

rover's position within site). The same range and meaning for valid values is used for *pos* as defined for *site* above.

[157] Valid values: **00**, **01**, **02**,...,**99**, **A0**, **A1**,...,**A9**, **AA**, **AB**, etc.

**seq** = (1 alpha character plus 4 integers) Sequence identifier. Denotes a group of images that were all obtained within a single command sequence.

[158] Valid values for character (position 1) in field:

|          |   |
|----------|---|
| <b>C</b> | - Cruise  |
| <b>D</b> | - IDD & RAT   |
| <b>E</b> | - Engineering   |
| <b>F</b> | - Flight Software automatic sequence                                |
| <b>G</b> | - (spare)   |
| <b>K</b> | - (spare)   |
| <b>M</b> | - Master (Surface only)   |
| <b>N</b> | - In-Situ instr. (APXS, MB, MI)                                     |
| <b>P</b> | - PMA & Remote Sensing instr. (Pancam, Navcam, Hazcam, MI, MiniTES) |
| <b>R</b> | - Rover Driving   |
| <b>S</b> | - Submaster   |
| <b>T</b> | - Test  |
| <b>W</b> | - Seq triggered by a Communications Window                          |
| <b>X</b> | - Contingency   |
| <b>Y</b> | - (spare)   |
| <b>Z</b> | - SCM Seqs  |

[159] Valid values for integers (positions 2 thru 5) in field: **0000** thru **4095** - Valid Sequence number, commanded by Ground

If **P** in character position:

|                                 |   |
|---------------------------------|---|
| <b>0000</b> through <b>0499</b> | - Misc. imaging setup/parm sequences      |
| <b>0500</b> through <b>0999</b> | - Unallocated, for possible future use    |
| <b>1000</b> through <b>1499</b> | - Hazcam sequences                        |
| <b>1500</b> through <b>1999</b> | - Navcam sequences                        |
| <b>2000</b> through <b>2899</b> | - Pancam sequences                        |
| <b>2900</b> through <b>2999</b> | - MI sequences                            |
| <b>3000</b> through <b>3999</b> | - MiniTES sequences                       |
| <b>4000</b> through <b>4095</b> | - Misc. PMA actuation seqs (deploy, etc.) |

**eye** = (1 alpha character) Camera eye.

Valid values are:

|          |                                  |
|----------|----------------------------------|
| <b>L</b> | - Left camera eye                |
| <b>R</b> | - Right camera eye               |
| <b>M</b> | - Monoscopic (non-stereo camera) |
| <b>N</b> | - Not Applicable                 |

**filt** = (1 alphanumeric) Spectral filter position.

[160] Valid values are an integer range of **0-8** (0 = no filter or N/A, 1 thru 8 are valid filter positions).

[161] Pancam Filter Positions:  
Wavelength (and bandpass) in nm at -10 C

| LEFT CAMERA          | RIGHT CAMERA      |
|----------------------|-------------------|
| 1. 739 (338 - EMPTY) | 1. 436 (37 - SP)* |
| 2. 753 (20)          | 2. 754 (20)       |



| LEFT CAMERA             | RIGHT CAMERA            |
|-------------------------|-------------------------|
| 3. 673 (16)             | 3. 803 (20)             |
| 4. 601 (17)             | 4. 864 (17)             |
| 5. 535 (20)             | 5. 904 (26)             |
| 6. 482 (30)             | 6. 934 (25)             |
| 7. 432 (32 - SP)*       | 7. 1009 (38 - LP)*      |
| 8. 440 Solar ND5** (20) | 8. 880 Solar ND5** (20) |

\*SP indicates short-pass filter; LP indicates long-pass filter

\*\*ND5 indicated  $10^{-5}$  neutral density coating

[162] Microscopic Imager “Filter” positions:

[163] 1. MI window/cover closed (500-700 nm response)

[164] 2. MI window/cover open (400-700 nm response)

**who** = (1 alpha character) Product Creator indicator. Valid values are:

- C** - Cornell University
- F** - USGS at Flagstaff
- M** - MIPL (OPGS) at JPL
- S** - SOAS at JPL
- X** - Other

**ver** = (1 alphanumeric) Version identifier providing uniqueness for book keeping.

[165] Valid values: **1, 2, 3, .. 9, A, B, .. Z**

**ext** = (4 alpha characters) 3-character PDS product type extension following a “.” character.

Valid values for nominal operations camera data products:

- IMG** - Camera image EDRs and RDRs (PDS labeled).
- JPG** - JPEG compressed (no PDS label).
- \_n.JPG** - Scaled and JPEG compressed, where **n** is **2** for 1/2 scale, **4** for 1/4 scale, or **8** for 1/8 scale (no PDS label). The filenames for these products are not PDS compliant, being longer than the 27.3 PDS nomenclature.

#### Example:

2P133918951EFF2232P2363L2C1.IMG

Spirit MER-A (“2”), Pancam instrument (“P”), SCLK 133918951 (MER-A Sol 85, 14:24:46 LTST; 2004-03-30, 11:41:37 UTC), Raw Full-Frame image (“EFF”), Site 22, Position 32, Sequence P2363, left Eye (“L”), Filter position 2 (753 nm), produced by Cornell U. (“C”), product version 1 (“1”), PDS format image (“.IMG”).

## C2. Important Notes About Pancam “Science” Versus “Operations” EDRs

[166] There are three flavors of raw Pancam images that are being released to the PDS archive, and it is important for scientists planning to do quantitative work with the Pancam images to understand the differences. Specifically, there are raw 8-bit “Operations” EDRs (sometimes called “OPGS EDRs”), raw 12-bit “Operations” EDRs, and raw 12-bit “Science” EDRs (sometimes called “SOAS EDRs”). Anyone interested in doing quantitative work with the **raw** Pancam images should use the Science EDRs. This is

because the MER team almost always used 12 to 8 bit Lookup Table (LUT) scaling on the Pancam images to avoid encoding noise in the downlinked data, and the 8-bit Operations EDRs have not had an Inverse Lookup Table (ILUT) scaling applied to return the data back to 12 bits. Therefore the Data Number (DN) values in the 8-bit Operations EDRs represent an approximately square-root encoded representation of the radiance on sensor, rather than a linear representation of that radiance. Using those data instead of the Science EDRs for quantitative work will result in significant errors. The 12-bit Operations EDRs have not been validated by the Pancam team, and so their use for scientific analysis is not recommended.

[167] The Science EDRs can be identified by the occurrence of the character “C” in the filename’s <who> field, which is the next-to-last character at the end of the filename, before the 3-letter extension (see section C1). The Operations EDRs have the character “M” in the <who> field in the filename. Users who intend to use the Pancam data for quantitative purposes should use the Science EDRs with a “C” in the <who> field in the filename.

[168] It is also important for researchers working with the Pancam data to know that the calibrated Pancam RAD and IOF files generated by the science team are stored as short-integer format (2 bytes/pixel) PDS files, rather than floating point files. Conversion of the values stored in the data files to their correct floating point values requires the use of the **RADIANCE\_OFFSET** and **RADIANCE\_SCALING\_FACTOR** keywords stored in the PDS header. Specifically, to retrieve the desired floating point values of the data, the following equation must be applied to the integer values stored in the archived files:

$$\text{float\_value} = \text{RADIANCE\_OFFSET} + \text{integer\_value} \cdot \text{RADIANCE\_SCALING\_FACTOR} \quad (\text{C1})$$

Properly functioning PDS file readers should automatically recognize the presence of the **RADIANCE\_OFFSET** and **RADIANCE\_SCALING\_FACTOR** keywords in the file label and apply this floating point scaling to the data when opening the archived files.

[169] **Acknowledgments.** We are grateful to the many scientists, engineers, managers, and administrators involved with the MER team at institutions and corporations worldwide who have helped to make the Pancams such a successful pair of imaging experiments on Mars. We thank Dave Brown, Mark Schwochert, Dave Thiessen, Darryl Day, Andy Collins, Tom Elliot, Alex Hayes, Ken Herkenhoff, Justin Maki, Larry Scherr, Greg Smith, Larry Soderblom, Steve Squyres, and Len Wayne for their countless hours of assistance and advice regarding Pancam calibration. We also thank Dan Britt, Woody Sullivan, Larry Stark, Dick Morris, Mike Shepard, Roger Clark, Patrick Pinet, Yves Daydou, and Pascal Depoix for their assistance with the preflight fabrication and characterization of the Pancam calibration target materials. Also critical to the success of Pancam has been the group of dedicated and hard working “Payload Downlink Leads” and “Payload Uplink Leads” (responsible for instrument health monitoring, tactical data product generation, and daily sequencing of new images). Besides the authors of this paper, this group includes Bill Farrand, Walter Goetz, Alex Hayes, Ken Herkenhoff, Jeff Johnson, Kjartan Kinch, Morten Madsen, Justin Maki, Elaina McCartney, Dick Morris, Tim Parker, Jon Proton, Frank Seelos, Jason Soderblom, Rob Sullivan, and Mike Wolff. And an enormous amount of gratitude also goes out to the “Cornell Calibration Crew,” a dedicated and hard-working team of undergraduate and graduate students and staff members who have been carefully monitoring camera performance and calibrating Pancam images every sol since January 2004. Thank you, Graham Anderson, Diane Bollen, Lindsey Brock, Rich Chomko, Emily Dean, Adam Fischman, Kristen Frazier, Alissa Friedman, Stephanie

Gil, Benjamin Herbert, Kelley Hess, Min Hubbard, Peter Meakin, Chase Million, Mary Mulvanerton, Eldar Noe, Alex Shapero, Alex Shih, John Skok, Pam Smith, Christopher Versfelt, and Brandi Wilcox. This work was supported by grants and contracts from JPL and the NASA Mars Exploration Rover project.

## References

- Bell, J. F., III, T. B. McCord, and P. D. Owensby (1990), Observational evidence of crystalline iron oxides on Mars, *J. Geophys. Res.*, **95**, 14,447–14,461.
- Bell, J. F., III, et al. (2000), Mineralogic and compositional properties of Martian soil and dust: Results from Mars Pathfinder, *J. Geophys. Res.*, **105**, 1721–1755.
- Bell, J. F., III, et al. (2003), Mars Exploration Rover Athena Panoramic Camera (Pancam) investigation, *J. Geophys. Res.*, **108**(E12), 8063, doi:10.1029/2003JE002070.
- Bell, J. F., III, et al. (2004a), Pancam multispectral imaging results from the Spirit rover at Gusev crater, *Science*, **305**, 800–806.
- Bell, J. F., III, et al. (2004b), Pancam multispectral imaging results from the Opportunity rover at Meridiani Planum, *Science*, **306**, 1703–1709.
- Bell, J. F., III, et al. (2004c), Pancam Calibration Report, *JPL Internal Doc. MER 420-6-700 (D-19826)*, Jet Propul. Lab., Pasadena, Calif., 25 June.
- Bertelsen, P., et al. (2004), Magnetic Properties Experiments on the Mars Exploration Rover Spirit at Gusev Crater, *Science*, **305**, 827–829.
- Carter, E. C., et al. (Eds.) (2004), *Colorimetry*, 3rd ed., *Publ. CIE 15:2004*, Int. Comm. on Illumination, Vienna. (Available at <http://www.cie.co.at/framepublications.html>)
- Clark, R. N., G. A. Swayze, A. J. Gallagher, T. V. V. King, and W. M. Calvin (1993), The USGS Digital Spectral Library, *U.S. Geol. Surv. Open File Rep.*, 93-592.
- Colina, L., R. C. Bohlin, and F. Castelli (1996), The 0.12–2.5 micron absolute flux distribution of the Sun for comparison with solar analog stars, *Astron. J.*, **112**, 307–315.
- Farrand, W. H., J. F. Bell III, J. R. Johnson, S. W. Squyres, J. Soderblom, and D. W. Ming (2006), Spectral variability among rocks in visible and near-infrared multispectral Pancam data collected at Gusev crater: Examinations using spectral mixture analysis and related techniques, *J. Geophys. Res.*, **111**, E02S15, doi:10.1029/2005JE002495.
- Grotzinger, J. P., et al. (2005), Stratigraphy and sedimentology of a dry to wet eolian depositional system, Burns formation, Meridiani Planum, Mars, *Earth Planet. Sci. Lett.*, **240**, 11–72, doi:10.1016/j.epsl.2005.09.039.
- Hapke, B. (1993), *Theory of Reflectance and Emittance Spectroscopy*, 455 pp., Cambridge Univ. Press, New York.
- He, X. D., K. E. Torrance, F. X. Sillion, and D. P. Greenberg (1991), A comprehensive physical model for light reflection, *Comput. Graphics*, **25**(4), 175–186.
- Herkenhoff, K. E., et al. (2003), Athena Microscopic Imager investigation, *J. Geophys. Res.*, **108**(E12), 8065, doi:10.1029/2003JE002076.
- Irani, M., and S. Peleg (1991), Improving resolution by image registration, *CVGIP: Graphical Models Image Process.*, **53**, 231–239.
- Jet Propulsion Laboratory (2005), Mars Exploration Rover (MER) Software Interface Specification for Camera Experiment Data Record (EDR) and Reduced Data Record (RDR) Operations and Science Data Products, *JPL Doc. D-22846*, Pasadena, Calif. (Available at [http://pds-geosciences.wustl.edu/geodata/mer2-m-pancam-2-edr-sci-v1/mer2pc\\_0xxx/document/camera\\_dpis.pdf](http://pds-geosciences.wustl.edu/geodata/mer2-m-pancam-2-edr-sci-v1/mer2pc_0xxx/document/camera_dpis.pdf))
- Johnson, J. R., et al. (2006), Spectrophotometric properties of materials observed by Pancam on the Mars Exploration Rovers: 1. Spirit, *J. Geophys. Res.*, doi:10.1029/2005JE002494, in press.
- Lemmon, M. T., et al. (2004), Atmospheric imaging results from the Mars Exploration Rovers: Spirit and Opportunity, *Science*, **306**, 1753–1756.
- Maki, J. N., J. J. Lorre, P. H. Smith, R. D. Brandt, and D. J. Steinwand (1999), The color of Mars: Spectrophotometric measurements at the Pathfinder landing site, *J. Geophys. Res.*, **104**, 8781–8794.
- Maki, J. N., et al. (2003), Mars Exploration Rover Engineering Cameras, *J. Geophys. Res.*, **108**(E12), 8071, doi:10.1029/2003JE002077.
- McSween, H. Y., et al. (2004), Basaltic rocks analyzed by the Spirit Rover in Gusev Crater, *Science*, **305**, 842–845.
- McSween, H. Y., et al. (2006), Characterization and petrologic interpretation of olivine-rich basalts at Gusev Crater, Mars, *J. Geophys. Res.*, **111**, E02S10, doi:10.1029/2005JE002477.
- Morris, R., H. Lauer, C. Lawson, E. Gibson, G. Nace, and C. Stewart (1985), Spectral and other physiochemical properties of submicron powders of hematite ( $\alpha$ -Fe<sub>2</sub>O<sub>3</sub>), maghemite ( $\gamma$ -Fe<sub>2</sub>O<sub>3</sub>), magnetite (Fe<sub>3</sub>O<sub>4</sub>), goethite ( $\alpha$ -FeOOH), and lepidocrocite ( $\gamma$ -FeOOH), *J. Geophys. Res.*, **90**, 3126–3144.
- Mustard, J. F., and J. F. Bell III (1994), New composite reflectance spectra of Mars from 0.4 to 3.14  $\mu$ m, *Geophys. Res. Lett.*, **21**, 353–356.
- Pinet, P. C., A. Cord, Y. Daydou, F. Boubault, S. Chevrel, and V. Lapeyriere (2001), Influence of linear versus non-linear mixture on bidirectional reflectance spectra using a laboratory wide field spectral imaging facility, *Lunar Planet. Sci.*, **XXXII**, abstract 1552.
- Reid, R. J., et al. (1999), Imager for Mars Pathfinder (IMP) image calibration, *J. Geophys. Res.*, **104**, 8907–8926.
- Sargent, R., M. Deans, C. Kunz, M. Sims, and K. Herkenhoff (2005), The Ames MER Microscopic Imager toolkit, paper presented at IEEE Aerospace Conference, Inst. of Electr. and Electron. Eng., Big Sky, Mont.
- Seelos, F. P., R. E. Arvidson, E. A. Guinness, and M. J. Wolff (2004), Radiative transfer photometric analysis of surface materials at the Mars Exploration Rover landing sites, *Eos Trans. AGU*, **85**(47), Fall Meet. Supp., Abstract P21A-0199.
- Shepard, M. K. (2001), The Bloomsburg University Goniometer (B.U.G.) Laboratory: An integrated laboratory for measuring bidirectional reflectance functions, *Lunar Planet. Sci.*, **XXXII**, abstract 1015.
- Soderblom, L. A., et al. (2004), Soils of Eagle Crater and Meridiani Planum at the Opportunity Rover landing site, *Science*, **306**, 1723–1726.
- Smith, P. H., et al. (1997), First results from the Pathfinder camera, *Science*, **278**, 1758–1765.
- Squyres, S. W., et al. (2003), Athena Mars rover science investigation, *J. Geophys. Res.*, **108**(E12), 8062, doi:10.1029/2003JE002121.
- Stokes, M., M. Anderson, S. Chandrasekar, and R. Motta (1996), A standard default color space for the Internet—sRGB, Microsoft and Hewlett-Packard Joint Report, Version 1.10. (Available at <http://www.w3.org/Graphics/Color/sRGB>)
- Thomas, N. W. J. Markiewicz, R. M. Sablotny, M. W. Wuttke, H. U. Keller, J. R. Johnson, R. J. Reid, and P. H. Smith (1999), The color of the Martian sky and its influence on the illumination of the Martian surface, *J. Geophys. Res.*, **104**, 8795–8808.
- Tomasko, M. G., L. R. Dose, M. Lemmon, P. H. Smith, and E. Wegryn (1999), Properties of dust in the Martian atmosphere from the Imager on Mars Pathfinder, *J. Geophys. Res.*, **104**, 8987–9008.

H. M. Ameson, J. F. Bell III, J. Joseph, M. J. Johnson, D. Savransky, and J. N. Sohl-Dickstein, Department of Astronomy, Cornell University, 424 Space Sciences Building, Ithaca, NY 14853-6801, USA. (jfb8@cornell.edu)

M. T. Lemmon, Department of Atmospheric Sciences, Texas A&M University, College Station, TX 77843-3150, USA.